2001

Non-linear, irreversible magnetization processes in magnetic materials: instrumentation, measurements, modeling and application

Bin Zhu
Iowa State University

INFORMATION TO USERS

This manuscript has been reproduced from the microfilm master. UMI films the text directly from the original or copy submitted. Thus, some thesis and dissertation copies are in typewriter face, while others may be from any type of computer printer.

The quality of this reproduction is dependent upon the quality of the copy submitted. Broken or indistinct print, colored or poor quality illustrations and photographs, print bleedthrough, substandard margins, and improper alignment can adversely affect reproduction.

In the unlikely event that the author did not send UMI a complete manuscript and there are missing pages, these will be noted. Also, if unauthorized copyright material had to be removed, a note will indicate the deletion.

Oversize materials (e.g., maps, drawings, charts) are reproduced by sectioning the original, beginning at the upper left-hand corner and continuing from left to right in equal sections with small overlaps.

Photographs included in the original manuscript have been reproduced xerographically in this copy. Higher quality 6" x 9" black and white photographic prints are available for any photographs or illustrations appearing in this copy for an additional charge. Contact UMI directly to order.

Bell & Howell Information and Learning
300 North Zeeb Road, Ann Arbor, MI 48106-1346 USA
800-521-0600

Non-linear, irreversible magnetization processes in magnetic materials: instrumentation, measurements, modeling and application

by

Bin Zhu

A dissertation submitted to the graduate faculty

in partial fulfillment of the requirements for the degree of

DOCTOR OF PHILOSOPHY

Major: Electrical Engineering (Electromagnetics)

Major Professor: David C. Jiles

Iowa State University

Ames, Iowa

2001

UMI Number: 3003284

UMI Microform 3003284

Bell & Howell Information and Learning Company
300 North Zeeb Road
P.O. Box 1346
Ann Arbor, MI 48106-1346

Graduate College
Iowa State University

This is to certify that the Doctoral dissertation of

Bin Zhu

has met the dissertation requirements of Iowa State University

Signature was redacted for privacy.

Major Professor

Signature was redacted for privacy.

For the Major Program

Signature was redacted for privacy.

For the Graduate College

TABLE OF CONTENTS

ACKNOWLDGEMENTS

This work was supported by the United States National Science Foundation through Iowa State University.

First of all, I would like to express my sincere appreciation to my major professor Dr. David C. Jiles for his wise guidance and warm encouragement throughout the course of this study. His professional and personal instruction will be beneficial to my future.

Secondly, I would like to extend my appreciation to Dr. Chester Lo and Dr. Marcus J. Johnson. Their wise instructions in practical work made me learn a lot.

Thirdly, I would like to thank Dr. Udpa, Dr. Bowler, Dr. Mina and Dr. Thompson for dedicating time to serve on my committee.

Also special thanks to all members of Magnetic Group of Ames Laboratory. Their advice, thoughts, expertise and friendship through the course of this research are extremely helpful.

Finally, I would like to dedicate this dissertation to my parents and sister for their love and encouragement.

ABSTRACT

The main objective of this research is to develop instrumentation and models in order to study the Barkhausen effect both experimentally and theoretically. Another objective of this research is to investigate the effect of stress on magnetic properties of thin film using the micromagnetic (Landau-Lifschitz-Gilbert) modeling approach.

A new computer-controlled system Magneprobe-II based on our previous Magneprobe system has been developed to make Barkhausen emission (BE) measurement on materials. This involved a complete replacement of control and data logging software with new code which was researched and subsequently tested. System development included the hardware for generating an alternating magnetic field and detection of the BE signal, and software for instrument control and data analysis. This system provides the capability for making BE measurements using various settings such as the parameters of the excitation field, and analyzing the results in a variety of ways including time and frequency domain analysis. Measurements can be made easily and rapidly through the use of system software. Inspection procedures were implemented into the software in modular form. New procedures can therefore be easily added, allowing evolution of the instrument to meet new needs.

The new instrument can be used in a variety of nondestructive evaluation procedures. Material loss is a major problem in many engineering applications. Case-hardened steel components are frequently used in high wear applications to minimize the rate of material loss in situations where friction occurs between moving parts. Ultimately the material loss leads to failure of components because they can no longer sustain the intended levels of stress. Therefore, monitoring of wear rates non-destructively would allow components to be replaced before failure. In this thesis, we report the study of BE

measurements on well-controlled laboratory steel samples with different case depths in order to demonstrate the relationship between the BE signal and the amount of material removed from the case-hardened steel. The BE signal was measured and analyzed using the new system. The results demonstrate conclusively the viability of using BE measurement for monitoring wear-induced material loss.

Ferromagnetic hysteresis and the Barkhausen effect are mainly related to the irreversible stochastic motion of magnetic domain walls during the magnetization process. The intrinsically random nature of domain wall motion is a consequence of the pinning process caused by lattice defects, inclusions, or interactions between different walls. Magnetic and thermal treatments, applied stresses, and many other factors may affect the properties of the pinning sites. Because of this, a detailed description of the various microscopic magnetization processes, and of the related hysteretic behavior, still remains a very difficult task. In this thesis, a new BE model is presented and the modeling results are compared with the experimental data in both the time and frequency domain to test its validity. This shows that the new model can accurately reproduce the experimental BE signals.

Although stress has an important role in magnetism , it is surprising that modeling of magnetization processes in thin films in the presence of external stresses has received little attention. Recent experimental results obtained from nickel thin films showed a stress dependence of the hysteresis loop properties different from those from the bulk magnetic materials. Such differences can be attributed to the different mechanisms of magnetization reversal in thin films and bulk materials. In order to investigate the stress effect in magnetic thin films, a new micromagnetic model based on the Landau-Lifshitz-

Gilbert (LLG) equation has been developed. The modeling results show that the hysteresis loop properties, such as coercivity and remanence, should change drastically with applied stress and this is in good agreement with experimental observations.

1 GENERAL INTRODUTION

1.1 Barkhausen effect

The Barkhausen effect was discovered many years ago [1] as a result of magnetizing a ferromagnetic material with a time dependent magnetic field, and detecting the flux changes in a coil. This effect can be demonstrated with the apparatus shown in Figure 1-1. A search coil is wound on a specimen and is connected through an amplifier to a loudspeaker. The specimen is then subjected to a smoothly increasing field. However, no matter how smoothly and continuously the field is increased, a series of clicks are heard over the loudspeaker which are due to small spontaneous voltage pulses induced in the coil.

The discovery of the Barkhausen effect represented a fundamental proof of the existence of magnetic domains, postulated by Weiss [2]. When, many years later, the direct connection of Barkhausen effect with domain wall dynamics began to be

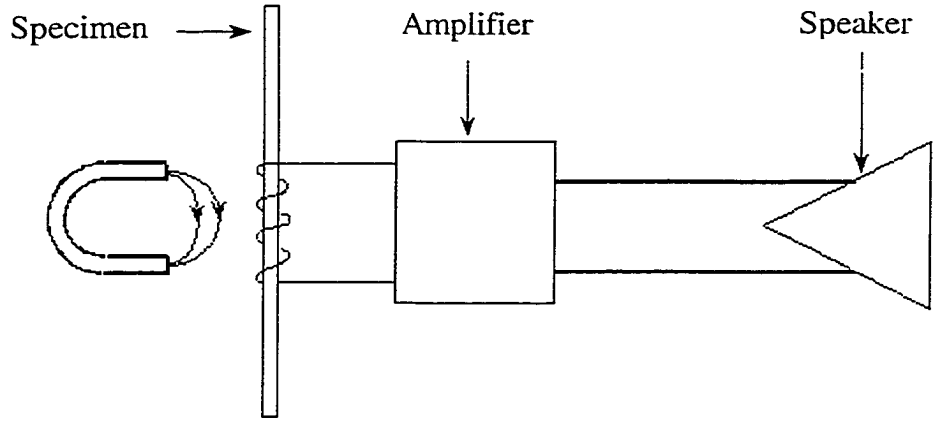

Figure 1-1 Demonstration of Barkhausen effect

appreciated, it became evident that Barkhausen effect can provide basic quantitative information on magnetization processes and may represent a unique key to the microscopic interpretation of ferromagnetic hysteresis.

Several factors play a role in contributing to the Barkhausen effect, including domain wall motion, domain rotation, domain nucleation and annihilation. The precise nature of Barkhausen emission (BE) signals is closely related to the microstructure of the magnetic material and consequently analysis of these signals can be used as a technique for materials evaluation, particularly for determining details of the microstructure. Stress also plays a vital role in changing the BE signals which arises principally from the dependence of differential susceptibility on stress.

The detected BE signals usually have frequency components from several kilohertz to several hundred kilohertz. This limits the range of penetration of the signals in conducting or permeable materials. Therefore, The BE signals can only be used for characterization of the near surface region.

1.2 Development of the model of Barkhausen effect

Because of its inherent complexity and intrinsic stochastic character, the quantitative description of the Barkhausen effect has proved to be extremely difficult. Nevertheless recent research on the description of the underlying processes such as domain wall motion and domain rotation [3, 4, 5] has led to the development of the theoretical models of the Barkhausen effect. Bertotti and coworkers [6, 7, 8] developed a comprehensive model (ABBM model) of the Barkhausen effect in which the Barkhausen effects are described by the stochastic motion of a domain wall subject to a random potential inside the material under the action of an applied field. By restricting the

investigations to the central part of the hysteresis loop, where domain wall motion is the dominant process, the Barkhausen effect can be described by a Langevin equation [9], whose solution provides definite analytic expressions for the Barkhausen effect. However, the assumption of this model limits its use to experiments where the differential permeability and the time derivative of applied field are constant which rarely occurs in practice.

A generalized model which is able to describe the Barkhausen effect over the entire hysteresis loop was proposed by Jiles, Sipahi and Williams (JSW model) [10]. One assumption of this model is that the rate of irreversible change in magnetization is proportional to the level of Barkhausen activity in a given time interval. In order to account for the random nature of the Barkhausen effect, it is also assumed that the Barkhausen activity in a given time interval is correlated with the activity in the previous time interval, but varies by an amount which is random in nature. Based on these assumptions, the Barkhausen effect can be described in terms of two components: a deterministic component which is reproducible and depends on the differential susceptibility, and a stochastic or random component. While the simplicity of this model is attractive, no attempt has been made to try to model the frequency response of the Barkhausen signal.

1.3 Micromagnetics

Until very recently, the principal theory for the interpretation of the hysteresis behavior of ferromagnetic materials was the domain theory. The building blocks in this theory are the domain and the domain wall, and the independent variables describing the

magnetic state are the directions of the magnetization within the domain and the positions of the domain walls. These are determined by minimizing the free energy. In this theory, the magnetization is constrained to be homogeneous inside the domains, and its direction to vary only within the domain walls.

In micromagnetics [11, 12] these constraints are relaxed, the individual magnetic moments within a domain are allowed to take different orientations and the magnetization $\boldsymbol{M}$ is described by

$$\boldsymbol{M} = M_s \cdot \boldsymbol{v} \tag{1-1}$$

where the spontaneous magnetization M_s is the magnitude of $\boldsymbol{M}$, $\boldsymbol{v}$ is the direction of $\boldsymbol{M}$ and it varies continuously with position

$$\boldsymbol{v} = v_x \boldsymbol{l}_x + v_y \boldsymbol{l}_y + v_z \boldsymbol{l}_z \tag{1-2}$$

Here $\boldsymbol{l}_x$, $\boldsymbol{l}_y$, $\boldsymbol{l}_z$ are unit vectors in the Cartesian coordinate system and v_x, v_y, v_z satisfy $\sqrt{v_x^2 + v_y^2 + v_z^2} = 1$. The changes in the bulk magnetization as a function of the applied field are described in terms of the changes in the direction of magnetization at every point and not by domain growth or domain rotation as in domain theory. Domains and domain walls, when they exist, should result naturally from this theory as regions in which the spatial variation of magnetization is respectively very slow and very rapid. To calculate the actual magnetic states, one looks for the minima of the free energy (i.e. the sum of the exchange, anisotropy, magnetostatic energies, etc), with the external field as a parameter.

However the formidable computational complexity of the micromagnetic approach limited its use at first to only a few simple cases, such as calculating the critical

field of magnetization reversal in infinite cylinders [13] that can be solved analytically. The development of adequate numerical methods for the solution of such problems by the LLG approach has attracted considerable interest in the last 30 years. Recently, the rapid advances in computer capabilities coupled with the ease of access to such facilities, have led to a dramatic increase in numerical modeling of magnetic structures within domains.

1.4 Scope of this thesis

Beginning with a general introduction in chapter 1 and ending with a general conclusion in chapter 7, this thesis can be broadly divided into two parts. The first part, which consists of chapters 2, 3, 4 and 5, discusses the background theories, measurement, applications and modeling of the Barkhausen effect. The second part, which will be presented in chapter 6, investigates the influence of applied stress on magnetic moments using the micromagnetic Landau-Lifschitz-Gilbert method.

In chapter 2, the basic magnetic processes and their relationship with Barkhausen effect will be addressed. The application of BE measurement will also be briefly reviewed in this chapter.

In chapter 3, a new multi-functional BE measurement system will be introduced. This system has been used to measure the BE signal on plain carbon steels with different carbon contents. The results presented in this chapter indicate that Barkhausen effect can be used as a method for material characterization.

In chapter 4, the nondestructive evaluation of wear-induced material loss in case-hardened steels through BE measurement will be discussed. The experimental results will be presented along with corresponding analysis and discussion.

In chapter 5, after a review of existing Barkhausen models, a new model incorporating ideas from these previous models will be presented. The Jiles-Atherton hysteresis model has been integrated into this model to calculate the irreversible permeability. Therefore, the new non-linear model can be used to investigate the BE signal according to the variation of the hysteresis loops. The comparison of modeling results with experimental results is also presented in this chapter.

In chapter 6, based on the Landau-Lifschitz-Gilbert equation, a new approach to the micromagnetic model, which can now be used to investigate the effect of stress on magnetic properties of thin films, will be presented. The modeling results along with the corresponding analysis and discussion will also be presented in this chapter.

2 MAGNETIC BARKHAUSEN EFFECT: THEORY, MEASUREMENT AND APPLICATION

2.1 Hysteresis

It is conventional to discuss the properties of ferromagnetic materials in terms of various parameters associated with the hysteresis loop of the material. Figure 2-1 shows such a loop, together with the definition of customary parameters.

The remanence B_r is defined as the nonzero flux density remaining in the material when the field in the material is brought from its maximum value back to zero. The coercivity H_c is the additional amount of field in the opposite direction that has to be applied before the remaining flux density in the material is finally brought back to zero.

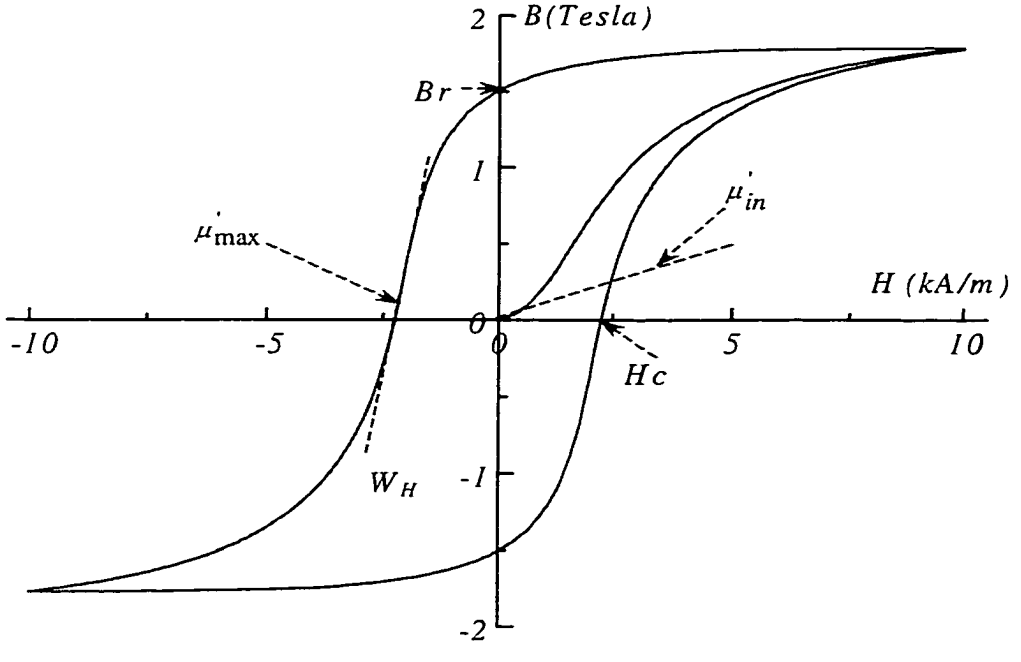

Figure 2-1 A typical hysteresis loop of a ferromagnetic material

The slope of the B-H curve, known as the differential permeability $\mu^{\cdot}$, is typically a maximum at the coercive field H_c, and so the maximum differential permeability $\mu^{\cdot}_{\max}$ is another characteristic of the hysteresis loop. The path taken on the B-H plot when an unmagnetized specimen is brought to maximum field is known as the initial magnetization curve, and the slope of the initial magnetization as the field begins to increase from $H = 0$ is known as the initial differential permeability $\mu^{\cdot}_{in}$.

The area enclosed by the hysteresis loop is the hysteresis loss W_H. The loop area is the magnetic energy that is dissipated if the material is to be completely cycled around the loop. The energy loss is associated with irreversible motion of magnetic domain walls inside the material and appears in the material as heat. The hysteresis is thus due to irreversible thermodynamic changes that develop as a result of magnetization.

One effect that has to be addressed is the problem of demagnetizing effects due to finite geometries and magnetic pole formation at both ends of the specimen. This effect leads to a reduction in effective local field in the material by $-N_d \boldsymbol{M}$, where N_d is known as the demagnetizing factor and is dependent on the shape of the sample.

The smooth appearance of the hysteresis loops is due solely to the properties of the instrumentation used to determine them. The implication of the discovery of the Barkhausen effect is that if variations in the magnetic flux density $\boldsymbol{B}$ are sufficiently well resolved, it would be seen that the hysteresis curve is not smooth but consists of a large number of small steps as depicted in Figure 2-2. If a search coil is wound around a specimen that is slowly magnetized, these individual steps in flux density are detected as sharp transient pulses of voltage across the coil and these pulses are called Barkhausen effect pulses.

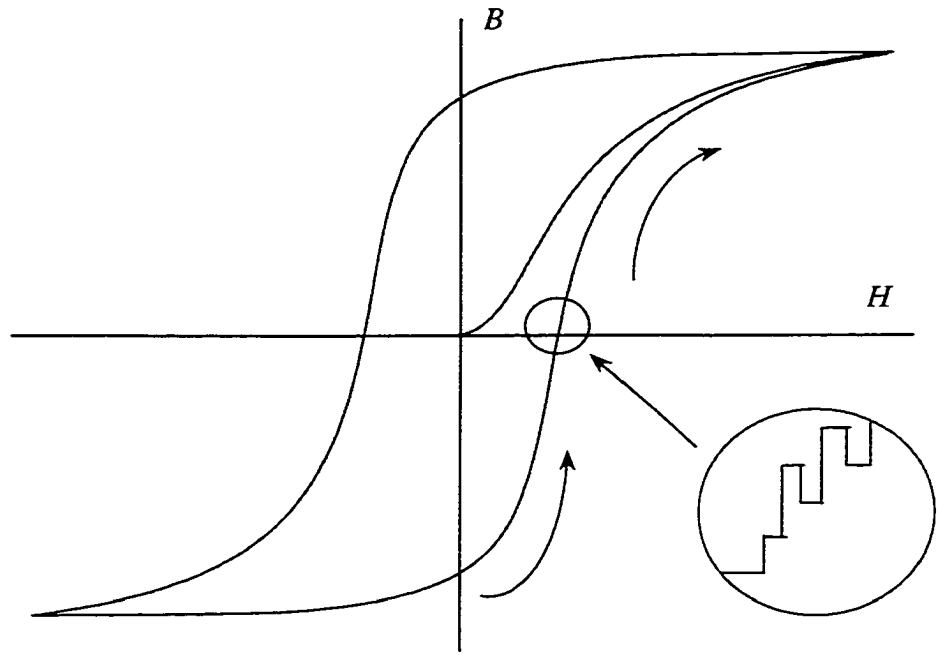

Figure 2-2 Barkhausen discontinuities along the hysteresis loop

2.2 Barkhausen effect and magnetization processes

2.2.1 Domain and domain walls

According to the theory of magnetism [14], magnetic moments in ferromagnetic materials are ordered into small regions called domains. Each domain is typically made up of 10^{12} to 10^{18} magnetic moments aligned in the same direction. Every domain is magnetized to saturation, but the vector sum of all the domains can be zero, and the material is then considered to be macroscopically demagnetized. The direction of alignment for domains generally follows one of the crystallographic axes, with certain axes preferred over others because of magnetocrystalline anisotropy. These preferred axes are called the "easy axes". The atomic ordering in these directions allows a reduction in energy compared with other directions, referred to as the magnetocrystalline

anisotropy energy.

The region between domains, where the magnetic moments change their orientations, is called a domain wall, a schematic diagram of which is shown in Figure 2-3. This change in orientation is normally spread out over several hundred atomic layers and the number of layers involved in the orientation change is called the domain-wall thickness. Two competing forces determine the domain-wall thickness, one arises from the exchange energy, the other from the anisotropy energy.

The exchange energy (E_{exch}) is created by the interaction between magnetic moments and is defined as

$$E_{exch} = -\mu_0 z J m_i m_j \cos\phi \tag{2-1}$$

where μ_0 is the permeability in free space and its value is $\mu_0 = 4\pi \times 10^{-7}\ Hm^{-1}$, z is the

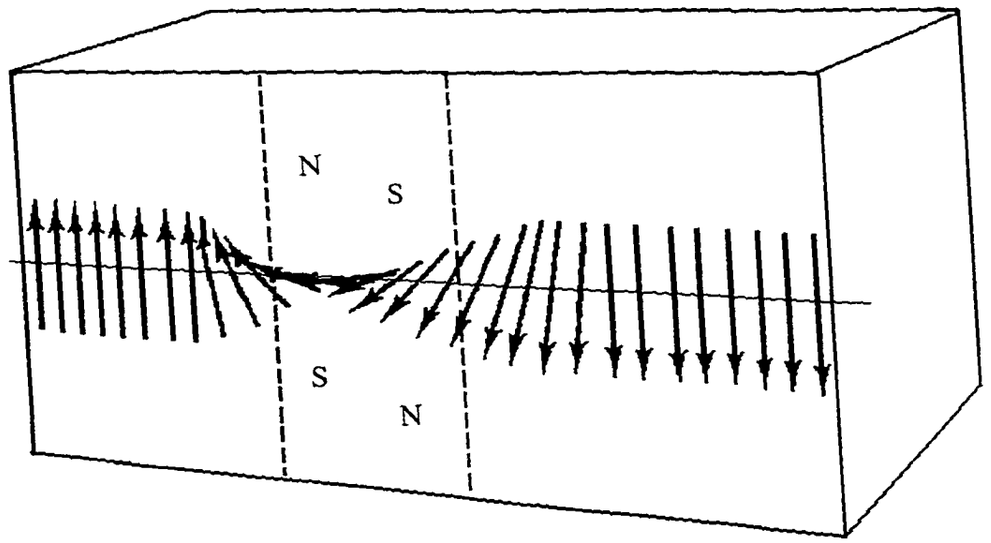

Figure 2-3 Schematic diagram of the orientation change of magnetic moments within a domain wall

number of nearest neighbors, J is the nearest-neighbor interaction, m_i and m_j are the strength of magnetic moments (usually $m_i = m_j = m$) and ϕ is the angle between the neighboring moments. In the simplest case of a linear chain, each magnetic moment has two nearest neighbors, that is $z = 2$. If ϕ is small, one can substitute $\cos\phi = 1 - \phi^2/2$, and the exchange energy per moment becomes

$$E_{exch} = \mu_0 J m^2 (\phi^2 - 2) \tag{2-2}$$

Summing the individual exchange energies over the number of moments in the wall yields

$$E_{exch} = \mu_0 J m^2 \phi^2 n \tag{2-3}$$

where n is the number of moments in the wall.

For a 180° domain wall with n lattice parameter, each of size a, ϕ becomes π/n. Substituting it into (2-3) gives the exchange energy per unit area

$$\frac{E_{exch}}{a^2} = \frac{\mu_0 J m^2 \pi^2}{n a^2} \tag{2-4}$$

From the above equation, it is clear that the larger n is, the lower the value ϕ and the lower the exchange energy. Therefore, exchange energy tends to make the domain wall thicker (with large n).

Anisotropy energy is associated with the energy differences of the magnetic moments when they are aligned along different crystallographic directions. In the case of a domain wall of thickness δ, the anisotropy energy per unit area E_{anis} can be expressed as

$$E_{anis} = K\delta \tag{2-5}$$

where K is the anisotropy constant. The above equation shows that the anisotropy tends to make the domain wall thinner because the anisotropy energy is lower with the smaller domain wall thickness δ.

The summation of the anisotropy and exchange energies gives the expression for the domain-wall energy per unit area $E_{domain-wall}$:

$$E_{domain-wall} = \frac{\mu_0 Jm^2 \pi^2}{na^2} + K\delta \tag{2-6}$$

The thickness of the domain wall is determined by minimizing the domain-wall energy with respect to its thickness. Table 2-1 lists the domain-wall properties for iron, cobalt and nickel. It can be seen that the material with the largest anisotropy energy, cobalt, has the thinnest domain wall. Nickel has the smallest anisotropy energy and the thickest domain wall of the group.

There are two general types of domain walls, 180° domain wall and non-180° domain wall. The 180° domain walls are the most common and occur between anti-parallel domains. The non-180° domain walls have orientations depending on the direction of the easy axes in the material. In iron, the easy axes are the <100> directions,

Table 2-1 Domain wall properties for Iron, Cobalt and Nickel

Property	Fe	Co	Ni
Domain-wall thickness (nm)	40	15	100
(lattice parameters)	138	36	285
Exchange energy (J)	2.5×10^{-21}	4.5×10^{-21}	2×10^{-21}
Anisotropy energy at 300K (kJm^{-3})	48	450	-5

so the domain walls between a domain oriented along the (010) direction and one oriented in the (001) direction would be called a 90° domain wall. In nickel, the easy axes are the <111> direction and the non-180° domain walls will be either 71° or 109°.

2.2.2 Magnetization processes

A magnetic material that is not macroscopically magnetized contains many domains because the existence of a single domain is normally energetically unfavorable. When the magnetostatic energy exceeds the energy required for domain wall formation, multiple domains will form in the material.

Under the action of a magnetic field, the orientations and sizes of these magnetic domains will change. The changes in magnetization under an applied magnetic field can be either reversible or irreversible depending on the domain processes involved. A reversible change in magnetization is the one in which after application and removal of a magnetic field, the magnetization returns to its original value. More often both reversible and irreversible changes occur together, so that on removal of the field the magnetization does not return to its initial value.

It is often suggested that the magnetic hysteresis curve of a ferromagnetic material can be interpreted in terms of four distinct regions, as illustrated in Figure 2-4.

(i) Starting from zero field, a narrow region "1" where domain walls move reversibly and will return to their original position if the field is removed.

(ii) A low-field region "2", where domain walls move irreversibly as they overcome barriers presented by pinning sites in the microstructure.

(iii) A middle-field region "3", where domain nucleation and annihilation occurs.

(iv) A high-field region "4", where little domain wall motion occurs and further increase in magnetization is predominantly due to rotation of the magnetization

vectors within individual domains.

2.2.2.1 Motion of domain walls

Domain wall motion incorporates two distinct effects: domain wall bowing and translation. Domain wall bowing is a reversible process at low-field amplitudes, and it becomes irreversible when the domain wall is sufficiently deformed. The translation of domain walls is usually irreversible unless the material is sufficiently pure.

Williams and Shockley [15] reported direct visual evidence of discontinuous domain wall motion. They observed that the wall motion was generally fairly smooth, but now and then discontinuous when the wall encountered microstructural and compositional defects such as dislocations, voids, cracks, nonmagnetic inclusions or impurities. Some of these defects produce strains that interact, through magnetoelastic

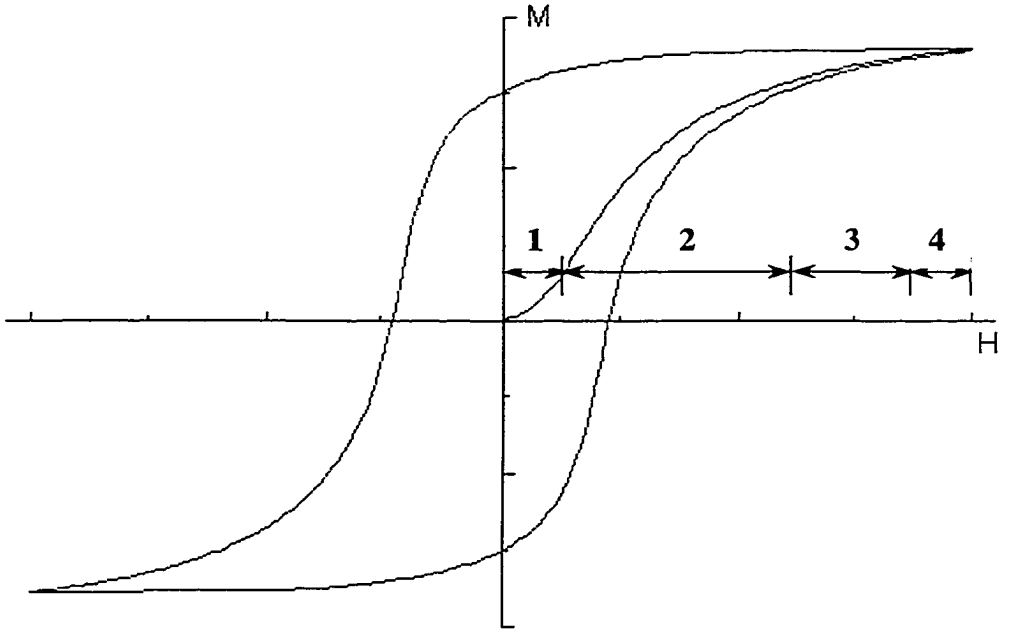

Figure 2-4 Magnetization curve and the classification of magnetization mechanisms according to the field strength at which they occur

coupling, with magnetic moments within a domain. Others, such as nonmagnetic inclusions, affect the mobility of domain walls for two reasons: the energy of the domain wall is reduced by the nonmagnetic region, and subsidiary or spike domains are produced on the nonmagnetic region, thus altering the magnetostatic energy of the domain.

The energy of a domain can be reduced by an inclusion because the domain-wall area is diminished and the wall's surface energy is reduced. Although this is only one of several factors reducing the energy of domain walls located on pinning sites, the wall is inhibited from moving further until the applied magnetic field supplies enough energy to push it past the inclusion region.

The production of subsidiary domains or free poles around inclusions was theorized by Néel [16]. The free poles produce a significant restoring force on a domain wall. If the inclusion is entirely within the domain, there will be free poles around it with an associated demagnetization energy as shown in Figure 2-5(a). In reality, an inclusion

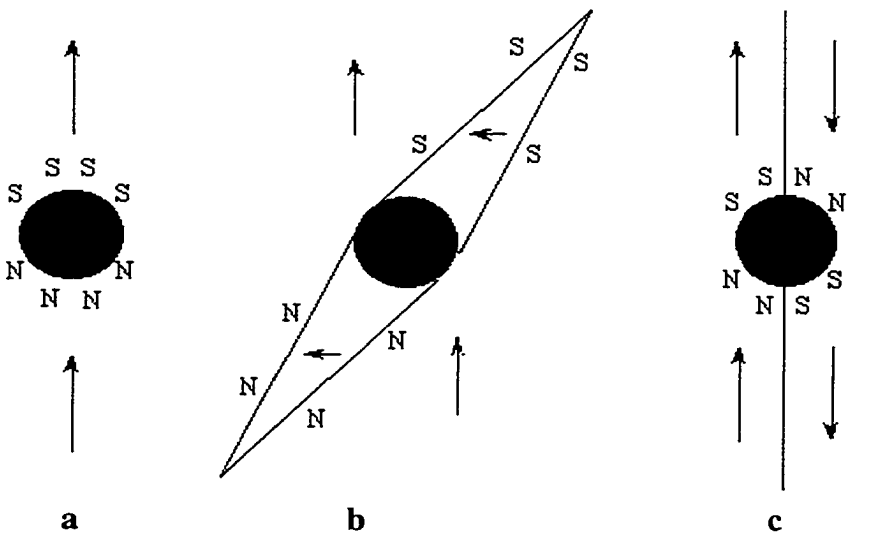

Figure 2-5 (a) A spherical inclusion within a domain. (b) Spike domain attached to an inclusion. (c) The domain structure as the domain wall bisects the inclusion

may be attached by a spike domain within the body of a domain as shown in Figure 2-5(b). As a domain wall bisects the inclusion, the free poles are redistributed according to the domain orientation, and the magnetostatic energy is reduced. In addition, the energy could be further reduced to zero because closure domains would form [17].

The ability of inclusions to inhibit domain-wall movement is dependent on the inclusion size [18]. A large inclusion (larger than 1μm, or approximately the domain wall thickness) impedes the wall primarily through the formation and growth of spike domains. Smaller inclusions hinder a wall primarily through reduction of domain-wall energy. Naturally, in most microstructures the inclusion sizes vary widely and both influences determine the magnetic behavior at the macroscopic level.

Therefore, domain wall movement is determined by not only the external magnetic field, but also the domain wall energy and defects in the magnetic material. Since these defects result in local energy minima when domain walls intersect them, an extra energy is needed for domain walls to overcome the energy barrier. When the external magnetic field is removed, the domain wall will stay at the last energy minimum which it has encountered.

Under the action of a low magnetic field, the high energy domain wall will reversibly translate over a short distance, or the low energy domain wall will reversibly bend until it encounters another pinning site.

At an intermediate magnetic field, the domain wall breaks away from its current pinning site, and moves without further increase in magnetic field, and later becomes pinned by another pinning site.

If the magnetic field increases further, the domain wall will continue moving, bending, unpinning, pinning and so on, until the domain walls move out of the material and the material becomes a single domain. Before becoming a single domain, the

energetically "favored" domains may grow and coalesce, while the "unfavored" domains may diminish. This process is called domain growth.

2.2.2.2 Rotation of domains

Due to the magnetocrystalline anisotropy, in zero applied field, the magnetic moments in each domain will align along the directions of the crystallographic easy axes which correspond to local energy minima.

At low field, the direction of alignment of the magnetic moments is displaced slightly from the original easy axes toward the field direction. This results in a reversible rotation of the magnetic moments within a domain.

At intermediate to high field, the magnetic moments within the domain rotate from their original easy axes to the easy axes closest to the field direction when the field energy overcomes the anisotropy energy. They will not rotate back to the original easy axes direction after the field is removed. Instead, they will remain at the last easy axes direction which they have encountered.

At higher fields, the magnetic moments are rotated further toward the field direction from the easy axes which are closest to the field direction. This results in a reversible rotation of the moments into the field direction and hence a reversible change in magnetization.

2.2.2.3 Domain nucleation

When a magnetic field is removed so that magnetization is reduced from saturation, new domains are nucleated around precipitates or grain boundaries where the magnetic poles are accumulated during the spin rotation. Goodenough [19] calculated the critical field strength for domain nucleation and indicated that the domain nucleation

could proceed when the reduction in the magnetic energy associated with the poles during the formation of new domains was greater than the work required to form domains.

2.2.2.4 Domain wall motion and Barkhausen events

The Barkhausen effect was originally thought to be due to irreversible domain rotation. It is now known to be due mainly to the irreversible domain wall movement which predominates in region "2" in Figure 2-4. Nix and Huggins [20] reported that the Barkhausen event was caused primarily by 180° domain walls and not by 90° domain walls. It has been shown that Barkhausen jumps can also occur at the "knee" regions of the magnetization curve [21, 22] which is caused by domain nucleation and annihilation. The experimental results [23] indicated that the BE signals due to the domain nucleation were normally larger than the BE signals due to the domain annihilation. However, the maximum Barkhausen activity usually occurs at around the coercive point where maximum irreversible magnetization change occurs.

In general, the movement of a domain wall under the influence of an applied magnetic field obeys a damped simple harmonic oscillator equation of the form [24]

$$m\frac{d^2x}{dt^2}+\beta\frac{dx}{dt}+\alpha x = F(t) \qquad (2\text{-}7)$$

where $F(t)$ is the force on the domain wall, x is the position of the wall, m is the inertia of the domain wall which simply relates its acceleration to the force causing acceleration, β is the damping coefficient which is determined by the combined effect of all energy dissipation mechanisms and α is the stiffness or restoring force coefficient. The force term $F(t)$ is normally expressed as $F(t) = b\mu_0 M_s H\cos\phi$, where $b=2$ for 180° domain

walls and $\sqrt{2}$ for 90° walls, ϕ is the angle between the applied field and the direction of magnetization.

From experimental studies of domain wall motion [25], it is known that the domain wall velocity is nearly constant during most of a Barkhausen jump. Thus, the inertial term $m\frac{d^2x}{dt^2}$ can be dropped and (2-7) can be rewritten as

$$v = \frac{dx}{dt} = \frac{b\mu_0 M_s}{\beta}(H\cos\phi - H_c) \tag{2-8}$$

where

$$H_c = \frac{\alpha}{b\mu_0 M_s}x \tag{2-9}$$

here v is the velocity of the domain wall and H_c is the local coercive field needed to be overcome to move the domain wall.

In a perfect single crystal, there would be no force to impede the motion of domain walls and the coercive field H_c would vanish everywhere. However, in any real material, there are always defects to hinder the motion of domain walls and the interactions between the defects and the domain walls can be described by the corresponding local coercive field H_c which is a complicated function of domain wall position x as shown in Figure 2-6. In general there is not much more that can be said about this function without some knowledge of the distribution of defects. However, it is evident that the distance between peaks in H_c is approximately equal to the distance between defects, while the magnitudes of the peaks are a measure of the strength of interactions between the defects and domain walls.

Now consider the motion of a 180° domain wall under an applied field that

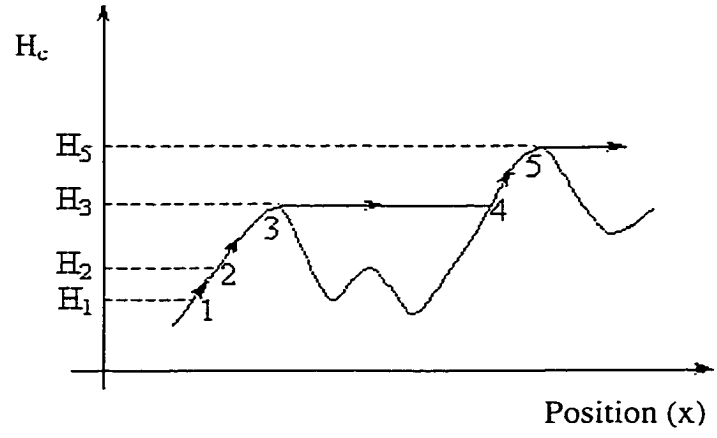

Figure 2-6 Domain wall motion and coercive field

increases continuously with time. Let H_1 be the field strength at time t_1, H_2 at time t_2 and so on. Suppose the applied field has the same direction as the direction of magnetization in one of the domains beside the wall, according to equation (2-9), the wall will move under the influence of a field H_1 until it reaches a point where $H_c = H_1$ which is point 1 in Figure 2-6. A continuous increase in field strength from H_1 to H_2 likewise causes the wall a continuous movement to point 2. However, when the field is further increased to H_3, which corresponds to a local maximum in $H_c(x)$, the wall position is unstable, which means that an additional infinitesimal increase in $\boldsymbol{H}$ will cause the wall to move from point 3 to point 4, where the coercive field balances the applied field. This discontinuous jump in the position of the wall corresponds to an abrupt increase in the magnetization which is a Barkhausen jump. A further increase in the applied field strength to level H_5, which corresponds to the next peak in $H_c(x)$, produces another jump. This process continues until favorably oriented domains combine. When most 180° domain walls have been annihilated by the joining of favorably oriented domains, the Barkhausen activity

begins to diminish. At this point, which is near saturation, further increases in the field increase the bulk magnetization principally by continuous domain rotation.

2.3 Barkhausen emissions measurement

The most common means of measuring the BE is to surround the specimen with a pick-up coil. The sample is set onto the desired hysteresis loop by cycling the applied magnetic field a few times up to the maximum field to be used. The magnetic field is then slowly changed by increasing the current through the magnetizing coil and the voltage due to the rapid flux changes is detected on the pickup coil. The Barkhausen noise measured by this coil configuration is called encircle Barkhausen noise [26].

If $\Delta\phi$ is the flux change associated with a Barkhausen jump, then the voltage induced in a coil is given by

$$V = -N\frac{d\phi}{dt} \tag{2-10}$$

where N is the number of turns in the pickup coil. The relationship between the flux change and the change in magnetic moments that gives rise to this flux change is very difficult to establish quantitatively and depends on the geometry of the coil and on the permeability of the sample [27]. For simplicity, the flux change $\Delta\phi$ is usually considered to be proportional to the change in magnetic moment Δm produced by the Barkhausen jump.

Tebble *et al.* [28] indicated that the Barkhausen jump in the material and the pickup coil can be considered to be two coupled inductors each with its own time constant and with a particular coupling constant depending on the relative geometry of the two coils. Based on this, two extreme cases can be calculated [27, 29]. If the time

constant of the pickup coil (τ_c) is much shorter than the time constant of the Barkhausen jump (τ_s), the coil has very little effect on the voltage pulse which can be described as

$$V(t) = \frac{N\Delta\phi}{\tau_s}\left[e^{-\frac{t}{\tau_s}} - e^{-\frac{t}{\tau_c(1-k^2)}}\right] \qquad \tau_c << \tau_s \tag{2-11}$$

where k is the coupling constant and varies between 0 and 1 for loose and tight coupling, respectively.

At the other extreme, that is, when the time constant of the pickup coil is much longer than the time constant of the Barkhausen jump, the induced voltage is given by

$$V(t) = \frac{N\Delta\phi}{\tau_c}\left[e^{-\frac{t}{\tau_c}} - e^{-\frac{t}{\tau_s(1-k^2)}}\right] \qquad \tau_s << \tau_c \tag{2-12}$$

and

$$V_{\max} = \frac{N\Delta\phi}{\tau_c} \tag{2-13}$$

Thus, in this case, the maximum amplitude of the voltage does not depend on the time constant of the Barkhausen jump and is directly proportional to the rate of flux change. This is called the "ballistic" method and indicates that the size of a Barkhausen jump can be measured from the amplitude of the induced voltage pulse.

For practical application of the Barkhausen method in nondestructive evaluation, special techniques have been developed to enable measurements to be made on the surface of the specimen. A schematic diagram of this setup is shown in Figure 2-7. With this arrangement, a cyclically varying magnetic field is applied to the specimen by means of a C-shaped magnet and a small pickup coil located in proximity to the specimen surface is used to sense near-surface Barkhausen jumps. Because of eddy current,

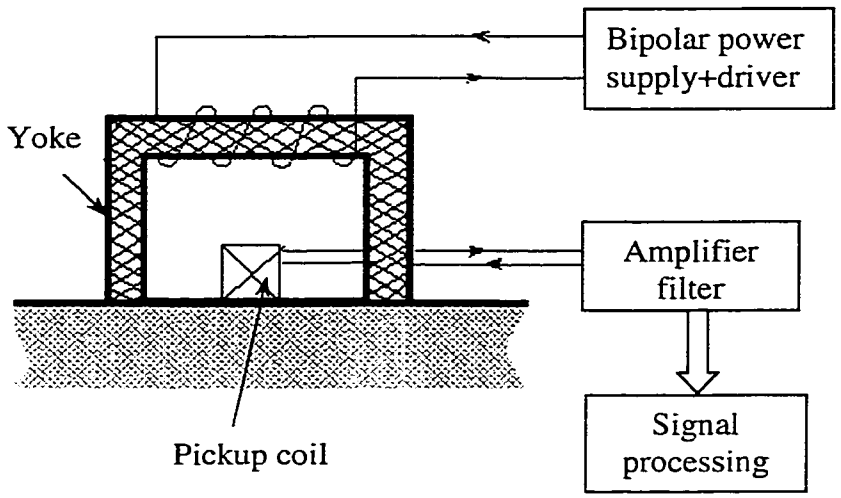

Figure 2-7 Schematic diagram for measuring Barkhausen emission

detection of jumps by this method is limited to approximately 0.3 mm depth in most structural steels.

Earlier studies [26] revealed that the surface Barkhausen noise and the encircle Barkhausen noise had similar characteristics except for a difference in amplitude of the signal. The surface Barkhausen noise is always lower than the encircle Barkhausen noise signal. This is due to the fact the surface pickup coil does not intersect the flux changes occurring in the plane of the specimen.

Bhattacharya and Vaidyanathan [30] investigated the effect of demagnetizing factor on the Barkhausen noise measurement. They concluded that a scheme for magnetizing using a yoke should be used instead of using a solenoid coil because the latter would involve a significant demagnetizing factor.

Sipahi *et al.* [31] studied the dependence of magnetic Barkhausen emission upon different excitation wave forms. They found that the frequency spectra of sinusoidal and triangular alternating field excitations showed similar behavior. However the spectrum

under square wave excitation was different due to the existence of high frequency components during square wave switching which makes it inappropriate for the Barkhausen emission measurement.

The magnetic Barkhausen noise activity was found to increase with increasing magnetizing frequency [32] because the number of domain walls participating in magnetization is linearly dependent on the square root of frequency [33]. Sipahi [34] also indicated that the superimposition of DC bias field can affect the result of Barkhausen measurement.

Thus, in developing the Barkhausen effect as a tool for nondestructive evaluation, it is essential that the features of Barkhausen emission attributable to the magnetizing parameters be carefully considered and possibly eliminated so that the signals can reveal structural information about the test material.

2.4 Applications of the Barkhausen effect

2.4.1 Stess measurement

Many of the properties of a ferromagnetic material are strongly influenced by the state of mechanical stress. Through the years, numerous efforts have been directed toward investigating the utilization of various measurable magnetic parameters as the basis of practical method for quantitatively determining the state of mechanical stress. It has been suggested that measurement of the Barkhausen effect might present a useful non-contact alternative to the measurement of stress using strain gauges.

The origin of stress dependence of Barkhausen effect lies in the interaction between strain and local magnetic moments. Because of magnetoelastic coupling [35], domains in a positive magnetostriction material, such as iron, tend to align parallel to the

stress axis under tension and perpendicular to the stress axis under compression [36]. Since the Barkhausen effect is primarily caused by irreversible movement of 180° domain walls, the increase (or decrease) in 180° domains along the direction of applied magnetic field could result in an increase (or decrease) in the Barkhausen noise amplitude, as observed experimentally [37, 38, 39]. Jagadish, Clapham and Atherton [40] measured Barkhausen emissions from a pipeline steel under tensile and compressive isotress. Pulse height distribution and power spectral analyses were performed on the Barkhausen data. The results revealed that Barkhausen events with large amplitude occurred in the presence of tensile stress, while events with small amplitude occurred under compressive stress. The power of the Barkhausen noise spectrum increased or decreased with increasing tension or compression respectively.

The Barkhausen effect also depends on the angle between uniaxial stress and magnetization direction. For a positive magnetostriction material, when stress and field directions are parallel, tension causes an increase in Barkhausen noise amplitude while compression causes a decrease; when the field is perpendicular to the stress axis, the effects of stress are reversed [29]. Kwun [41] investigated the dependence of Barkhausen noise amplitude on the angle θ between the stress and the direction of the applied magnetic field in AISI/SAE 4340, HY-80 and ASTM A-36 steels. The interesting finding in his investigation is that the Barkhausen noise amplitude measured at $\theta = 60°$ remains approximately constant despite the application of stress over a wide range. This finding indicate that the Barkhausen noise amplitude is directly dependent on the normal strain [42] along the direction of the magnetization.

The impact of uniaxial stress on the Barkhausen effect was modeled by Sablik [43]. The magnetomechanical hysteresis model [44] was utilized in this model to compute the Barkhausen noise power from the derivative of the irreversible components

of magnetization. This model was recently applied to fit results of BE measurements [45].

The dependence of Barkhausen effect on stress and the simplicity of the measurement make it a viable nondestructive technique for stress determination. However, the principal reason for the difficulty experienced in obtaining reliable stress values is the high sensitivity of BE measurement to the microstructural state of the material. The highest Barkhausen noise amplitude has been observed to occur at field strengths around the coercivity, which in turn is affected differently by the stress and microstructural features [46]. Thus, in principle this offers a means to separate the contributions from stress and microstructures. If there is no shift in the field strength at which the noise occurs, no microstructural changes are involved. If, on the other hand, a new Barkhausen noise maximum is found at a different field value, differences in microstructural constituents or their distributions are present.

2.4.2 Microstructure determination

Since its discovery, the Barkhausen effect has been researched in a wide range of ferromagnetic materials subjected to a wide variety of processing conditions. With advances in theory and experimental techniques, many attempts have been made to utilize the dependence of Barkhausen effect on material properties as a measure of those properties.

The magnetic Barkhausen event is caused primarily by sudden discontinuous motion of domain walls. During their motion, the interactions of the magnetic domain walls with microstructure parameters such as dislocations, grain boundaries and precipitate particles. under the application of an externally applied magnetic field of slowly varying intensity, may be sensed by appropriate detection means. Thus, the

magnetic Barkhausen effect provides an alternative technique for probing the microstructure of the material without having to resort to destructive techniques, such as those required for direct observation, for example by optical micrographs.

Because of its dependency on the density and nature of pinning sites within the material, the Barkhausen effect can be used to detect the precipitation of solute carbon as carbide [47]. Buttle *et al.* [23] investigated the Barkhausen effect in Incoloy 904 and found that for small inclusion, the increase of its size causes a rise in the intensity of Barkhausen emission. The maximum of the intensity appears when the inclusion size is comparable with the domain wall width. For inclusion sizes larger than the domain wall width, closure domains form at the inclusions and magnetic domain structure becomes more complicated, leading to a decrease of the pulse amplitude and intensity of the Barkhausen emission. Kameda and Ranjan [21] investigated the Barkhausen effect in a quenched and tempered steel and spheroidized steels. The results showed that increasing tempering temperature, which causes a decrease in hardness and an increase in carbide size and spacing, caused the magnetic Barkhausen peak voltage to increase. In spheroidized steels, the magnetic peak voltage was the greatest when the carbon content was 0.46wt%. These results were explained in terms of the domain nucleation and growth mechanism.

Grain size affects the magnetic properties in two ways: first, by change of domain structure due to generation of closure domains at the grain boundaries and second, by change of domain wall motion because grain boundaries present obstacles to movement of domain wall. Titto, Otala and Säynäjäkangas [48] found that the Barkhausen effect in steel is sensitive to the grain size and their results showed that the average amplitude of the Barkhausen noise increased with the increase in grain size. Gatelier-Rothéa *et al.* [49] investigated the BE in pure iron and found that the Barkhausen RMS (root mean square)

peak amplitude decreased with increasing grain size. Ranjan *et al.* [50] obtained similar results when they measured BE from nickel and decarburized steel. In nickel, the BE signal decreased with increasing grain size since grain size is the dominant microstructural parameter affecting the magnetic properties in nickel. However, in decarburized steel, the BE signal increases with increasing grain size. This is due to the presence of precipitates and grain boundary which act as nucleation sites for domains and thus the density of domain wall increases. Sakamoto, Okada and Homma [51] studied the theoretical relationships between RMS values of Barkhausen noises and the microstructure of carbon steels. Their analysis results are described as follows, in ferrite grains $RMS = Cg \times dg^{-1/2}$ and in cementite-dispersed ferrite grains $RMS = Cp \times dp^{2}$, where dg and dp are ferrite grain size and cementite particle diameter, respectively. Cg and Cp are constants.

Barkhausen effect can also be used to detect the dislocation density inside the material. In an investigation by using high voltage Lorentz microscopy [52], dislocation tangles were found to be effective pinning sites against the motion of domain walls. Ranjan, Buck and Thompson [53] studied the change in Barkhausen emission as plastically deformed nickel was annealed. The total number of Barkhausen emission reduced as annealing temperature was increased. This decrease was attributed to the reduction in the dislocation density, which would reduce the number of pinning sites for 180° domain walls. The same result has also been observed in iron by Buttle *et al.* [54]. It has also been found that the energy [55] and the low-frequency component [56, 57] of the Barkhausen noise decreased as plastic deformation progressed.

The rolling texture can also be evaluated using Barkhausen effect. Kim, Hwang and Choi [58] measured the BE signal from several polycrystalline permalloy sheets

which were cut at different angles with respect to the rolling direction. The total number of Barkhausen pulses decreased as the angle increased. Krause, Clapham and Atherton [59] suggested that the magnetic Barkhausen noise can be used to characterize the magnetic easy axis because the magnetic Barkhausen signal is sensitive to the orientation of the applied sweep field with respect to the specimen's macroscopic magnetic easy axis.

The intensity of the BE signal is also correlated with the hardness level of the material [60]. A decrease in hardness is accompanied by an increase in the intensity of the BE signal. This correlation between BE signal and hardness can be used to evaluate the surface hardening depth in carburized steels [61, 62].

Structural degradation of industrial materials is an important NDE application of the Barkhausen effect. Sundström and Törrönen [63] reported preliminary results indicating that Barkhausen effect can be used for in-service inspection of high temperature pipeline steels in power stations. The observed decrease of the Barkhausen emission intensity in the overheated areas of tested tubes correlated well with reduction of mechanical hardness level. The Barkhausen effect can also be used to monitor the fatigue damage of the material. Chen, Strom and Jiles [64] found the BE signal amplitude decreases throughout the fatigue life of the medium strength structural alloy (ASTM code A533B).

Other applications of Barkhausen effect include grinding and shot peening. Grinding may cause the surface of the material to become over-tempered which is called retempering burn, or to become over-hardened which is called rehardening burn. Both of these changes can be detected by means of Barkhausen emissions [65, 66]. Shot peening as a surface treatment for extending fatigue life can also be monitored by means of Barkhausen effect inspection [67].

The Barkhausen effect has been clearly established as a viable technique for microstructural changes evaluation. However, the physical mechanisms for microstructural influences on the Barkhausen effect need to be further elucidated and understood.

2.5 Conclusion

Due to the strong interaction between individual magnetic moments, the ferromagnetic material consists of large number of magnetic domains, in which all magnetic moments are aligned along the same direction. These magnetic domains align randomly before magnetization. Under the action of magnetic field, the domains rotate and the domain boundaries, or domain walls, move. However the domain rotation is impeded by anisotropy energy and the motion of domain walls is impeded by the pinning sites. Both processes are responsible for magnetic hysteresis and Barkhausen effect.

The microstructural factors, such as grain boundaries, dislocations, inclusions and volumes of second phase material, which act as pining sites to impede the motion of domain walls, can significantly change magnetic properties. Therefore, BE signals are very sensitive to the change in microstructure of the material and can be used to assess the microstructure of ferromagnetic materials.

3 MULTI-FUNCTIONAL MAGNETIC BARKHAUSEN EMISSION MEASUREMENT SYSTEM

3.1 Introduction

The measurement of magnetic Barkhausen emission of materials has received little attention in the past. Nevertheless it is now becoming of increasing interest, particularly in the area of nondestructive evaluation or material assessment. It has been realized that the form of the Barkhausen effect signal is closely related to the microstructure and stress state of the material, and therefore measurement of the BE signal can be used to evaluate the microstructure or stress level of the material.

Efforts have been focused on the relationship between the BE measurement parameters such as RMS voltage or amplitude of Barkhausen signals and their dependence on the various changes in microstructure or stress [68, 69, 70]. Theoretical models of Barkhausen effect by Bertotti *et al.* [6, 7, 8] and by Jiles *et al.* [10, 71] allow various characteristics of Barkhausen signals such as the variance, pulse height distribution and power spectral density to be described mathematically. This provides a basis for a more fundamental understanding of the phenomenon and allows the relationship between the characteristics of BE signal and other properties of materials (*e.g.* coercivity, permeability) to be studied. The advance in the understanding of Barkhausen effect also suggests the need for further development of measurement systems that can be used to measure various characteristics of Barkhausen effect for comparison with theoretical modeling results.

In this study a new computer-controlled system, for making BE measurement on materials has been developed. This was based on our previous Magneprobe system [72].

This new system provides the capability for making BE measurements using various settings and analyzing the results in a variety of ways. Measurements can be made easily and rapidly through the use of custom designed system software. Various inspection procedures were implemented into the software in modular form. New procedures can therefore be easily added, allowing evolution of the instrument to meet new needs.

3.2 Main contribution: System design

The new system was designed for easy and rapid detection and analysis of BE signal from materials for non-destructive evaluation. The versatility of the system arises from the fact that it offers a range of embedded software based analysis techniques. System development included the hardware for generating an alternating magnetic field and detection of the BE signal, and software for instrument control and data analysis. Furthermore, this system can be used to sample the BE signal at a rate of 5MHz with a voltage resolution of 1.2mV (14bit, 5V full scale). This represents a significant improvement over the previous 400kHz, 12bit system [72]. The algorithms embedded in the software enable rapid collection and analysis of the BE signals measured under precisely controlled condition.

3.2.1 Principles of operation

The system broadly consists of two modules, the magnetizing module and the detection module. All major components of this system are controlled from the computer. In the magnetizing module, an alternating signal is generated by the waveform generation card and amplified by the Kepco power supply. This signal enters the excitation coil of the sensor and generates an alternating magnetic field within the c-core magnet which is then coupled into the test material. Discontinuous changes in magnetization occur in the

test material generating the so-called BE signal which is detected by a pick-up coil. Then the signal is amplified, bandwidth limited using analog filters, and digitized by the data acquisition card for further analysis. The data can also be stored on hard disk.

3.2.2 Hardware components

To prepare for a measurement, the hardware needs to be set up. A schematic diagram of the hardware configuration is shown in Figure 3-1. The whole system, except the computer, measures approximately 20"× 20"× 16" and weighs about 60 pounds. Its major components include a two-channel arbitrary waveform generation (AWG) card which can generate signals at up to 10MHz with a frequency resolution of 0.012% and an accuracy of ±0.012% of the frequency used. The signal amplitude range is 20V peak-to-peak and the resolution is 0.05% of the full scale.

Seven third order Butterworth low-pass filters with a range of fixed cutoff frequencies from 10kHz to 10MHz are embedded on each output channel of the AWG card to ensure high spectral purity of the excitation signal. This card can be used to produce any form of excitation signal in order to excite Barkhausen events. The excitation signal is amplified by a bipolar power supply and is delivered to the excitation coil which is wound on a c-core magnet. The Barkhausen signal detected by a pick-up coil is amplified and filtered using a high-pass filter to remove the low frequency interference such as that coupled from the excitation coil and 60Hz power line frequency noise. The low-pass filter then removes high frequency electrical noise and its harmonics. The voltage gains of the filters can be adjusted to provide additional amplification of the signal. A GPIB card is used to communicate with the programmable filter unit which has

a frequency range from 1Hz to 2MHz. The output signal of the band-pass filter is fed to the channel-0 of a high performance PCI data acquisition card which allows accurate sampling of the BE signals.

This card has two simultaneous (14-bit, 2.5V full-scale voltage input, 5MHz sampling rate) A/D channels and the input section of each channel connects to a very high speed, wide-band low noise amplifier. In order to obtain consistent measurement results the voltage signal across a resistor R_{sensor}, which is in phase with the excitation

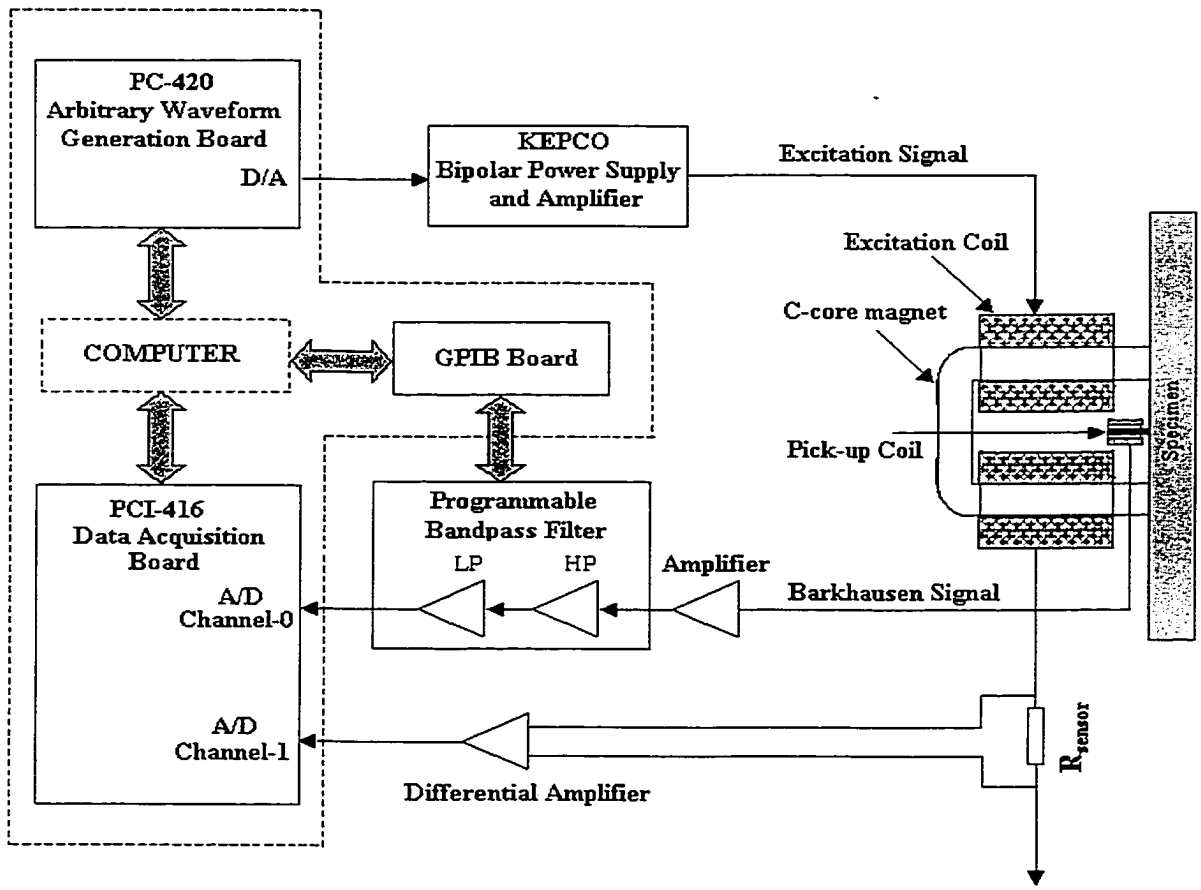

Figure 3-1 Block diagram of system hardware

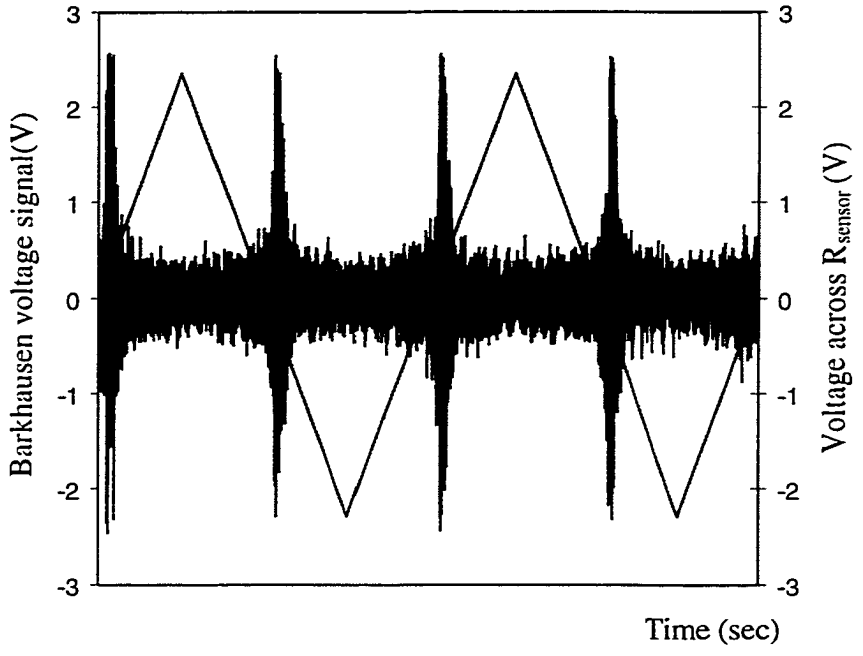

Figure 3-2 Triangular excitation current signal and detected Barkhausen signal plotted as function of time

current, is input to the A/D channel-1 on the data acquisition card (as shown in Figure 3-1) and used as the trigger signal. The system starts collecting BE data when this trigger signal passes the zero crossing point during the rising edge. This guarantees that the acquired BE signal always has the same phase relationship with the excitation current. Figure 3-2 shows the relationship between the excitation current and the Barkhausen signal obtained from a plain carbon steel sample (0.2wt% C).

3.2.3 Software

The unique capabilities of the new system are derived largely from the control and data analysis software – Magsoft, which is a 32 bit application program written in

Visual C++ 6.0 under the Windows 98 environment. The user interface for the software is shown in Figure 3-3. From the user interface, the operator can change the settings of measurement and run the signal processing routine to analyze the acquired data. Measurement conditions can be specified by changing the settings of the waveform generation module, the data acquisition module and the filter setting module. The waveform generation module allows setting the amplitude, frequency and offset of the excitation signal. The data acquisition module allows setting sampling clock rate, clock source (internal or external), number of sampling cycles, trigger rate and trigger source for the A/D card. The filter setting module is used to send GPIB commands to the filters to control the filter settings including the input and output gains, frequency range, filter mode (high-pass, low-pass, band-pass or band-reject) and filter type (Elliptical, Butterworth or Bessel). The structure of the software is shown in Figure 3-4.

Figure 3-3 Software user interface

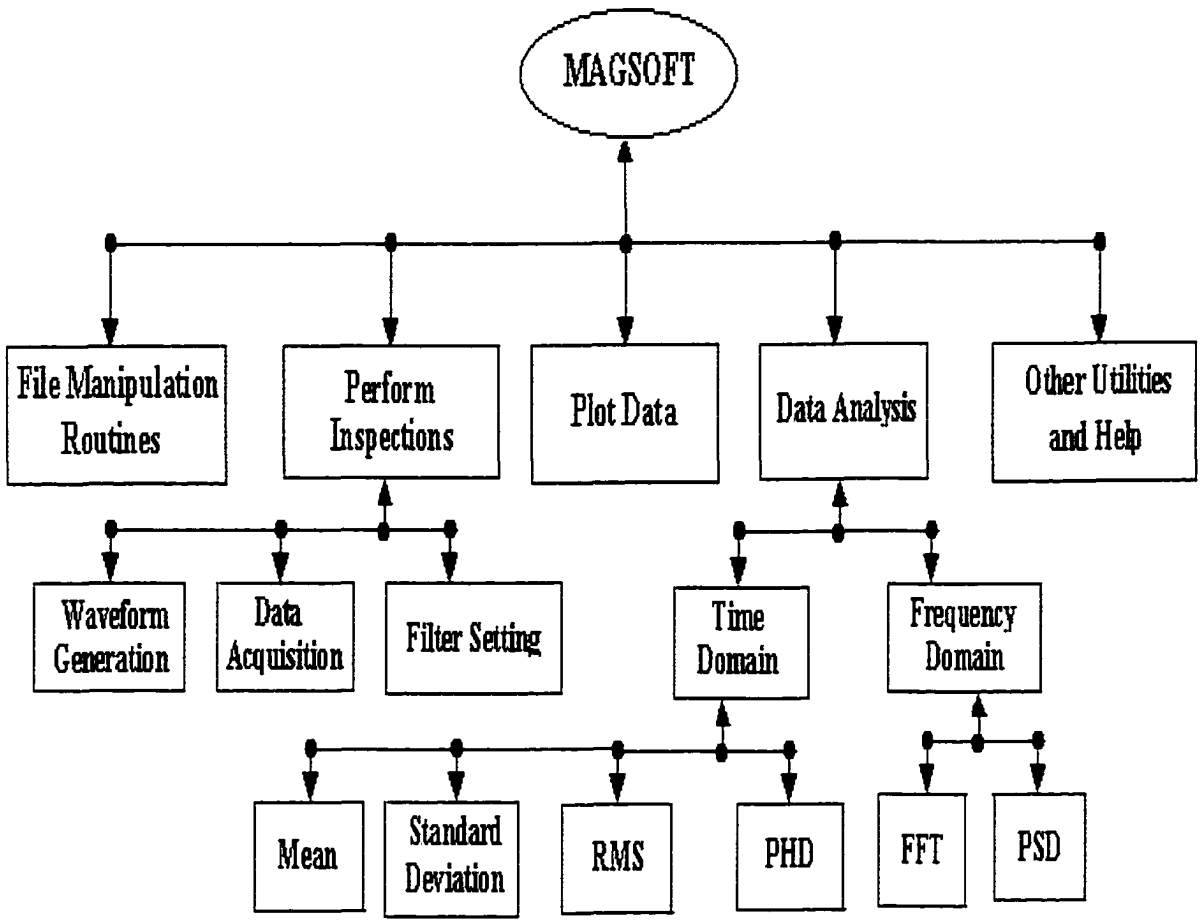

Figure 3-4 Block diagram of system software hierarchy

The acquired data can be analyzed by a number of algorithms to give standard deviation, Root Mean Square (RMS), Fast Fourier Transform (FFT), Power Spectral Density (PSD) and Pulse Height Distribution (PHD) of the BE signals. These results of the analysis of the BE signal in the time and frequency domain can also be displayed on the screen and saved to data files for further analysis. An operator manual has been prepared to guide the users through the details of operating the instrument [73].

3.3 Signal processing algorithms

3.3.1 Frequency spectrum

A physical process can be described either in the time domain, by the values of some quantity h as a function of time t (i.e. $h(t)$), or in the frequency domain, where the process is specified by giving its amplitude H as a function of frequency f, that is $H(f)$, with $-\infty<f<+\infty$. For many purposes it is useful to think of $h(t)$ and $H(f)$ as being two different representations of the same function. The relationship between these two representations are given by the Fourier transform equations,

$$\begin{aligned} H(f) &= \int_{-\infty}^{+\infty} h(t) e^{2\pi i f t}\, dt \\ h(t) &= \int_{-\infty}^{+\infty} H(f) e^{-2\pi i f t}\, df \end{aligned} \tag{3-1}$$

In the most frequently encountered situation, function $h(t)$ is sampled at evenly spaced intervals in time. Let Δ denote the time interval between two consecutive sampled data, so that the sequence of sampled values is

$$h_n = h(n\Delta) \qquad n = \ldots,-3,-2,-1,0,1,2,3,\ldots \tag{3-2}$$

The reciprocal of the time interval Δ is called the sampling rate.

For any sampling interval, there is also a special frequency f_c, called the Nyquist critical frequency, which is given by

$$f_c = \frac{1}{2\Delta} \tag{3-3}$$

The sampling theorem states that if a continuous function $h(t)$, sampled at an interval Δ, happens to be bandwidth limited to frequencies smaller in magnitude than f_c, then the

function $h(t)$ is completely determined by its sampled values h_n. However, if the function $h(t)$ is not bandwidth limited to less than the Nyquist critical frequency, any frequency component outside the frequency range $(-f_c, f_c)$ is aliased into that range. Once the signal has been sampled, it is difficult to remove aliased component. The way to overcome aliasing is to (i) know the natural bandwidth limit of the signal, or enforce a known limit by analog filtering of the continuous signal. (ii) sample at a rate sufficiently rapid (*i.e.* extend the Nyquist frequency).

The Fourier transform of a function $h(t)$ can be estimated from a finite number of its N consecutive sampled values:

$$h_k = h(t_k), \qquad t_k = k\Delta, \qquad k = 0, 1, 2, \ldots, N-1 \tag{3-4}$$

The corresponding discrete Fourier transform (DFT) is estimated only at the discrete values f_n:

$$f_n = \frac{n}{N\Delta} \qquad n = -\frac{N}{2}, \ldots, \frac{N}{2} \tag{3-5}$$

and can be described as:

$$H(f_n) = \int_{-\infty}^{+\infty} h(t) e^{2\pi i f_n t} dt \approx \sum_{k=0}^{N-1} h_k e^{2\pi i f_n t_k} \Delta = \Delta \sum_{k=0}^{N-1} h_k e^{2\pi i k n / N} \tag{3-6}$$

Computing the value of $H(f_n)$ in equation (3-6) is a matrix multiplication requiring the order of N^2 operations. The DFT can, in fact, be computed in the order of $N\log_2 N$ operations with an algorithm called the fast Fourier transform (known as "FFT"). The difference between $N\log_2 N$ and N^2 is immense. With $N = 10^6$, for example, it is the difference between, roughly, 10 seconds of CPU time and 2 days of CPU time on a Pentium 400MHz computer. The FFT program provided in [74] was used in this study to

analyze the BE signal. The results show that most of the frequency components of the Barkhausen signal are distributed from several kiloHertz to a few hundred kiloHertz.

3.3.2 Power spectrum

In the frequency domain, the total power in a signal is given by

$$\int_{-\infty}^{+\infty}|H(f)|^2 df \tag{3-7}$$

Frequently, one wants to know the power spectral density, that is how much "power" is contained in the frequency interval between f and $f+df$. In such circumstances one does not usually distinguish between positive and negative f, but rather regards f as varying from 0 to $+\infty$. In such cases, the power spectral density (PSD) of the function f is defined as

$$P(f) = |H(f)|^2 + |H(-f)|^2 \qquad 0 \le f \le +\infty \tag{3-8}$$

so that the total power is just the integral of $P(f)$ from $f=0$ to $f = +\infty$. When the function $h(t)$ is real, the PSD is defined as

$$P(f) = 2|H(f)|^2 \tag{3-9}$$

Equations (3-8) and (3-9) give estimations of power spectral density. The value of $P(f_k)$ does not equal to the continuous $P(f)$ at exactly f_k, since f_k is supposed to be representative of a whole frequency bin extending halfway from the preceding discrete frequency to halfway to the next one. The solution to this problem is to apply a nonrectangular data window to the sections prior to computing the PSD. The Hann, Bartlett or Welch windows [74] are usually used to calculate the PSD.

For the present system, the Welch window [74] was chosen. This is advantageous

because it makes the tails of the distribution fall off very rapidly. The equations for the PSD estimation become

$$
\begin{aligned}
D_k &= \sum_{j=0}^{N-1} h_j w_j e^{2\pi ijk/N} \qquad k = 0,\ldots,N-1 \\
P(f_0) &= \frac{1}{W_{ss}}|D_0|^2 \\
P(f_{N/2}) &= \frac{1}{W_{ss}}|D_{N/2}|^2 \\
P(f_k) &= \frac{1}{W_{ss}}\left[|D_k|^2 + |D_{N-k}|^2\right] \qquad k = 1,2,\ldots,(\frac{N}{2}-1)
\end{aligned}
\tag{3-10}
$$

where h_j, $j=0,1,\ldots,N-1$ is the input data and W_{ss} stands for "window squared and summed" which is defined as

$$W_{ss} = N\sum_{j=0}^{N-1} w_j^2 \tag{3-11}$$

For the Welch window, the w_j is given by

$$w_j = 1 - \left(\frac{j - \frac{1}{2}N}{\frac{1}{2}N}\right)^2 \tag{3-12}$$

3.3.3 Root mean square (RMS)

The RMS voltage of the BE signal can be easily computed from the raw Barkhausen data as

$$RMS = \sqrt{\frac{1}{N}\sum_{i=1}^{N} x_i^2} \tag{3-13}$$

where N is the total number of acquired points and x_i is the *i-th* sampled Barkhausen data.

The RMS voltage measurement provides an easy and fast way to observe the BE signal. However, the main drawback of the RMS voltage is its insensitivity to the actual detailed structure of the BE signal. The RMS voltage may be the same for a strong BE signal of short duration or a weak signal of large duration. Hence, the RMS voltage may not provide much detailed information about the true variation of the BE signal, and hence gives only limited information about the structure of the material.

3.3.4 Pulse height distribution (PHD)

To obtain the PHD of the Barkhausen voltage signal, a series of amplitude bins were set up between the minimum and the maximum of the Barkhausen pulses amplitude. The number of pulses that fall into each bin were counted and plotted as a function of the average voltage amplitude in that bin. If the number of bins is large enough, pulse-height distribution can give a proper assessment of the BE signal and has been used frequently to obtain material-dependent information.

3.4 Main contribution: Experimental results

3.4.1 Experimental details

In this study, the system was used to investigate the effects of varying microstructure of plain carbon steel samples on BE signals. Two samples, namely S1 and S2, were used in the experiment. The dimensions of these samples are shown in Figure 3-5. The carbon contents of the samples are listed in Table 3-1. Both samples were found to have a ferrite/pearlite structure. The volume fraction of pearlite V_p of the samples were measured and the results are listed in Table 3-1. Barkhausen measurements were made using a 2Hz excitation signal with triangle waveform generated by the AWG

card. The lower and higher cut-off frequencies of the filters are 5kHz and 250kHz respectively. Voltage gains of 10dB and 40dB were used in the high-pass and low-pass filtering stages respectively. The filtered signal was sampled at 500kHz using an internal clock.

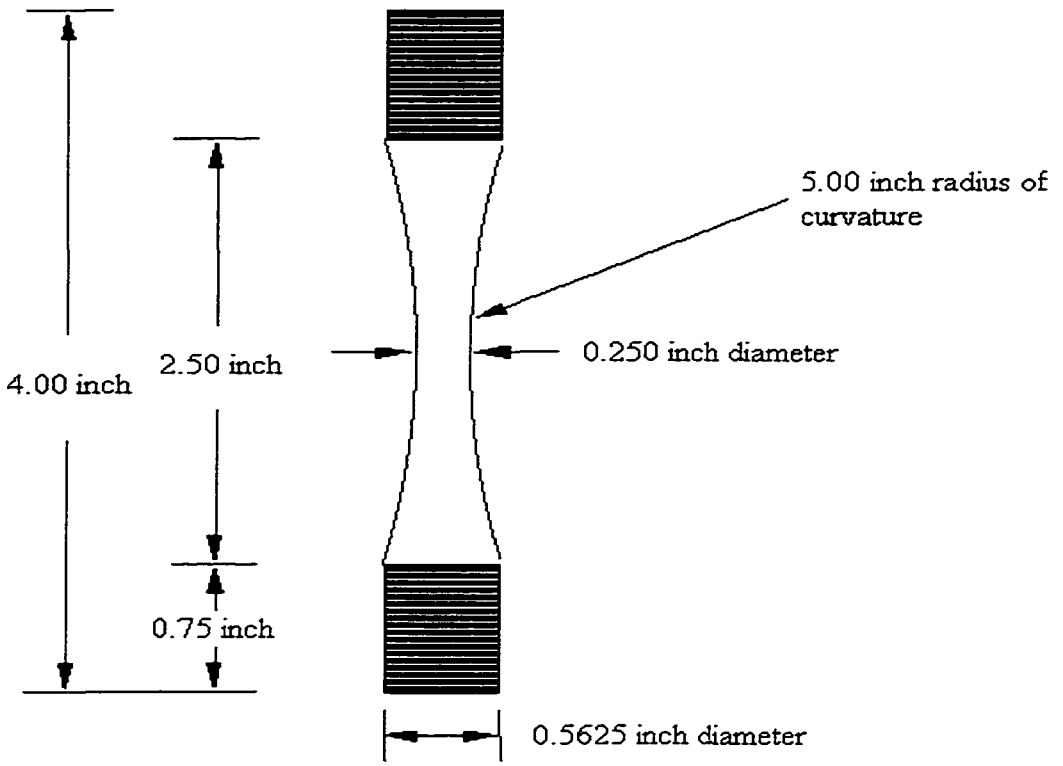

Figure 3-5 The dimensions of the test samples

Table 3-1 Carbon content and microstructure

Sample	Carbon content (wt%)	Volume fraction of pearlite V_p (%)
S1	0.20	17
S2	0.45	56

3.4.2 Results and discussion

The BE signals and the corresponding RMS values measured from the samples S1 and S2 are shown in Figure 3-6 and Figure 3-7 respectively.

The PHD spectra of the BE signals measured from the samples are shown in Figure 3-8. The PHD spectra of the two samples were very similar in the low amplitude

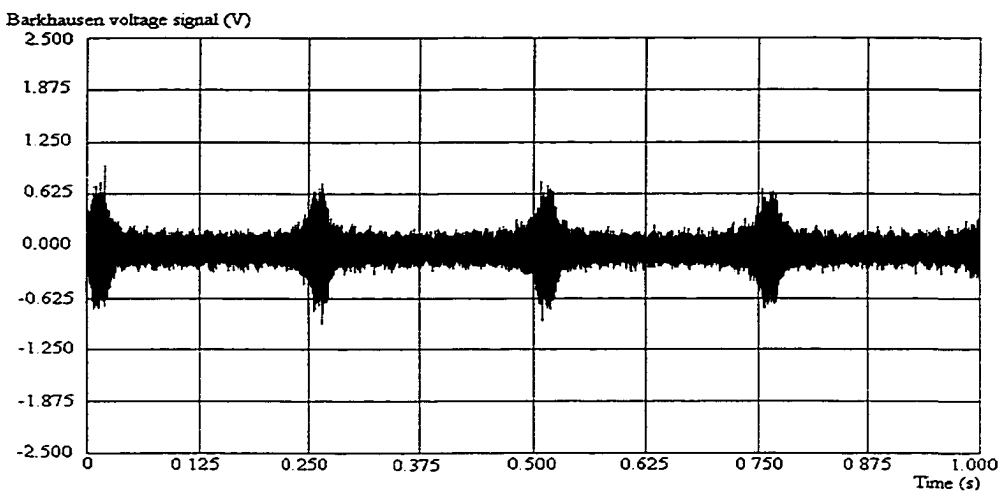

Figure 3-6 Barkhausen signal from S1 (RMS:97mV)

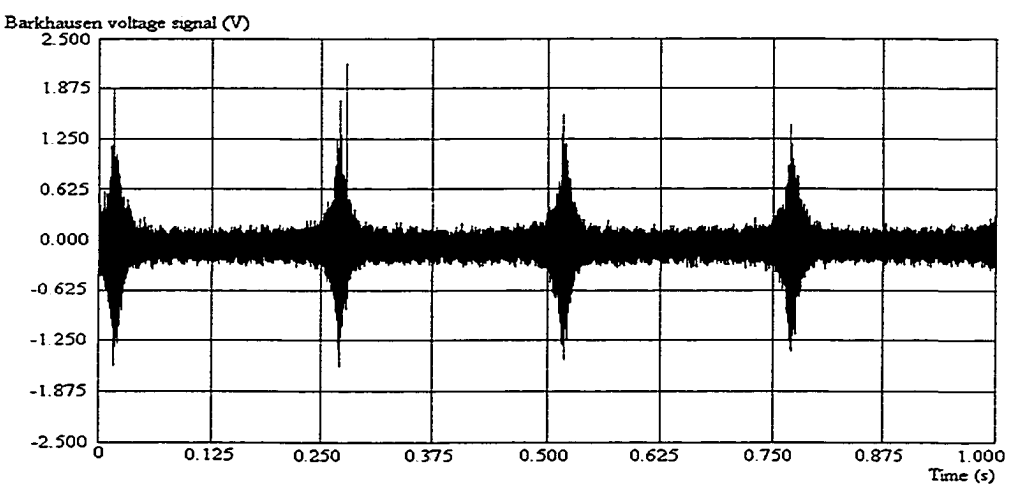

Figure 3-7 Barkhausen signal from S2 (RMS:132mV)

regime of Barkhausen pulses (up to 0.3V). This is attributed to the dominance of the background noise in the acquired signals in this regime as indicated in Figure 3-9, which shows the PHD of the background noise measured by sampling the input signal to the A/D card without applying any excitation field to the samples. Important information about the Barkhausen pulses can be extracted from the PHD spectra in the high amplitude regime (signal pulses larger than 0.2V as indicated by "A" in Figure 3-8).

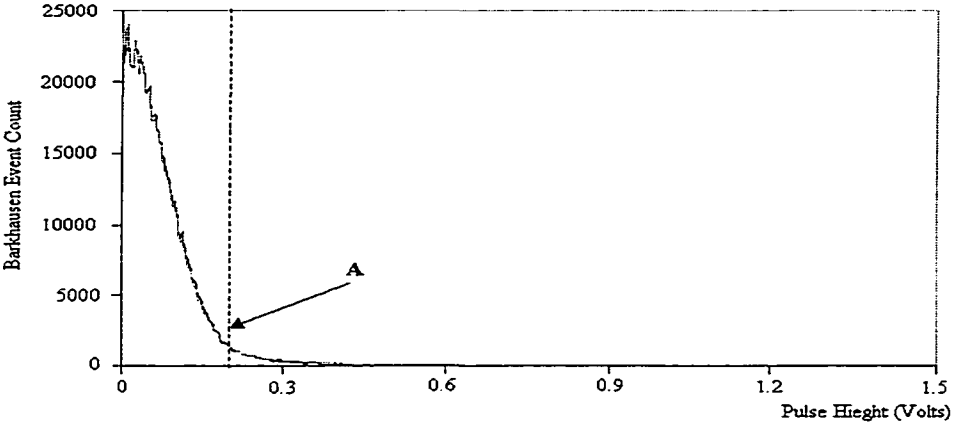

Figure 3-8 Pulse height distribution of BE signal measured from the sample S1 and S2

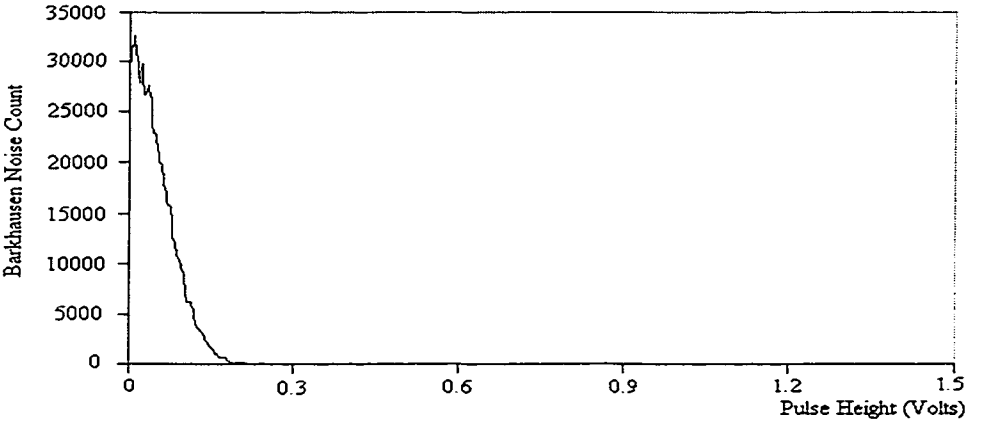

Figure 3-9 Pulse height distribution of background noise

As Figure 3-10 shows, the PHD spectrum of the BE signal of S2 displays a long tail extending to larger pulse heights than that of S1. The present results are consistent with the results obtained in a previous study of BE signals in plain carbon steels with different pearlite contents [75], and can be explained in terms of the difference in pearlite content between the samples.

A Barkhausen event, or pulse, can be interpreted as individual or collective jumps of domain walls as they overcome pinning sites. The larger the jump following unpinning, the stronger the voltage pulse induced in the pickup coil corresponding to that jump. It has been shown that cementite lamellae in pearlites are strong pinning sites for domain walls [76]. Therefore, the domain walls in S2, which had higher pearlite content, experienced stronger pinning forces than those in S1. During the hysteresis cycle, once the local fields exerting on the domain walls in S2 overcome the pinning forces these domain walls can jump further than those in S1 before they become pinned again. This gave rise to stronger Barkhausen jumps in S2 than in S1 as shown in Figure 3-6 and Figure 3-7, and thus accounts for the wider range of Barkhausen jump size in S2 than in S1.

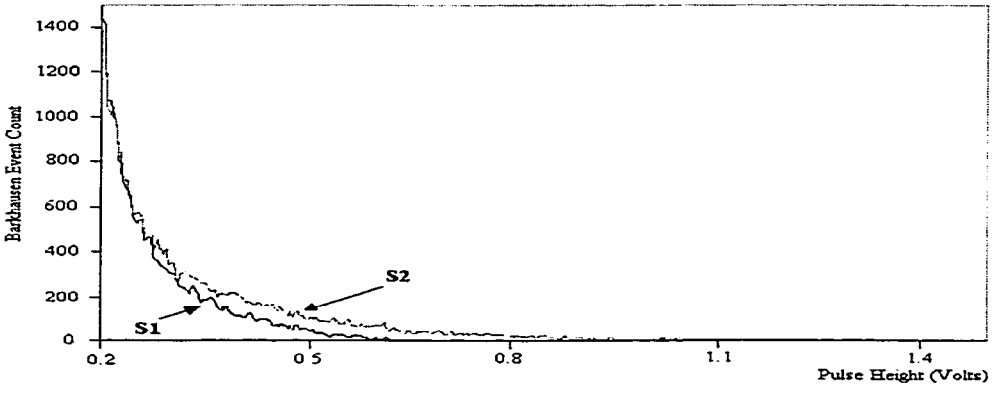

Figure 3-10 Pulse height distribution of Barkhausen signals in high amplitude range (pulse height>0.2V)

The BE profiles, which were obtained by averaging the rectified Barkhausen signals over 300 hysteresis cycles, are shown in Figure 3-11 and Figure 3-12 respectively for the sample S1 and S2. The BE profile of S1 was found to have two resolvable voltage peaks in the time domain, while the BE profile of S2 showed a single sharp peak. Similar BE profiles have been reported in a previous study [30] and can be explained as follows.

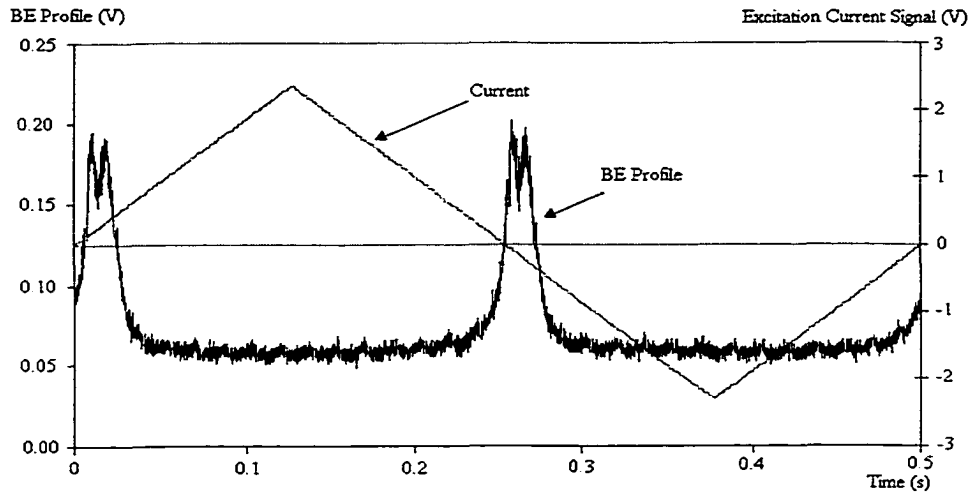

Figure 3-11 BE profile over one hysteresis loop for S1

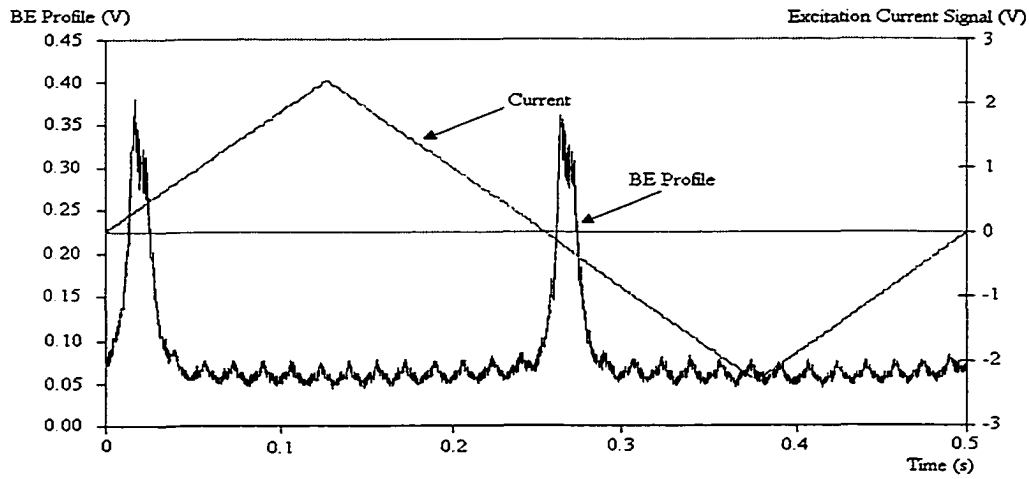

Figure 3-12 BE profile over one hysteresis loop for S2

In sample S1, there were fewer impediments for domain growth after domains were nucleated than in S2. Thus, in S1, the domains after nucleation can grow easily because the impedance to domain wall motion in the form of dispersed carbides is less. This rapid growth of domains gave rise to the first peak in the profile. Once the domains extend beyond the grains, significant changes in domain patterns occur when a reverse magnetic field strength is present for domain annihilation to take place. This accounts for the second peak in the BE profile. However, in sample S2, after domains were nucleated they were unable to grow until the applied magnetic field strength was reversed because of the wide presence of impediments to domain wall motion. Therefore, the observed differences in BE profiles between these two samples suggests that the samples have different magnetization processes occurring around the hysteresis loop.

3.5 Conclusion

A new multi-functional system for measurement of Barkhausen emission has been developed as part of the research for this thesis. The improved hardware of this system together with the procedures incorporated into the software allow flexible control of applied fields and multivariate analysis of the BE signals.

Furthermore, Barkhausen emissions measured on two plain carbon steels with different carbon contents showed differences which indicates that Barkhausen effect can be used as a method for nondestructive material characterization.

4 EVALUATION OF WEAR-INDUCED MATERIAL LOSS IN CASE HARDENED STEEL

4.1 Introduction

From the mechanics of materials it is known that the surface layer plays an important role in determining the mechanical properties of components as the loading is often distributed disproportionately on the surface layer. For engineering applications steel components often need to have a good toughness in the core to resist impacts and have a hard surface to resist wear. From a metallurgical point of view, these properties are contradictory. In the case of carbon steels, the former requires a low carbon content, while the latter requires a high carbon content. This is often solved by means of surface hardening to get different microstructures on the surface and in the core. This has another advantage because less expensive low-carbon and medium-carbon steels can be surface hardened without distortion and cracking associated with the hardening.

Material loss is a major problem in many engineering applications. Case-hardened steel components are frequently used in high wear applications to minimize the rate of material loss in situations where friction occurs between moving parts. Ultimately the material loss leads to failure of components because they can no longer sustain the intended levels of stress. Therefore, monitoring of wear rates non-destructively would allow components to be replaced before failure.

Here we report on BE measurements on well-controlled laboratory steel samples with different case depths in order to demonstrate the relationship between the BE signal and the amount of material removed from the case-hardened steel. The BE signal was measured and analyzed by our new measurement system introduced in chapter 3. The

results demonstrate the feasibility of using BE measurement for monitoring wear-induced material loss.

4.2 Background

4.2.1 Carbon content and diffusion time

It is known that during surface carburization, the concentration of carbon below the surface and the depth of carburization vary continuously with exposure time as shown in Figure 4-1. This process is governed by the diffusion equation known as Fick's law [77]. The formal mathematical treatment of such diffusional flow is expressed as

$$\frac{\partial c}{\partial t} = \frac{\partial}{\partial x}(D\frac{\partial c}{\partial x}) \quad . \tag{4-1}$$

where c is the carbon concentration, x is the distance below the surface, t is the exposure time and D is the diffusion coefficient.

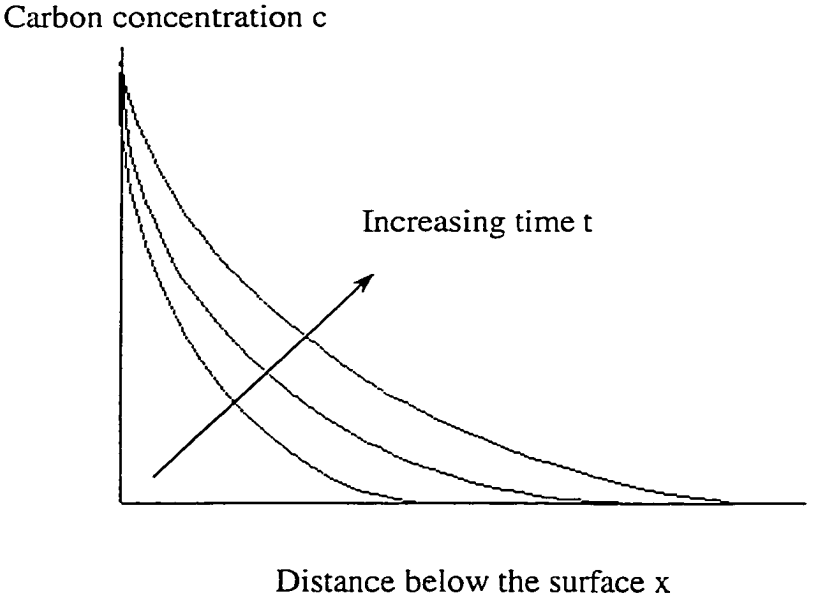

Figure 4-1 Schematic diagram of variation in carbon concentration with carburizing time

For given process conditions and material, the subsurface carbon concentration and the depth of carburization can be related or estimated experimentally, as well as theoretically, based on the phenomenon of diffusion. This subsurface concentration strongly influences the hardness of the material as a function of depth and could affect the level of the BE signal since it has been shown that BE signal is related to the hardness of steel [60]. Thus, surface BE measurement can be related to the changes in the subsurface carbon concentration and hence, with appropriate calibration, the depth of material loss can be estimated.

4.2.2 Penetration depth

When electromagnetic signals pass through electrically conducting materials, they are rapidly attenuated by eddy current damping. This can be demonstrated in the simplest case by considering the attenuation of a plane sinusoidal electromagnetic field of angular frequency ω impinging on a semi-infinite plane surface of a material with conductivity σ, permittivity ε and relative permeability μ_r. Under these conditions the magnetic field obeys the equation

$$\nabla^2 \boldsymbol{H} - \sigma\mu_0\mu_r \frac{\partial \boldsymbol{H}}{\partial t} - \varepsilon\mu_0\mu_r \frac{\partial^2 \boldsymbol{H}}{\partial t^2} = 0 \quad , \tag{4-2}$$

which is a wave equation in which the damping term is $\sigma\mu_0\mu_r \frac{\partial \boldsymbol{H}}{\partial t}$. The solution to (4-2) has the form

$$B = B_0 \exp[i(\alpha z - \omega t)]\exp(-z/\delta) \quad , \tag{4-3}$$

where $\alpha = 2\pi/\lambda$ is the wave number and δ is the skin depth at which the amplitude of the field decays to $1/e$ (i.e. 0.3679) of its value at the surface and is given by

$$\delta = \sqrt{\frac{2}{\varpi \sigma \mu_0 \mu_r}} \quad . \tag{4-4}$$

For a material such as steel with typical permeability μ_r=50, conductivity σ=10^6 $(\Omega m)^{-1}$, the values of the plane wave skin depth at different frequencies has the values shown in Table 4-1. It is clear from the results of Table 4-1 that the penetration depth of BE signals, which are typically in the range of 10kHz – 500kHz, is very limited in electrically conducting magnetic materials such as iron. Therefore detected BE signal are likely to have originated from depths not greater than about 0.3mm in low permeability, low conductivity (μ_r=50, σ=5×10^6 $\Omega^{-1}m^{-1}$) material or from depths not greater than 0.02mm in high permeability, high conductivity iron (μ_r=5000, σ=10×10^6 $\Omega^{-1}m^{-1}$). As a result of this the measurement of BE signals can only be used for characterization of the near surface region.

4.2.3 Barkhausen effect and hardness

Magnetic Barkhausen emissions occur in ferromagnetic materials subjected to magnetic fields. The phenomenon is attributed mostly to the irreversible movement of

Table 4-1 Penetration depths at different frequencies for steel with μ_r=50, σ=10^6 $\Omega^{-1}m^{-1}$

Frequency (kHz)	Penetration Depth δ (mm)
10	0.7
50	0.3
100	0.2
500	0.1

magnetic domain walls as they overcome the potential barriers in their path during magnetization. In real materials not all domain wall motion is planar, particularly because of the effects of inhomogeneities such as pinning sites for domain wall motion. When a magnetic domain wall has relatively low domain wall surface energy γ and is subjected to pinning, the domain wall will bend under the action of an applied magnetic field.

As shown by Jiles [78], in a simplified case such as two dimensional or cylindrical deformation of the domain wall, shown in Figure 4-2, the radius of curvature R of the bowing wall can be expressed in terms of the angle subtended by the section of the wall θ as

$$R = \frac{L}{2\sin\theta} \quad , \tag{4-5}$$

and the excess pressure P across a cylindrical domain wall is then given by

$$P = \frac{\gamma}{R} = \frac{2\gamma\sin\theta}{L} \quad . \tag{4-6}$$

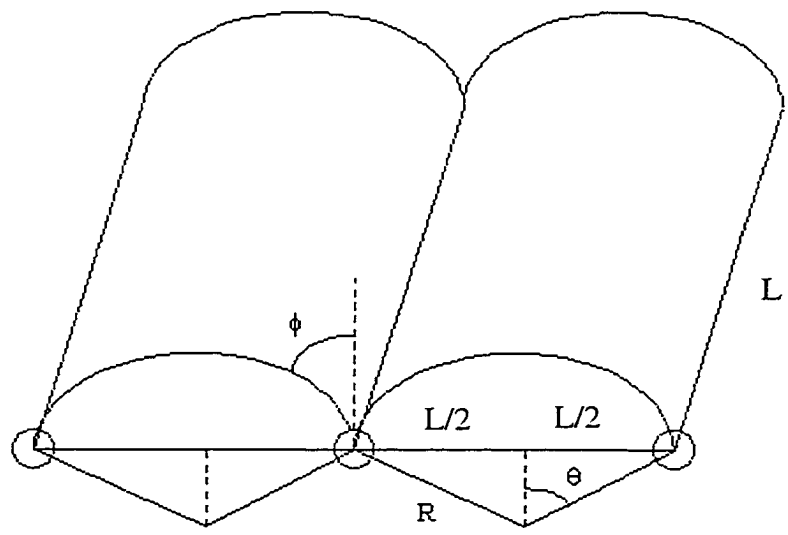

Figure 4-2 Domain wall bending along three line defects

From simple geometrical consideration the angle ϕ, which is half the angle between the sections of the two walls at the pinning sites, is given by $\phi = \frac{\pi}{2} - \theta$. Therefore the pressure across the wall is

$$P = \frac{2\gamma \cos\phi}{L} \quad , \tag{4-7}$$

and the net force on the pinning line of length L is then $F = 2\gamma L \cos\phi$.

The force on the domain wall due to an applied magnetic filed $\boldsymbol{H}$ can be calculated from the excess pressure across the curved interface. In the general case of two domains oriented at arbitrary angles to the field, this pressure can also be expressed in terms of the applied magnetic field $\boldsymbol{H}$, the magnetic moment per unit volume M_s and the angles between the magnetic moments and the applied field on either side of the domain wall Ω_1 and Ω_2

$$P = \mu_0 M_s H(\cos\Omega_1 - \cos\Omega_2) \quad . \tag{4-8}$$

A positive pressure on the wall indicates that domain 1 (angle Ω_1) is more favorably aligned with the magnetic field $\boldsymbol{H}$ than domain 2 (angle Ω_2). Equating the terms for the pressure across the domain wall, from (4-7) and (4-8)

$$P = \frac{2\gamma \cos\phi}{L} = \mu_0 M_s H(\cos\Omega_1 - \cos\Omega_2) \quad , \tag{4-9}$$

and therefore

$$2\gamma \cos\phi = \mu_0 M_s HL(\cos\Omega_1 - \cos\Omega_2) \quad . \tag{4-10}$$

Since the force on the dislocation of length L is $2\gamma L \cos\phi$

$$2\gamma L \cos\phi = \mu_0 M_s HL^2(\cos\Omega_1 - \cos\Omega_2) \quad . \tag{4-11}$$

Expressing this in terms of force per unit length, the equation becomes

$$F^{\cdot} = \frac{F}{L} = \mu_0 M_s HL(\cos\Omega_1 - \cos\Omega_2) = 2\gamma\cos\phi \quad . \tag{4-12}$$

Each dislocation will have a critical value of the pinning force per unit length $F_c^{\cdot}$, beyond which the domain wall breaks away from the pinning site. Depending on the magnitude of $F_c^{\cdot}$, the domain wall will either break away from the pinning site at a critical angle ϕ_c, or if the pinning is very strong or the domain wall surface energy very weak, the angle will reach 0° and the two surface of the domain wall will coalesce before the wall breaks away from the pinning site. If $F_{crit}^{\cdot}$ is the critical stress needed to break the domain wall away from the dislocation, in Nm^{-1}, then this can be expressed as

$$F_{crit}^{\cdot} = 2\gamma\cos\phi_{crit} \quad , \tag{4-13}$$

which shows that for a given critical angle the critical force per unit length $F_{crit}^{\cdot}$ increases linearly with the surface energy γ of the domain wall.

$F_{crit}^{\cdot}$ and the force exerted on the pinning site by a domain wall can be used to determine a critical field strength H_{crit} that is needed to break a domain wall away from a dislocation or pinning site as follows

$$2\gamma\cos\phi_{crit} = \mu_0 M_s LH_{crit}(\cos\Omega_1 - \cos\Omega_2) \quad . \tag{4-14}$$

The critical field is therefore given by

$$H_{crit} = \frac{2\gamma\cos\phi_{crit}}{\mu_0 M_s L(\cos\Omega_1 - \cos\Omega_2)} \quad . \tag{4-15}$$

This means that the critical field strength for Barkhausen activity decreases as the

spacing L between pinning sites increases. Therefore Barkhausen activity is easier to generate when the density of dislocations is low. In addition the domain wall will move further when dislocation density is low. Therefore we have the basis of an explanation of high hardness giving high dislocation density and consequently low Barkhausen signal, and vice versa [78].

4.3 Main contribution: Material loss evaluation using BE measurement

In case-hardened steels, the high carbon content in the surface layer increases the number of defects and pinning sites, and hence increases the hardness. These pinning sites can also impede the movement of domain walls and thus alter the BE signals. Therefore, in principle, measurement of BE signals should be useful for evaluation of case depth on surface modified steels and this has been shown to be possible in earlier studies [61, 79, 80].

In this study, three gas-carburized 8620 steel samples (designated 1, 2 and 3) were used. Sample 1 and 2 are steel disks with a diameter of 75mm and a thickness of 10mm. which have nominal case depths of 1.03mm and 1.24mm respectively. A smaller sample (sample 3) of diameter 32mm was cut from the third steel disk in order to fit into the auto electrical-polisher. Sample 3 has a nominal case depth of 1.07mm. All of these specimens have the same compositions which are (in wt%): 97.75 Fe; 0.8 Mn; 0.5 Ni; 0.5 Mo; 0.2 C; 0.2 Si; 0.03 S; 0.02 P.

4.3.1 Material loss measurement on sample 1 and 2

Sample 1 and 2 were investigated in the same group with different treatment. Baseline Barkhausen measurements were made on the as received samples. Material was removed from each disk by surface grinding in increments ranging from around 100 μm

to nearly 300 μm. Sample 1 was then mechanically polished down to 1μm diamond paste after grinding. Sample 2 was left in its "as-ground" state. BE measurements were repeated in order to detect any changes resulting from the removal of material. Vickers microhardness indentation tests were also carried out on the surface of both samples.

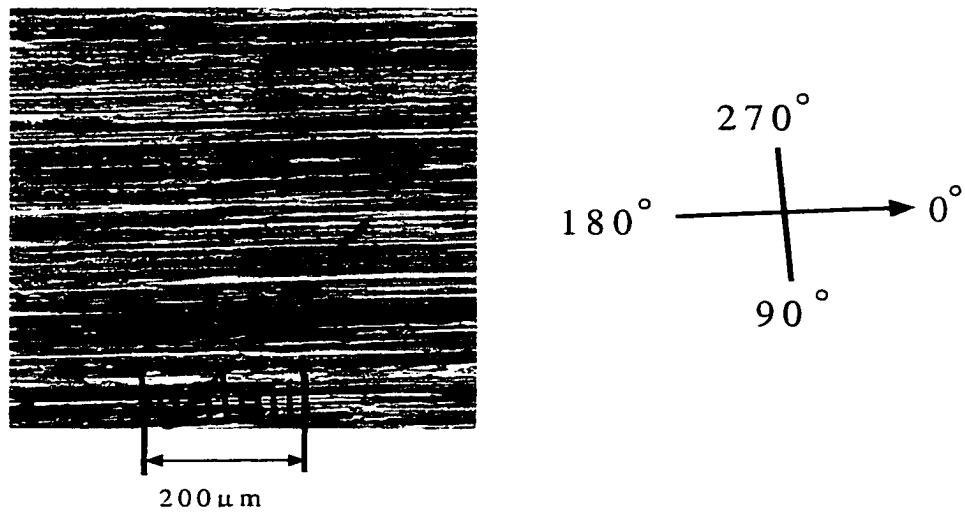

Figure 4-3 The surface of sample 2 after grinding

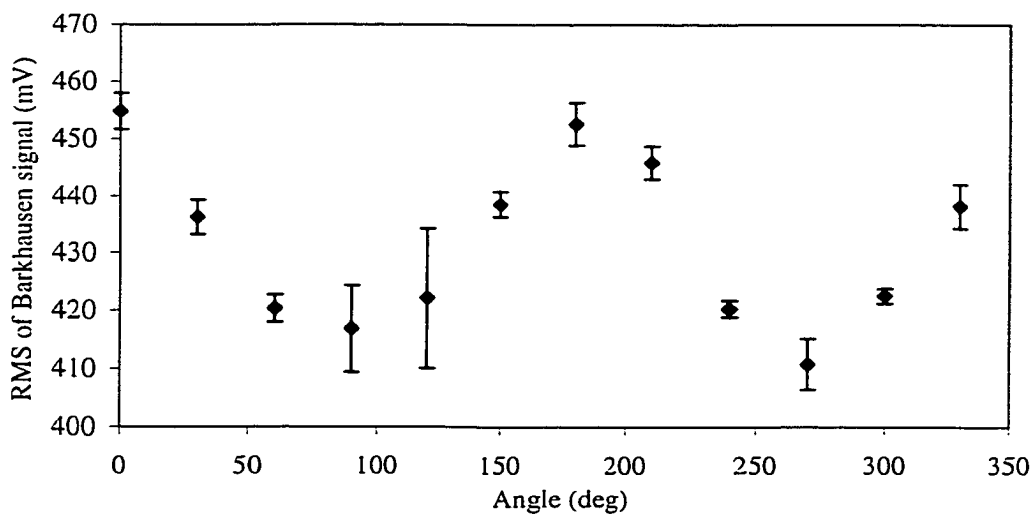

Figure 4-4 Root mean square of Barkhausen signal versus probe angle

The surface of sample 2 was found to be highly anisotropic due to the grinding action as shown in Figure 4-3. The anisotropy had a strong effect on the Barkhausen measurement since the applied field was mostly uniaxial in the plane of the surface. A plot of RMS Barkhausen activity versus the orientation of the probe produced a near sinusoidal response as shown in Figure 4-4. Peaks in the Barkhausen response occurred at probe orientations of 0° and 180° and corresponded to directions parallel to the surface-grinding pattern.

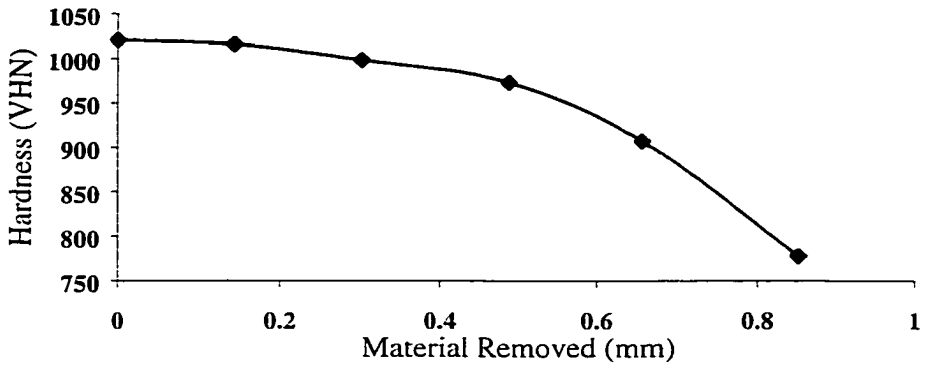

Figure 4-5 Vickers hardness value as a function of the thickness of the material removed from the surface of sample 1

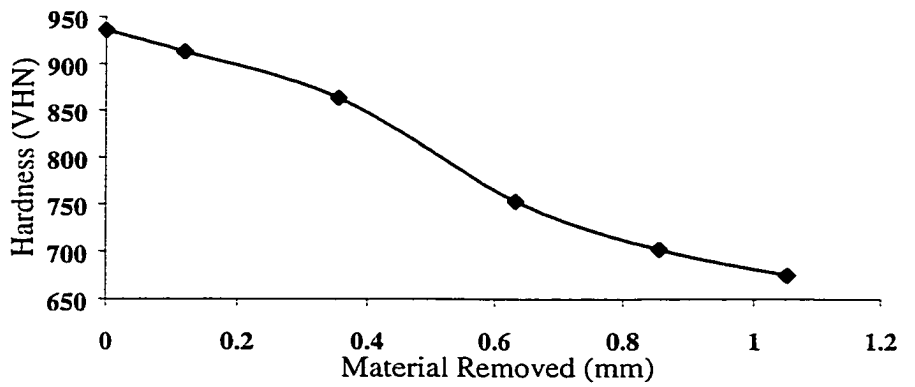

Figure 4-6 Vickers hardness value as a function of the thickness of the material removed from the surface of sample 2

The relationships between the amount of the material removed and the surface hardness are shown in Figure 4-5 and Figure 4-6. The hardness decreases as more material removed due to the decrease in carbon content at the surface.

A similar relationship between BE signal measurement and the amount of material removed was found for both samples, as shown in Figure 4-7 and Figure 4-8. As

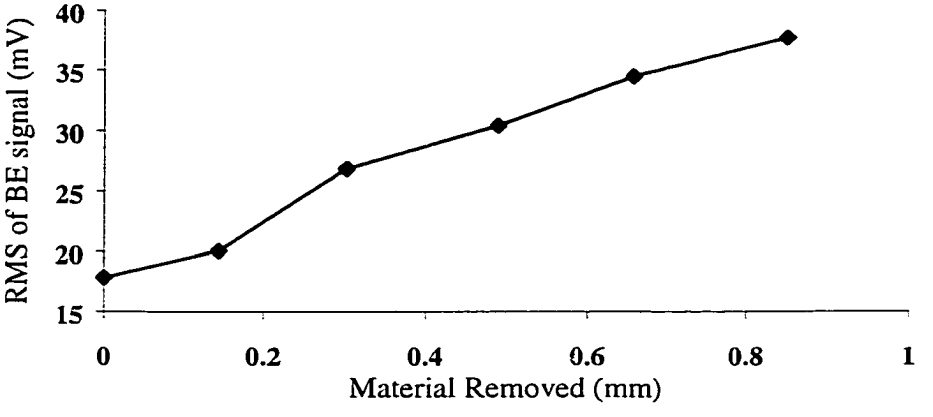

Figure 4-7 RMS of BE signal from sample 1 as a function of the thickness of material removed

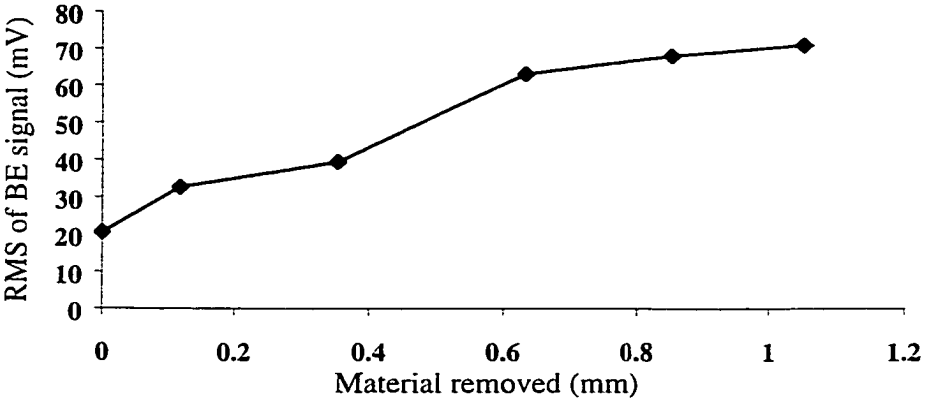

Figure 4-8 RMS of BE signal from sample 2 as a function of the thickness of material removed

material was removed, the layer close to the surface became softer and permeability increased, and therefore the BE signal increased. For sample 1, the removal of 1mm of material (corresponding to the entire case-hardened layer) resulting in a 105% increase in BE signal. For sample 2, BE signal was measured by the probe which oriented parallel to the surface grinding pattern to reduce the influence of anisotropy. The results showed that the removal of 1mm of material (corresponding to 80% of the case-hardened layer) resulted in a 250% increase in BE signal.

4.3.2 Material loss measurement on sample 3

Sample 3 was studied under the similar experimental condition as sample 1. But after grinding and mechanical polishing, sample 3 was also electrical-polished to remove the surface stress. The relationship of the surface hardness and the RMS value of the measured BE signal with the amount of material removed is shown in Figure 4-9.

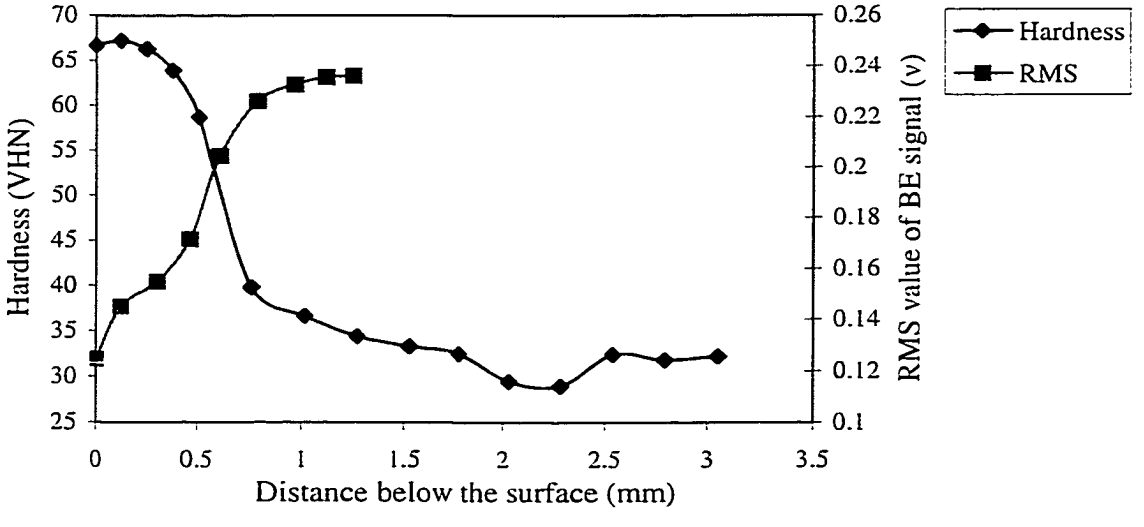

Figure 4-9 Surface hardness and RMS of BE signal from sample 3 as a function of the thickness of material removed

Figure 4-10 shows the surface microstructure of sample 3 at various different depths. The hard surface is characterized by a fine microstructure (acicular martensite) shown in Figure 4-10 (a), (b) and (c). Retained austensite (white region) are also observed in these figures. However the volume fraction of the retained austensite in Figure 4-10 (c) is smaller than that observed in Figure 4-10 (a) and (b), showing a lower carbon content. Figure 4-10 (d), (e) and (f) show a mixture of acicular and lath martensites. The volume fraction of lath martensites (dark regions) is higher for a deeper layer indicating a decrease in carbon content with depth below the case-hardened surface.

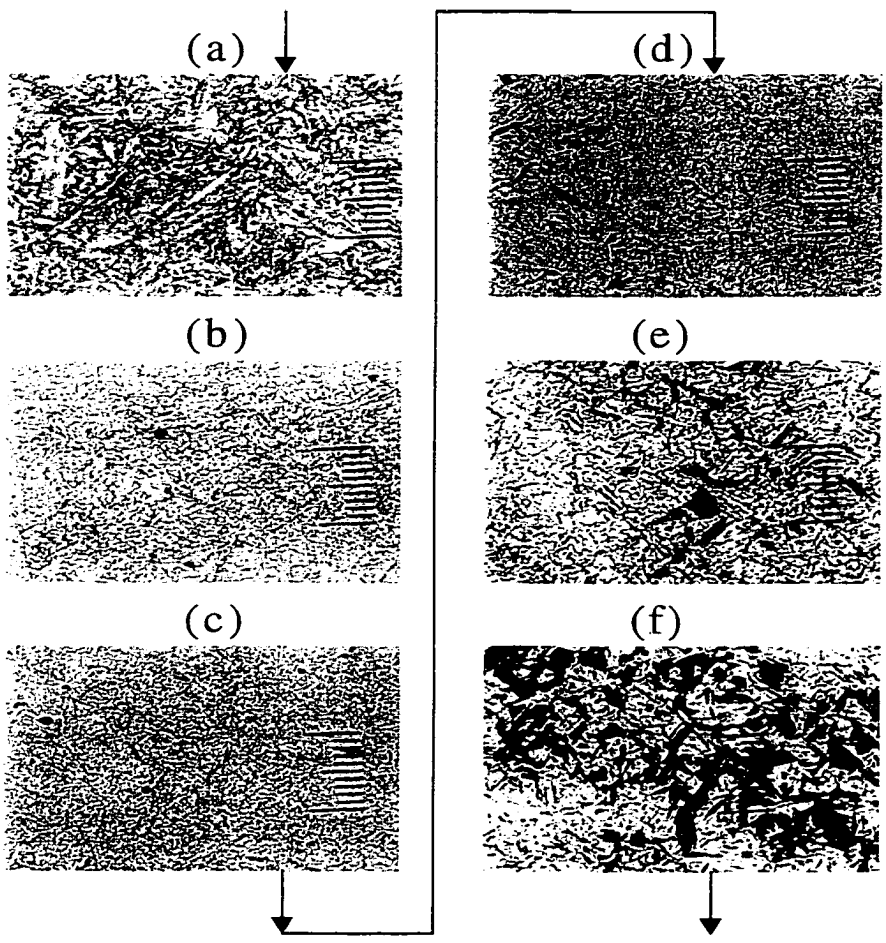

Figure 4-10 Micrographs from sample 3 after successive amounts of material were removed.

4.3.3 Discussion

The measurement results show that BE signals are highly sensitive to surface material loss. As material was removed, the hardness of the region of material from which the BE signal measurements are obtained became lower and its permeability became higher. The domain walls were therefore able to move over larger distances resulting in stronger BE signal. However, it has been shown in Figure 4-9 that in the uncarburized region, the BE signal remained almost constant. These results demonstrate the feasibility of using the BE measurement for monitoring wear-induced material loss.

4.4 Conclusion

The results presented in this chapter show that magnetic Barkhausen signal varies systematically with the amount of the material removed from carefully prepared test samples. This suggests that Barkhausen measurements can be used to monitor the wear-induced material loss in case-hardened steel. Changes in signal levels were large, in some instances these were greater than 100%, which indicates the high sensitivity of Barkhausen emissions to surface condition. This high sensitivity confirms the practical viability of the Barkhausen method even in situations where there is likely to be ambient electromagnetic noise.

It is known that magnetic Barkhausen signal is affected by grain boundaries, carbides, inclusions and dislocations. The individual effects can be distinguished from each other under certain conditions. In the case of carburization, the extensive carbide precipitation due to carbon diffusion dominated the microstructural variation and strongly influenced the hardness. These carbide particles pin the domain walls. When carbon was removed it became easier for domain walls to overcome the pinning sites. The net effect was an increase in the Barkhausen signal with decrease in the carbon content.

Furthermore, it has been shown that in the uncarburized region, the Barkhausen signal remains almost constant.

In practice, grinding damage will often occur in a single direction leading to surface anisotropy. The results here have shown that the detected Barkhausen signal depends on the orientations of the sensor under these conditions. If this direction is known and does not change from location to location on the surface, then the Barkhausen measurement can be reliably applied. Otherwise the presence of surface anisotropy needs to be taken into account in interpreting the measurements.

5 HYSTERESIS EXTENSION TO THE NON-LINEAR MAGNETIC BARKHAUSEN MODEL

5.1 Introduction

Ferromagnetic hysteresis and the Barkhausen effect are mainly related to the irreversible stochastic motion of magnetic domain walls during the magnetization process. The intrinsically random nature of domain wall motion is a consequence of the pinning process caused by lattice defects, inclusions, or interactions between different walls. Magnetic and thermal treatments, applied stresses, and many other factors may affect the properties of the pinning sites. Because of this, a detailed description of the various microscopic magnetization processes, and of the related hysteretic behavior, still remains a very difficult task.

Concurrent research on the description of the underlying processes of the Barkhausen effect such as discontinuous domain wall motion and domain rotations has led to the development of theoretical models by Alessandro *et al.* (ABBM) [7, 8] and by Jiles *et al.* (JSW) [10]. These models allow the various characteristics of the Barkhausen signals to be described mathematically and linked to other properties of a material such as the internal potential experienced by the domain walls, the differential permeability, coercivity and hysteresis loss, and also to externally controlled variables such as rate of change of magnetic field.

A new model incorporating ideas from both of these previous models is proposed in this thesis. The classical Jiles-Atherton hysteresis model [81] was integrated into this new model to calculate the irreversible permeability of the sample. As a result, the new model allows for changes in permeability with applied field and can be used to

investigate the Barkhausen effect signal according to the variations in magnetic properties around the hysteresis loop.

5.2 Jiles-Atherton hysteresis model

Inside a ferromagnetic material, there is coupling between the domains. According to the Jiles-Atherton model this coupling can be represented as a coupling to the bulk magnetization $\boldsymbol{M}$. Therefore, the effective magnetic field which each magnetic domain experiences is

$$\boldsymbol{H}_e = H + \alpha \boldsymbol{M} \quad , \tag{5-1}$$

where α is a mean field parameter representing inter-domain coupling. This effective field is analogous to the Weiss mean field experienced by the individual magnetic moments within a domain, although the mean field parameter α is different in the two cases.

The response of the magnetization to this effective field in the absence of hysteresis can be expressed as

$$M = M_s f(H_e) \quad , \tag{5-2}$$

where f is an single-valued function of H_e which takes the value zero when H_e is zero and takes the value unity as H_e tends to infinity; and M_s is the saturation magnetization. The form of this function varies depending on such factors as anisotropy and texture. This has been discussed in a recent paper [82]. However, this expression ignores the possibility of the change of magnetization being impeded such as when the motion of domain walls is inhibited by pinning sites. Therefore it can only be used to model the magnetization state of a ferromagnetic material at its global equilibrium state. This applies only in the case of an ideal material in which there are no impedances to the changes in magnetization. In

practice it applies to the anhysteretic or ideal magnetization curve which can be created artificially by the application of a decaying AC field superimposed on the DC field as described by Cullity [17]. The anhysteretic curve can then be written as

$$M_{an}(H_e) = M_s f(H_e) \quad , \tag{5-3}$$

where M_{an} is the anhysteretic magnetization. In the original Jiles-Atherton model, a modified Langevin expression [83] was chosen as the arbitrary function $M_s f(H_e)$, which leads to an expression for the anhysteretic magnetization in the case of isotropic materials [84]

$$M_{an}(H_e) = M_s(\coth(H_e / a) - (a / H_e)) \quad , \tag{5-4}$$

Here a is a parameter with the dimension of magnetic field which characterizes the shape of the anhysteretic magnetization and is defined as

$$a = \frac{k_B T}{\mu_0 m} \quad , \tag{5-5}$$

where k_B is Boltzmann's constant, m is the magnetic moment of a pseudo domain and T is the temperature in Kelvin. Although (5-4) is an implicit function, it represents a single-valued relation between magnetic field H and magnetization M_{an} for certain values of α and a. An example is shown in Figure 5-1.

Under the action of a magnetic field, domain walls will move so that the volume of domains aligned favorably with respect to the field direction increases at the expense of the domains aligned unfavorably with respect to the field direction. If a 180° domain wall of area A moves through a distance dx, the change in magnetization due to the movement is

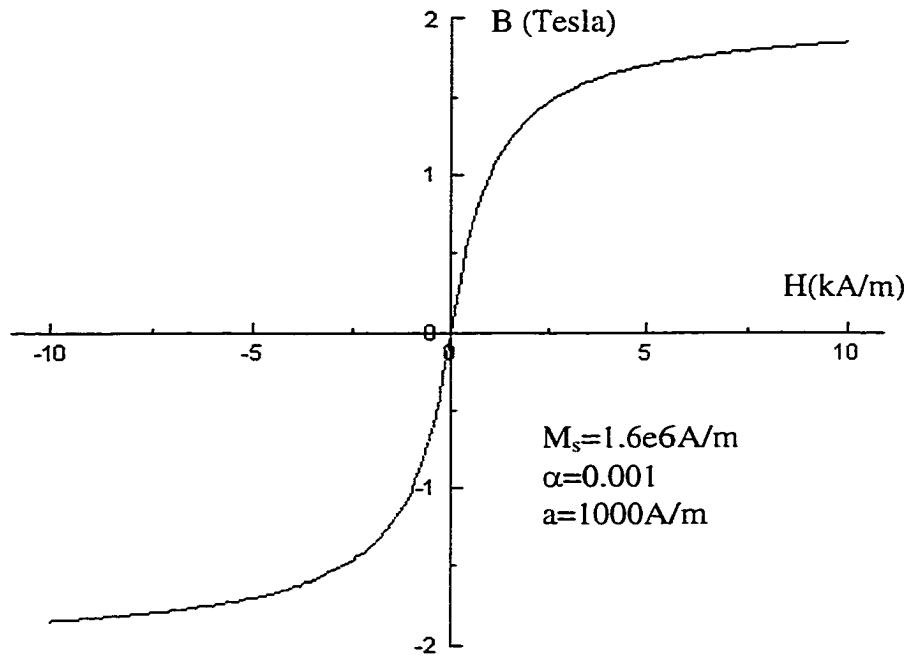

Figure 5-1 Anhysteretic magnetization curve modeled using Langevin function

$$dM = 2M_s A dx \quad , \tag{5-6}$$

where M_s is spontaneous magnetization within a domain.

For non-180° domain walls, the change in magnetization is

$$dM = M_s(1-\cos\theta)A dx \quad , \tag{5-7}$$

where θ is the relative orientation of the magnetization vectors in the domains on either side of the wall.

However the motion of domain walls under the influence of an applied magnetic field is impeded by the presence of pinning sites inside the material, such as grain boundaries, dislocations, inclusions and secondary phases which have magnetic properties different from that of the matrix. These defects induce local energy minima

when domain walls intersect them. Extra energy is needed for domain walls to overcome the local energy minima, resulting in hysteresis loss. Consider a pinning site on a domain wall between domains with magnetization $\boldsymbol{m}$ and $\boldsymbol{m}'$ where $\boldsymbol{m}$ is aligned parallel to the applied field and is the growing domain while $\boldsymbol{m}'$ is aligned at some arbitrary angle θ to the field. The energy required to overcome the pinning site depends on two factors, namely the nature of the pinning site and the relative orientations of the magnetizations in the domains on either side of the wall. The model assumes that the distribution of pinning sites inside the material is homogeneous with pinning site density n and that every pinning site has the same average pinning energy. The total energy dissipated through pinning when a 180° domain wall of area A moved through a distance dx is given by

$$E_{pin} = n\mu_0 \langle \varepsilon_\pi \rangle A dx \quad , \tag{5-8}$$

where $\langle \varepsilon_\pi \rangle$ is the average pinning energy for 180° walls. For non-180° domain wall, the pinning energy is

$$E_{pin} = \frac{1}{2} n\mu_0 \langle \varepsilon_\pi \rangle (1-\cos\theta) A dx \quad . \tag{5-9}$$

Therefore

$$E_{pin} = \frac{\mu_0 n \langle \varepsilon_\pi \rangle dM}{2M_s} \quad , \tag{5-10}$$

replacing $k = n\langle \varepsilon_\pi \rangle / 2M_s$ gives

$$E_{pin} = \mu_0 k dM \quad . \tag{5-11}$$

Hence under the assumption of a uniform distribution of pinning sites, and treating each one as having the average pinning energy, the total work against pinning is proportional

to the change in magnetization.

In the absence of pinning sites, all energy supplied to the material is translated into a change in magnetostatic energy in the material and this is the anhysteretic magnetization. In the case of hysteresis, the energy supplied to the materials equals the change in magnetostatic energy plus hysteresis loss. Therefore, the magnetostatic energy in the material is the energy difference between input energy, which is equal to the anhysteretic energy without pinning, minus the energy loss due to the domain wall pinning [81].

$$\mu_0 \int M(H_e) dH_e = \mu_0 \int M_{an}(H_e) dH_e - \mu_0 \int k\left(\frac{dM}{dH_e}\right) dH_e \quad , \tag{5-12}$$

where $\boldsymbol{H_e}$ is the effective field give by (5-1). Differentiating this equation gives

$$M(H_e) = M_{an}(H_e) - k\left(\frac{dM}{dH_e}\right) \quad . \tag{5-13}$$

Rearranging the above equation yields the form for susceptibility

$$\frac{dM}{dH_e} = \frac{M_{an}(H_e) - M(H_e)}{k} \quad . \tag{5-14}$$

Replacing H_e with $H + \alpha M$ gives

$$\frac{dM}{dH} = \frac{M_{an} - M}{\delta k - \alpha(M_{an} - M)} \quad , \tag{5-15}$$

where the parameter δ takes the value +1 when H increases in the positive direction, *i.e.* $dH/dt > 0$, and -1 when H increases in the negative direction, *i.e.* $dH/dt < 0$. This choice of sign convention ensures that the pinning always opposes change in magnetization. The above equation shows that apart from the perturbation due to the

coupling of magnetization, expressed through the coefficient α, the rate of change of magnetization M with field is proportional to the displacement from the anhysteretic $M_{an} - M$.

The magnetization M can be calculated as the sum of two components, an irreversible component M_{irr} and a reversible component M_{rev}:

$$M = M_{irr} + M_{rev} \quad . \tag{5-16}$$

The irreversible component of magnetization is given by the solution of (5-15)

$$\frac{dM_{irr}}{dH} = \frac{M_{an} - M_{irr}}{\delta k - \alpha(M_{an} - M_{irr})} \quad . \tag{5-17}$$

The reversible component of magnetization due to reversible domain wall bowing, reversible translation and reversible rotation was expressed in the model as

$$M_{rev} = c(M_{an} - M_{irr}) \quad , \tag{5-18}$$

where the constant c ranges from 0 (completely irreversible magnetization) to 1 (completely reversible magnetization). The differentiation of above equation gives the rate of changes of the reversible component

$$\frac{dM_{rev}}{dH} = c(\frac{dM_{an}}{dH} - \frac{dM_{irr}}{dH}) \quad . \tag{5-19}$$

The Jiles-Atherton model which includes both irreversible and reversible magnetization can be expressed as

$$\frac{dM}{dH} = (1-c)\frac{M_{an} - M}{\delta k - \alpha(M_{an} - M)} + c\frac{dM_{an}}{dM} \quad . \tag{5-20}$$

After solving the first order differential equation numerically, a sigmoid-shaped

hysteresis loop can be obtained. Through changing the parameters, this model is able to describe the magnetization curves of soft magnetic materials, hard magnetic materials and anhysteretic magnetization. Figure 5-2 shows three typical modeled hysteresis curves.

5.3 Review of current Barkhausen models

5.3.1 ABBM model

A description of domain wall dynamics giving rise to the Barkhausen effect has been proposed by Alessandro, Beatrice, Bertotti and Montorsi [7]. They considered the

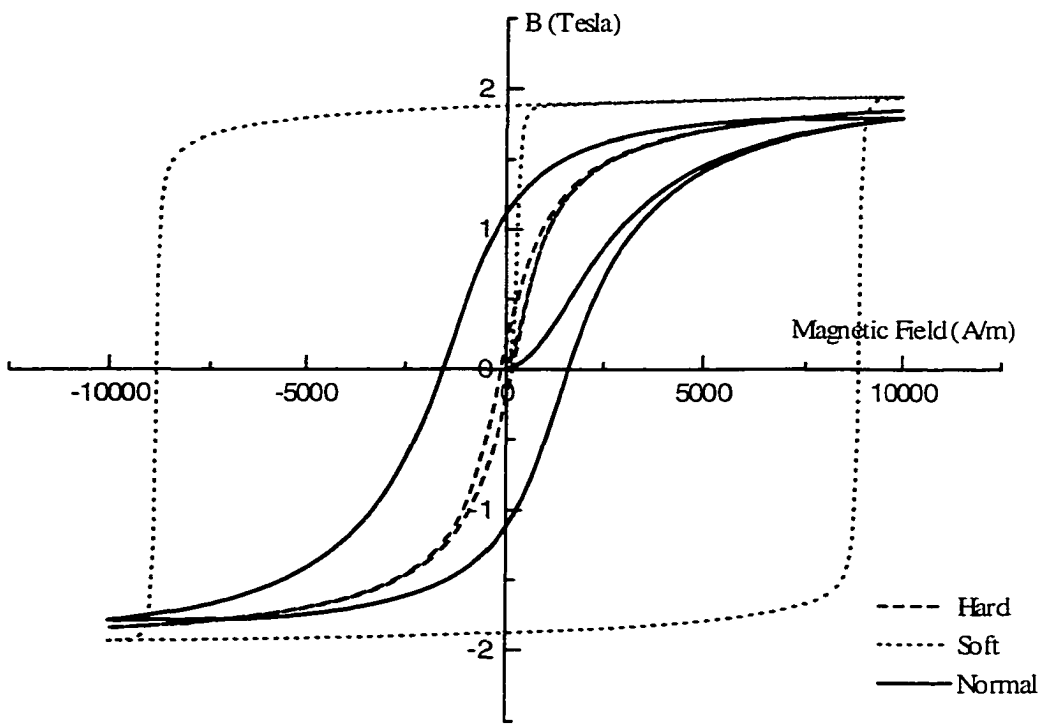

Figure 5-2 Calculated hysteresis curves using the Jiles-Atherton model

problem of a single domain wall moving in a randomly perturbed medium in terms of a stationary Markov process. The theory began with the dependence of domain wall velocity on applied field and internal local coercivity field, as was reported by Williams, Shockley and Kittel [25]:

$$v = k(H - H_c) \quad , \tag{5-21}$$

where H_c is the local coercive field experienced by the moving domain wall, and the constant k can be calculated from Maxwell's equations. As the domain wall moves through a material it will experience an effective pinning field H_c which is a randomly fluctuating function of domain wall position and can be approximated by a Wiener-Levy (WL) process [9]. However, when large domain wall displacements are considered, the presence of a finite correlation length ξ is inevitably expected. ξ corresponds to the finite interaction range of the domain wall with a given perturbation. A convenient description of these features is obtained by assuming that H_c obeys the Langevin equation [9]:

$$\frac{dH_c}{d\phi} + \frac{H_c - < H_c >}{\xi} = \frac{dW}{d\phi} \quad , \tag{5-22}$$

where the WL process $W(\phi)$ is characterized by

$$< dW >= 0, \ \left\langle |dW|^2 \right\rangle = 2Ad\phi \quad , \tag{5-23}$$

with A being a constant which describes the variance of the fluctuations in the WL process $W(\phi)$.

By considering a planar 180° domain wall moving in a specimen of unit volume with thickness d and cross sectional area S, as shown in Figure 5-3. The rate of change of

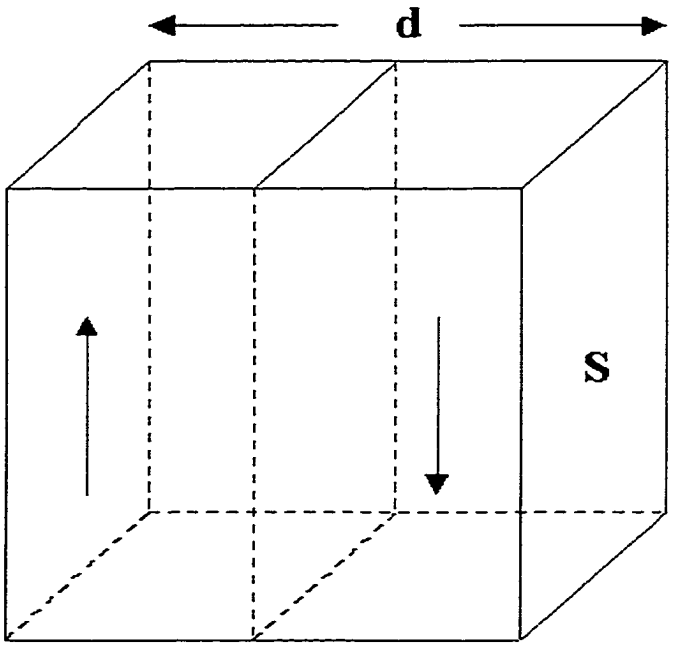

Figure 5-3 A 180° domain wall moving across a slab of material

magnetization in the slab is therefore [78]

$$\frac{dM}{dt} = 2M_s \frac{dx}{dt}\frac{1}{d} \quad , \tag{5-24}$$

and so in the case of a high permeability material for which $B \approx M$, the rate of change of the magnetic flux is

$$\frac{d\phi}{dt} = \mu_0 S \frac{dM}{dt} = \frac{2\mu_0 S M_s}{d}\frac{dx}{dt} = \frac{2\mu_0 S M_s}{d} v \quad . \tag{5-25}$$

Rewriting (5-21) as

$$v = k(H - H_c) = \frac{d}{2\mu_0 S M_s}\frac{d\phi}{dt} \quad , \tag{5-26}$$

and considering the energy dissipated as heat by eddy currents when power is supplied by

the external field [85], the velocity is inversely proportional to the conductivity σ, so that

$$\frac{d\phi}{dt} = \frac{1}{\sigma G}(H - H_c) \quad , \tag{5-27}$$

where the dimensionless coefficient $G = (4/\pi^3) = \sum_{odd}(1/k^3) = 0.1356$, if a wide slab $(S >> d^2)$ is considered.

The time derivative of above equation can then be written as

$$\frac{d\dot{\phi}}{dt} + \frac{\dot{\phi} - S\dot{I}}{\tau} = -\frac{1}{\sigma G}\frac{dH_c}{dt} \quad , \tag{5-28}$$

where I is the intensity of magnetization and is defined by $I = \mu_0 M$,the time constant τ is defined as

$$\tau = \sigma G S \mu \quad . \tag{5-29}$$

However, all the variables in (5-28) are based on the local condition and can be changed dynamically with the domain wall position. To arrive at a Langevin equation which couples the rate of change of flux with the local coercive field, the ABBM model assumes that the permeability μ_r is very large compared with unity $(\mu_r >> 1)$, so the differential susceptibility χ' and differential permeability μ_r' will be approximately equal, *i.e.* $\mu_r' \approx \chi'$. Using a linear approximation for the rate of change of magnetization with field, the rate of change of magnetic field with respect to time becomes

$$\frac{dH}{dt} = \frac{dH}{dM}\frac{dM}{dt} \approx \frac{1}{\mu_r'}\frac{dM}{dt} \quad , \tag{5-30}$$

and since $\mu_r >> 1$, then $M >> H$ and $M \approx \frac{B}{\mu_0} = \frac{\phi}{\mu_0 S}$, then

$$\frac{dM}{dt} \approx \frac{1}{\mu_0 s}\frac{d\phi}{dt} \quad , \tag{5-31}$$

and so

$$\frac{dH}{dt} \approx \frac{1}{\mu_0 \dot{\mu_r} S}\frac{d\phi}{dt} \quad . \tag{5-32}$$

In real materials, $H = H_a - H_m$, where a and m designate the applied and magnetostatic fields respectively. Under the limited assumptions that the measured differential permeability $\dot{\mu}_{rmeas}$ remains constant (*i.e.* the magnetization curve on the *M,H* plane remains a straight line) $\dot{\mu}_{rmeas} = \frac{1}{\mu_0}\frac{dB}{dH_a} \approx \frac{dM}{dH_a} = const$ and the average magnetization increases at a constant rate (*i.e.* $\frac{dM}{dt} = const$), $\frac{dH_a}{dt} = \frac{1}{\dot{\mu}_{rmeas}}\frac{dM}{dt}$. Under these conditions, $\frac{d\phi}{dt}$ is a stationary process with a mean value over the range of fields of interest given by

$$\left\langle \frac{d\phi}{dt} \right\rangle = S\mu_0 \frac{dM}{dt} \quad . \tag{5-33}$$

Taking the time derivative of the of (5-27) and replacing $H = H_a - H_m$ gives

$$\frac{d\dot{\phi}}{dt} = \frac{1}{\sigma G}\frac{dH_a}{dt} - \frac{1}{\sigma G}\frac{dH_m}{dt} - \frac{1}{\sigma G}\frac{dH_c}{dt} \quad . \tag{5-34}$$

By assuming that $\frac{dH_m}{dt} = \left\langle \frac{dH_m}{dt} \right\rangle = \frac{1}{\dot{\mu}_{rmeas}\mu_0 S}\frac{d\phi}{dt}$, the above equation can be rewritten as

$$\frac{d\dot{\phi}}{dt} = \frac{1}{\sigma G}\left(\frac{1}{\dot{\mu}_{rmeas}}\frac{dM}{dt} - \frac{1}{\dot{\mu}_{rmeas}\mu_0 S}\frac{d\phi}{dt}\right) - \frac{1}{\sigma G}\frac{dH_c}{dt} \quad . \tag{5-35}$$

By replacing $\tau = \sigma G \dot{\mu}_{rmeas} \mu_0 S$, the same equation as (5-28) can be arrived at.

However, it is important to note that this linear approximation only applies under extremely limited cases which are restricted to modeling the Barkhausen signal at constant applied field rates and in a small region of the hysteresis loop near the coercive point where the permeability is approximately constant. It should be also remembered that the model is restricted to soft magnetic materials where $\mu / \mu_0 >> 1$.

Equation (5-28) also has the form of the Langevin equation, but the random term dH_c / dt does not correspond to a Gaussian white noise, and must be evaluated from (5-22). Solutions of this equation under the linear approximation have been provided by Alessandro *et al.*[7] and compared with experimental measurements along limited regions of the magnetization curve close to the coercivity where this linear approximation is more or less satisfied.

An interesting result is that although the model is derived only for the case of a single domain wall moving in a randomly perturbed medium, it can also accurately describe experimental Barkhausen signals originating from a combination of many interacting domain walls [8].

5.3.2 JSW model

A generalized model which is able to describe the Barkhausen effect over the entire hysteresis loop has been proposed by Jiles, Sipahi and Williams [10]. The first assumption of this model is that the level of Barkhausen activity in a given time is proportional to the rate of irreversible change in magnetization,

$$\frac{dM_{JS}}{dt} \propto \dot{M}_{irr} = \dot{\chi}_{irr} \dot{H} \quad , \tag{5-36}$$

where $\dot{\chi}_{irr}$ is the irreversible differential susceptibility. M_{JS} represents the Barkhausen activity in terms of the "jump sum" as discussed by Swartzendruber *et al.*[86] and is basically of the product of number of events N and the average Barkhausen jump size $< M_{disc} >$ over a given time interval:

$$M_{JS} = N < M_{disc} > \quad . \tag{5-37}$$

While not explicitly stated, this implies that the Barkhausen signal is the result of a linear combination of many individual events occurring at different locations within the material. In order to account for the random nature of the Barkhausen effect, the number of Barkhausen events in a given time period $N(t_n)$ are assumed to be related to the number of events in the previous time period $N(t_{n-1})$ by some random increment. This increment is small enough to ensure that the number of events remain correlated with those in the previous time period. The number of Barkhausen events per unit change of M in a given time period t_n $N'(t_n) = dN(t_n)/dM$ can be described by an equation of the form

$$N'(t_n) = N'(t_{n-1}) + \Delta N'(t_{n-1}) \quad . \tag{5-38}$$

Since the number of possible locations for a Barkhausen event to occur in the material is large, but the probability that an event occurs at a specific point and time in the material is low, the Poisson distribution should describe the variation of the number of events from one time period to the next. This uncertainty can be incorporated into the statistics using the relation

$$\Delta N^{\cdot}(t_{n-1}) = \delta_{rand}\sqrt{N^{\cdot}(t_{n-1})} \quad , \tag{5-39}$$

where δ_{rand} is a random number in the range $-1.47 \le \delta_{rand} \le +1.47$.

The Barkhausen jump sum in the interval between t_{n-1} and t_n will be the sum of all discontinuous changes in magnetization in that time interval, which on average will be

$$M_{JS}(t_n) = N(t_n) < M_{disc} > = < M_{disc} > \int_{t_{n-1}}^{t_n} dN(t) \quad . \tag{5-40}$$

Thus

$$M_{JS}(t_n) = < M_{disc} > \int_{t_{n-1}}^{t_n} (\frac{dN}{dM})\chi_{irr}^{\cdot}\, \dot{H}\, dt \quad . \tag{5-41}$$

By differentiating this equation, a model of the form

$$\dot{M}_{JS}(t_n) = < M_{disc} > \chi_{irr}^{\cdot}\, \dot{H}\left[N^{\cdot}(t_{n-1}) + \delta_{rand}\sqrt{N^{\cdot}(t_{n-1})}\right] \quad , \tag{5-42}$$

can be arrived at. This is the key equation in this model. It allows the number of Barkhausen events in time period t_n to be related to the number of events in time period t_{n-1} by a random increment $\Delta N(t_{n-1})$, which is small enough to ensure that $N(t_n)$ is correlated with $N(t_{n-1})$. The equation can also take into account changes in differential susceptibility and in the rate of change of magnetic field.

The advantage of this model is that it is able to describe the Barkhausen effect at all points on the hysteresis curve and under the action of variable rate of change of applied field, and thus does not require the assumption of a stationary process used by the ABBM model. The value of $\chi_{irr}^{\cdot}$ can be determined from hysteresis models and thus the effects of stress on the Barkhausen effect can be accurately predicted by incorporating the dependence of the differential susceptibility on stress into this model. While the

simplicity of the model is attractive, no attempt has been made to try to model the frequency response of the Barkhausen signal.

If we consider the ABBM model in the case where $\xi \to \infty$ (which corresponds to an infinite correlation distance between the domain wall and a given perturbation in the material or a sufficiently low domain wall velocity), (5-22) reduces to $dH_c = dW$, which can also be express as: $dH_c = \delta\sqrt{2Ad\phi}$, where δ is normally distributed with a mean of zero and a variance of 1. If we substitute this into (5-28) and rearrange, we obtain

$$\sigma G\, d\dot{\phi}/dt = \dot{H}_a - \dot{H}_m - \delta\sqrt{2Ad\phi}/dt \quad . \tag{5-43}$$

Over short time periods, the equation will be dominated by the third term on the right, and thus if we consider the change in $\dot{\phi}$ during a short time increment Δt, we find

$$\Delta\dot{\phi} = \delta\sqrt{2A\dot{\phi}\Delta t}/\sigma G \quad , \tag{5-44}$$

which leads to a simplified ABBM model of the form

$$\dot{\phi}(t_n) = \dot{\phi}(t_{n-1}) + \delta\frac{\sqrt{2At}}{\sigma G}\sqrt{\dot{\phi}(t_{n-1})} \quad . \tag{5-45}$$

The model described by (5-42) can be rewritten as

$$\dot{M}_{JS}(t_n) = \dot{M}_{JS}(t_{n-1}) + \delta\sqrt{\langle M_{disc}\rangle \chi_{irr}\, \dot{H}}\sqrt{\dot{M}_{JS}(t_{n-1})} \quad , \tag{5-46}$$

which demonstrates that the ABBM model reduces to a mathematical structure similar to JSW model over short time periods and under the given restrictions. Therefore the ABBM and JSW models give identical results under certain limiting conditions.

5.4 Main contribution: Hysteresis extension to the non-linear magnetic Barkhausen model

5.4.1 Theoretical improvements

5.4.1.1 Irreversible Magnetization change and Barkhausen effect

In the ABBM model, soft materials are considered so that $\mu/\mu_0 >> 1$ and $B \approx I$ ($I = \mu_0 M$). In this limiting case, the Barkhausen effect can be related to the rate of change of magnetic flux. However, this relation will not always hold since Barkhausen jumps correspond to irreversible movements of the domain wall and thus can only occur when there are irreversible changes in I. Therefore, the changes of B that do not originate from irreversible discontinuous changes in I will not contribute to the Barkhausen effect. If we inspect the Barkhausen signal obtained over a hysteresis loop, there is a region where essentially no Barkhausen events occur. In Figure 5-4, an experimental Barkhausen signal as well as the voltage signal V across the pickup coil due to changes in the induction have been plotted. There is a reasonable fit between these two curves in the region near the maximum in the Barkhausen envelope. However, in the other regions, the Barkhausen signal is much smaller than what would be predicted if it were proportional to the induced voltage across the pickup coil. If we look at the corresponding values of I and H in this region, we see that the value of H is decreasing from its maximum value to zero, and thus the value of I is decreasing from its maximum value to remanence.

The magnetization increases to the tip of the hysteresis loop as the result of domain walls undergoing both reversible and irreversible changes. As the magnetic field is reduced from its peak value to zero, the reversible changes will be undone but the irreversible changes will not, and thus the difference between magnetization at the loop

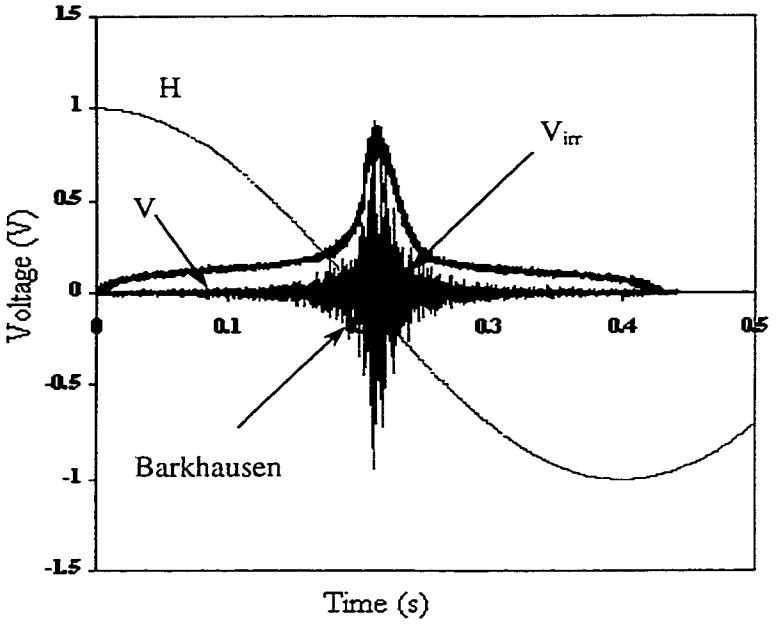

Figure 5-4 Barkhausen signal, voltage V due to total change in magnetization and V_{irr} due to the irreversible change in magnetization.

tip and at remanence represents reversible change in I. The difference in magnetization between remanence and zero represents mostly irreversible changes in I that had taken place. Since the change in I as the magnetic field is removed corresponds primarily to reversible changes in I, it follows that there will be fewer Barkhausen jumps in the region where I is decreasing to remanence from saturation value. In Figure 5-4, V_{irr} represents the voltage corresponding to the irreversible changes in magnetization, and it gives a much better fit to the Barkhausen envelope than the voltage V representing the total change in magnetization.

5.4.1.2 Model Implementation

Since Barkhausen jumps actually correspond to irreversible changes in magnetization rather than changes in magnetic induction as discussed above, the model

should be written in terms of SI_{irr} rather than ϕ

$$\frac{d\dot{I}_{irr}}{dt} = \frac{\dot{\chi}_{irr}}{\tau}\left(\frac{dH_a}{dt} - \frac{dH_c}{dt}\right) - \frac{\dot{I}_{irr}}{\tau} \quad , \tag{5-47}$$

where $\tau = \sigma GS\dot{\chi}_{irr}$, $\dot{\chi}_{irr}$ is the irreversible part of the differential susceptibility. Owing to the non-linear, multi-valued properties of the differential susceptibility, τ is now a function of the position on the hysteresis curve.

The coercive field H_c is described by

$$\frac{dH_c}{dI_{irr}} + \frac{S(H_c - < H_c >)}{\xi} = \frac{dW}{dI_{irr}} \quad , \tag{5-48}$$

where the WL process $W(I_{irr})$ is characterized by

$$< dW >= 0, \; < |dW|^2 >= 2ASdI_{irr} \quad . \tag{5-49}$$

Computer simulations have been carried out using an algorithm similar to the one described by Alessandro *et al.* [7]. If we consider a sufficiently small time period Δt, the change in $\dot{I}_{irr}(t)$ can be described by:

$$\Delta\dot{I}_{irr} = \dot{H}_a \Delta t / \sigma GS - \Delta H_c / \sigma GS - \Delta I_{irr} / \tau \quad , \tag{5-50}$$

where H_c is calculated from

$$\Delta H_c = -(H_c - < H_c >) S\Delta I_{irr} / \xi + \Delta W \quad . \tag{5-51}$$

where ΔW is the variation of the WL process $W(I_{irr})$ in the step ΔI_{irr}. The variations ΔI_{irr} and Δt are not independent, because they must be consistent with $\Delta I_{irr} / \Delta t = \dot{I}_{irr}$. Furthermore, they must be such that $\Delta t / \tau << 1$ and $S\Delta I_{irr} / \xi << 1$.

Unlike the ABBM model, the values of $\dot{\chi}_{irr}$ and $\dot{H}_a$ are functions of time and are determined from the applied field waveform and the hysteresis curve respectively. The dependence of $\dot{\chi}_{irr}$ on H can easily be obtained from the Jiles-Atherton hysteresis model, and then the values of $\dot{\chi}_{irr}$ are integrated into the model to calculate the rate of irreversible change in magnetization $\dot{I}_{irr}(t)$ which is proportional to the Barkhausen voltage according to the JSW model. Once simulation of the voltage corresponding to $\dot{I}_{irr}(t)$ for a specified range of t has been completed, the data is digitally filtered so that it can be directly compared with the experimental data which has undergone a similar filtering process. The Butterworth (7 poles) and elliptical (7 poles, 6 zeros) filters with different cutoff frequencies used in the experiments has been simulated using the algorithm provided in [87].

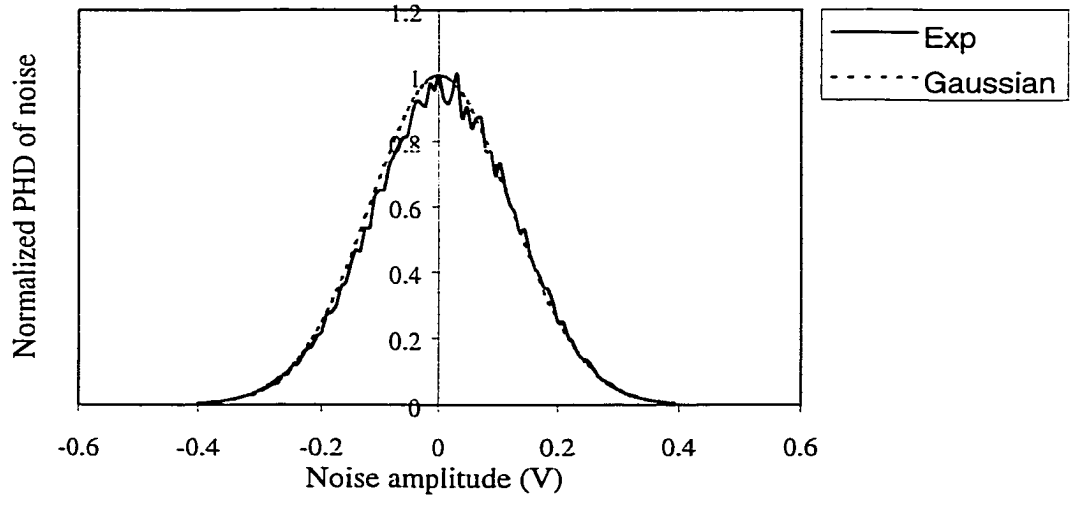

Figure 5-5 Comparison of the PHD result of the background noise and Gaussian distribution

In the real application, it is not possible to totally remove the background noise. Therefore, this factor has to be taken into account in the new model. In order to analyze its statistical characteristic, the background noise was collected and its pulse height distribution (PHD) was calculated using our new data acquisition and analysis system [88]. It has been observed that the PHD result of the background noise obeys the Gaussian distribution as shown in Figure 5-5.

In addition to comparing the modeled Barkhausen waveform with the experimental data, the root mean square (RMS), pulse height distribution (PHD) and fast Fourier transform (FFT) algorithms have also been integrated into the software package to determine whether or not the results of the model accurately describe the experimental data. Figure 5-6 shows the interface of the modeling software package. The model parameters are listed on the right side and the various functions of the package are controlled by the buttons array located at the bottom of the screen.

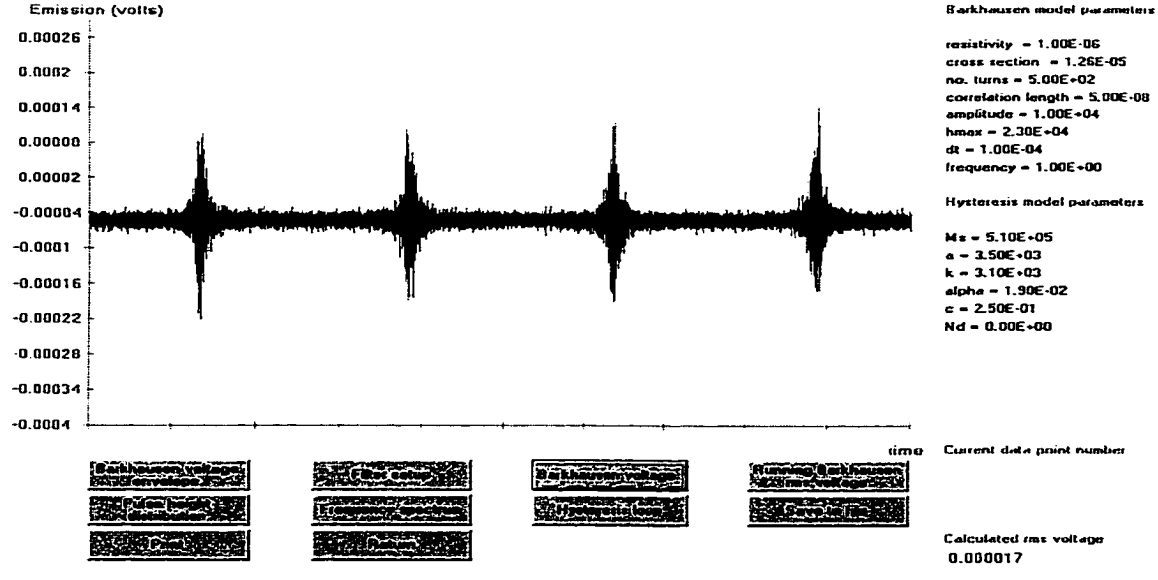

Figure 5-6 Interface of the modeling software package

5.4.2 Measurements of the hysteresis loop and BE signals

The sample used in this study was a nickel rod with diameter 6.35 mm. The experimental setup for measurements of hysteresis loop and BE signals are shown in Figure 5-7. A pickup coil of 800 turns was directly wound around the center of the sample. A Hall sensor was mounted on the sample to detect the surface field along the axis of the sample. The Hall sensor was connected to a gaussmeter and the output was logged on a computer. During the measurements a 2 Hz magnetizing field with a triangular waveform was applied to the sample. The voltage signal induced across the pickup coil, which by Faraday's law is proportional to the dB/dt, was logged on a computer. This signal was integrated numerically with respective to time to obtain the flux density $\boldsymbol{B}$ which was plotted versus the measured field $\boldsymbol{H}$ to give the hysteresis loop. The pickup coil signal was also filtered using an analog band-pass filter and was

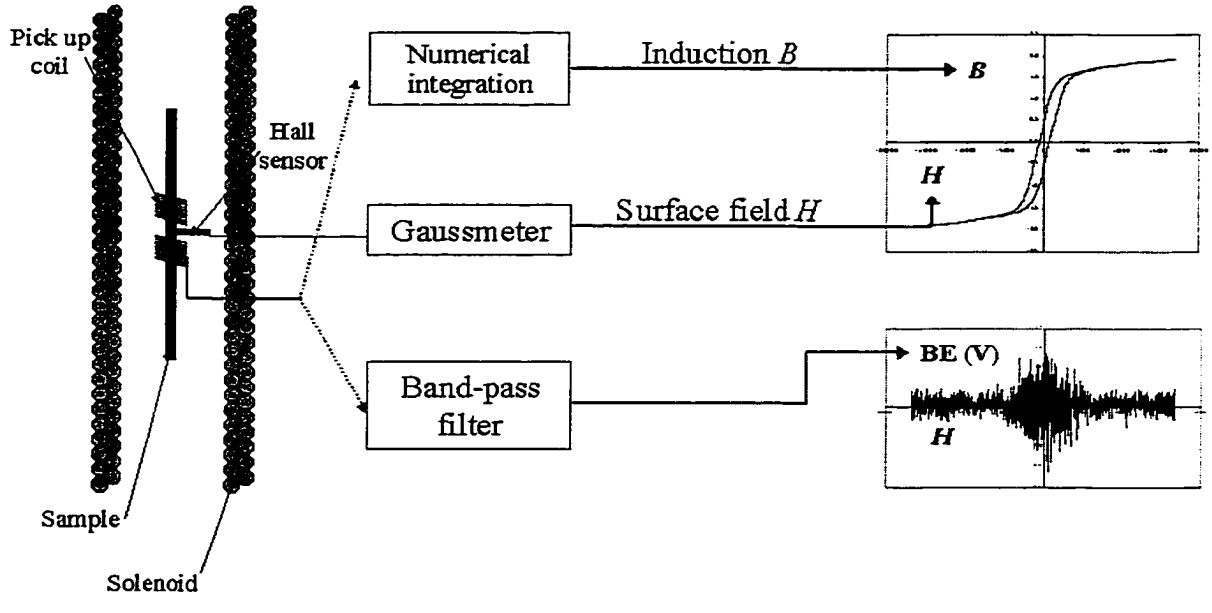

Figure 5-7 Diagram for measuring the BE signals and hysteresis loop

amplified to obtain the BE voltage signal. The BE signal was then acquired at a sampling rate of 10kHz or 500kHz respectively. The sampled signal was analyzed using a recently upgraded measurement system [88] to obtain the root-mean-square (RMS) value, pulse height distribution (PHD), fast Fourier transform (FFT) and power spectral density (PSD) of the voltage signal.

5.4.3 Modeling results

In the simulation, the five parameters in Jiles-Atherton hystereis model, M_s, a, α, c, k, were first obtained from the experimental major hysteresis loop [89] and then the irreversible permeabilities were calculated from the modeled hysteresis loop. Figure 5-8 shows the diagram of the experimental and the calculated hysteresis loops together with the values of the five model parameters.

After the irreversible permeabilities had been obtained, other parameters (σ, S, ξ, A, G) introduced in section 5.4.1.2 were added to the Barkhausen model to simulate the

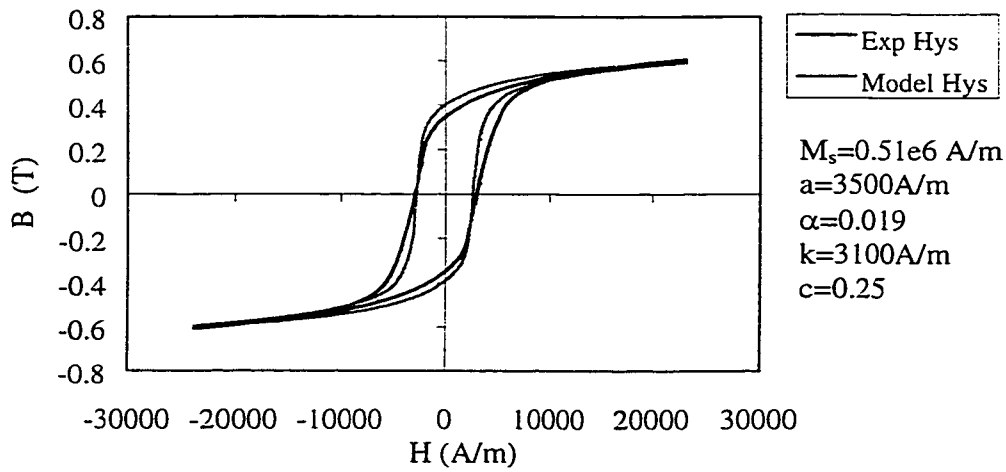

Figure 5-8 Diagram of the experimental and modeling hysteresis loops

BE signal. These parameters were set up to σ=1e6$\Omega^{-1}m^{-1}$, S=3.167e-5m^2, ξ=5e-8Wb, A=1e4, G=0.125 respectively in the simulation. Figure 5-9 and Figure 5-10 show the normalized experimental and modeling BE voltage signals when the sampling rate was 10kHz and the cutoff frequencies of the band-pass filter were 1kHz and 5kHz respectively. The results demonstrate that the new Barkhausen model is able to generate BE signals which closely resemble the experimental data.

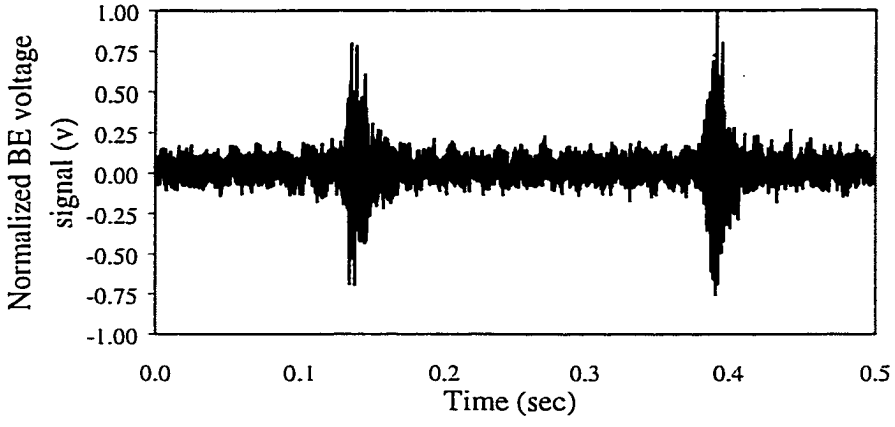

Figure 5-9 Normalized experimental BE voltage signal

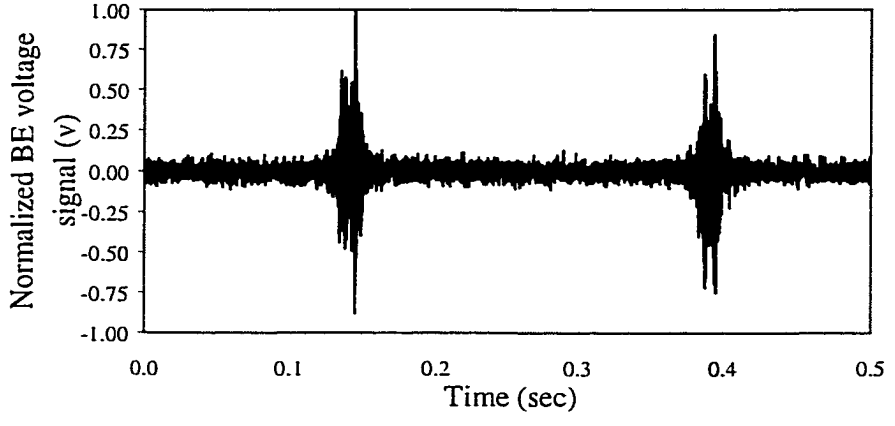

Figure 5-10 Normalized modeling BE voltage signal

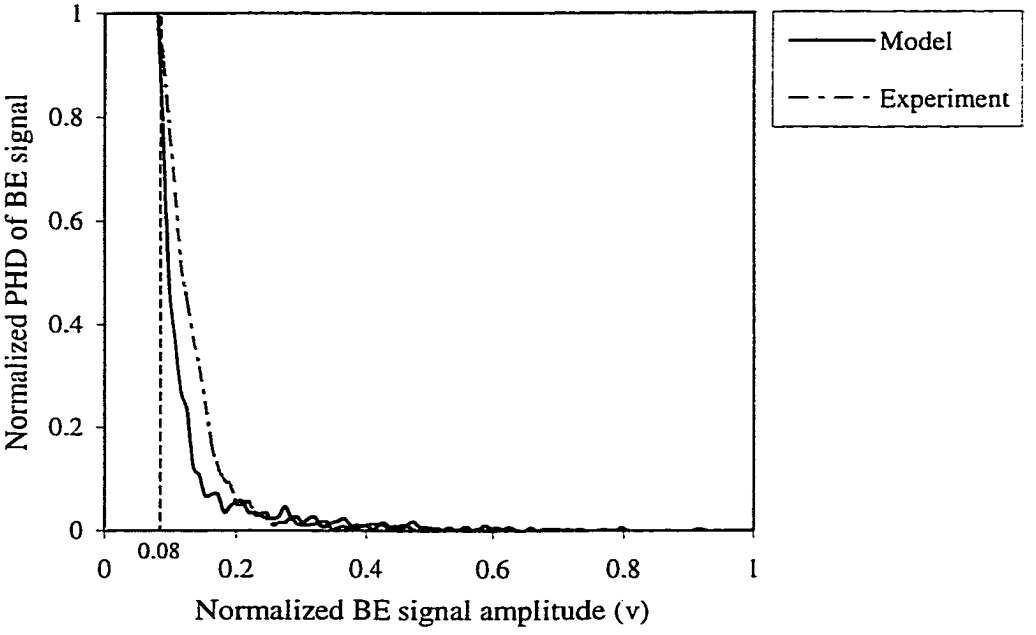

Figure 5-11 Normalized PHD results of BE signal

In order to determine whether or not the results of the model accurately describe the experimental data, the PHD results were obtained from the experiment and model respectively. It has been observed that when the influence of the background noise was removed by setting up the threshold value to the maximal amplitude of the background noise (which equals to approximately 8% of the BE peak signal), the normalized experimental and modeling BE voltage signals show the similar PHD results as indicated in Figure 5-11.

In order to investigate how the BE signals change with the amplitude of the magnetic field, five minor loops and corresponding BE signals were measured and modeled using the same parameters as before. The experimental and modeling results of the hysteresis loops are shown in Figure 5-12 and Figure 5-13 respectively.

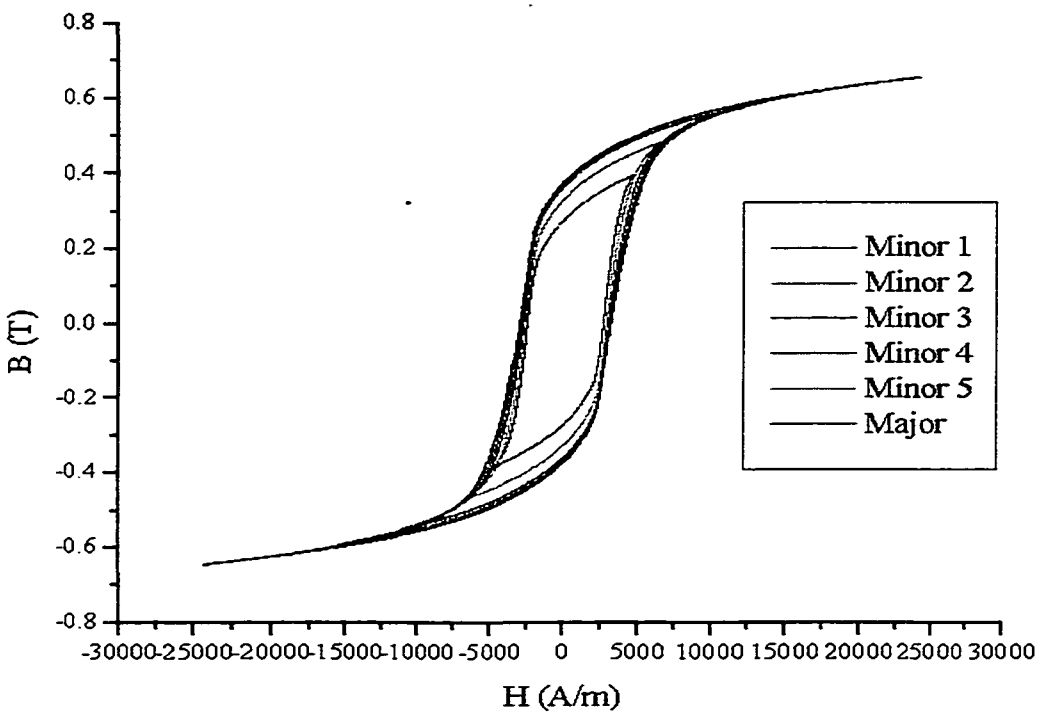

Figure 5-12 Experimental results of minor hysteresis loops

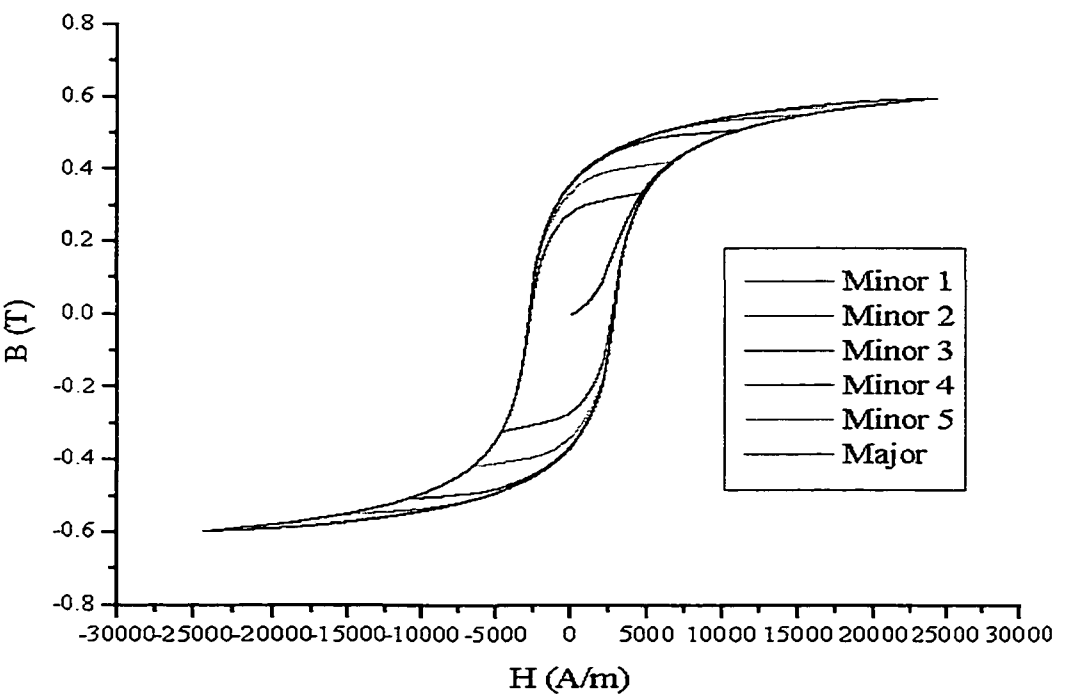

Figure 5-13 Modeling results of minor hysteresis loops

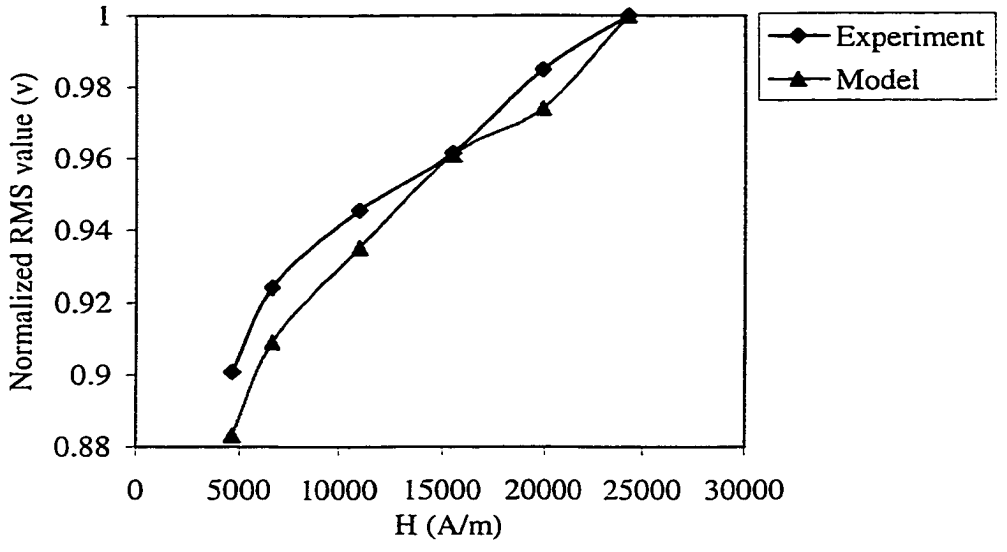

Figure 5-14 Normalized RMS value and magnetic field

The experimental and modeled RMS results of the BE signals exhibited the similar trend as shown in Figure 5-14. It was observed that the RMS value of the BE signals increases with the increasing magnetic field.

5.5 Conclusion

A new magnetic Barkhausen model, which incorporates the ideas from both the ABBM and JSW model is described in this chapter. The non-linear irreversible differential permeabilities are input into the new model by extracting values from the Jiles-Atherton hysteresis model. The Gaussian distributed background noise is also integrated into the new model and the systematic comparisons between the modeling and experimental results show that the new model can accurately reproduce the experimental Barkhausen signals.

6 MICROMAGNETIC MODELING OF EFFECTS OF STRESS ON MAGNETIC PROPERTIES

6.1 Introduction

It has been observed experimentally that the magnitude of the vector magnetization $\boldsymbol{M}$ is uniform throughout a homogeneous specimen of a ferromagnet at uniform temperature. This condition forms a non-linear constraint for the Cartesian magnetization components: $(M_x^2 + M_y^2 + M_z^2 = M_s^2)$. However the direction of $\boldsymbol{M}$ is in general not uniform throughout an entire ferromagnetic material, but varies from one region to another. The uniformity of direction is attained only by applying a field, or by choosing as a specimen a body which is itself of microscopic dimensions. The tendency of a ferromagnetic specimen to break up into "domains", with their vector magnetizations oriented differently, is a consequence of minimization of magnetostatic energy and this explains the existence of a demagnetized state.

In the domain theory, the magnetization is constrained to be homogeneous inside the domains, and its direction to vary only within the domain walls. Instead of using the traditional domain theory, Brown proposed a more general theory, called *micromagnetics* [11]. In this theory, the constraints in the domain theory are relaxed and the vector magnetization $\boldsymbol{M}$ has a direction which is a continuous function of its position x, y, z in the specimen. Then the various energy terms (exchange, anisotropy, magnetostatic, etc) are expressed in terms of these directions throughout the specimen. The resulting equations are then solved for the spin directions at all points. In thermodynamic equilibrium, the orientation of $\boldsymbol{M}$ at each point must be such that the total torque on each moment element is zero.

Although stress has an important role in magnetism [36], it is surprising that modeling of magnetization processes in thin films in the presence of external stresses has received little attention. A magnetomechanical model has been developed by Sablik and Jiles [90, 91] to describe the stress effect on magnetic properties of bulk materials. However, recent experimental results obtained from nickel thin films [92] showed a stress dependence of the hysteresis loop properties different from the predictions of the Sablik-Jiles model. Such differences can be attributed to the different mechanisms of magnetization reversal in thin films and bulk materials [92]. In order to investigate the stress effect in magnetic thin films, a new micromagnetic model based on the Landau-Lifshitz-Gilbert (LLG) equation [93, 94] has been developed. The magnetoelastic energy term [17] induced by an external stress was included in the Gibbs free energy of the material. The magnetic moment configuration was calculated by solving the LLG equation. The modeling results show that the hysteresis loop properties, such as coercivity and remanence, change drastically with applied stress in a way different from that of bulk magnetic materials. These results are in good agreement with experimental data on nickel thin films reported in the literature [92].

6.2 Ferromagnetic spin resonance

The torque τ on a magnetic dipole of moment $\boldsymbol{m}$ when subjected to an applied magnetic field $\boldsymbol{H}$ is given by

$$\tau = \mu_0 \boldsymbol{m} \times \boldsymbol{H} \quad . \tag{6-1}$$

Therefore, the torque tends to align the magnetic dipole along the field direction. In the absence of damping, the magnetic moment may go into precession, in which its orientation oscillates about the field direction at an angle that is dependent upon its initial

orientation. In this case, the rate of change of magnetization is proportional to the torque τ

$$\frac{\partial \boldsymbol{M}}{\partial t} = -\gamma \boldsymbol{\tau} \quad , \tag{6-2}$$

where the gyromagnetic ratio γ is defined as

$$\gamma = -\mu_B g(2\pi / h) \quad , \tag{6-3}$$

where μ_B is the Bohr magneton, g is the Landé splitting factor of the electron and h is Planck's constant. For a free electron, the value of γ is 1.76×10^{11} rad s^{-1} T^{-1}. The solutions of (6-2) yield a constant component along the direction of the applied field and a sinusoidal component with a fixed frequency ω_0 in the plane normal to the direction of the field:

$$\omega_0 = \gamma \mu_0 H \quad . \tag{6-4}$$

This shows that in the absence of damping there is a spin resonance at a frequency which increases linearly with the applied field strength. In practice, the effective value of H in the above equation is strongly affected by demagnetizing effects, and internal fields due to exchange and anisotropy.

In the presence of damping, the equation of motion must be modified. Landau and Lifschitz treated this problem and gave the following equation of motion known as the Landau-Lifschitz equation [93]:

$$\frac{\partial \boldsymbol{M}}{\partial t} = -\gamma \mu_0 \boldsymbol{M} \times \boldsymbol{H} - \frac{4\pi \lambda_d}{M^2}(\boldsymbol{M} \times \boldsymbol{M} \times \boldsymbol{H}) \quad , \tag{6-5}$$

where λ_d is the damping coefficient. Subsequently, Gilbert [94] derived a modified form

of this equation in which he considered that the damping of the motion should depend on the resultant motion $\frac{\partial \boldsymbol{M}}{\partial t}$ and proposed the alternative equation

$$\frac{\partial \boldsymbol{M}}{\partial t} = -\gamma\mu_0 \boldsymbol{M} \times \boldsymbol{H} + \frac{4\pi\lambda_d}{\gamma\mu_0 M^2}(\boldsymbol{M} \times \frac{\partial \boldsymbol{M}}{\partial t}) \quad . \tag{6-6}$$

This Landau-Lifschitz-Gilbert (LLG) equation is a generalization of the Landau-Lifschitz equation since the latter can be derived from this equation by neglecting the higher-order terms in the expression for $\frac{\partial \boldsymbol{M}}{\partial t}$ on the right-hand side of the equation.

Critical damping of the motion of the magnetic moments occurs when $\lambda_d = \gamma\mu_0 M / 4\pi$. For values of $\lambda_d << \gamma\mu_0 M / 4\pi$, the spins perform a number of precessions before finally reaching the field direction. While for $\lambda_d >> \gamma\mu_0 M / 4\pi$, the spins will rotate slowly but directly toward the field direction. The value of this relaxation frequency λ_d is typically 10^7-10^8 $s^{-1}$for nickel-zinc ferrite and manganese-zinc ferrite, and is generally in the range of 10^6-10^9 s^{-1} for other materials.

6.3 Solving micromagnetic problems

Solving problems in micromagnetics means finding an equilibrium magnetization configuration of a ferromagnetic body by minimizing its free energy under certain conditions. According to the phenomenological theory used in micromagnetics, the free energy of a ferromagnetic body with a magnetization configuration $\boldsymbol{M}(\vec{r})$ can be written as a sum of several energy contributions:

$$E_{tot} = E_{ext.field} + E_{exch} + E_{anis} + E_{demag} \quad , \tag{6-7}$$

where $E_{ext.field}$ is the energy contribution due to an external field, E_{exch} is the exchange energy, E_{anis} is the anisotropy energy, and E_{demag} is the demagnetizing or stray field energy. In general, the effective field $\boldsymbol{H}_{eff}$ acting on a given magnetic moment can be defined as a derivative of the corresponding energy term as

$$\boldsymbol{H}_{eff} = -\frac{1}{\mu_0}\frac{\partial E}{\partial \boldsymbol{M}} \quad , \tag{6-8}$$

Correspondingly, the effective field can be written as a sum of several field components:

$$\boldsymbol{H}_{eff} = \boldsymbol{H}_{ext.field} + \boldsymbol{H}_{exch} + \boldsymbol{H}_{anis} + \boldsymbol{H}_{demag} \quad , \tag{6-9}$$

where the $\boldsymbol{H}_{ext.field}$ is the external applied field, $\boldsymbol{H}_{exch}$ is the exchange coupling field, $\boldsymbol{H}_{anis}$ is the crystalline anisotropy field and $\boldsymbol{H}_{demag}$ is the magnetostatic field. At equilibrium, the magnetization vector $\boldsymbol{M}$ must be parallel to $\boldsymbol{H}_{eff}$ thus eliminating any torques acting on the atomic spins.

6.3.1 The continuous formulation of micromagnetics

Within the conventional continuum theory approach, the energy terms in (6-7) can be formulated as functions of the unit vector $\boldsymbol{m} = \boldsymbol{M}/M_s$ and of reduced fields $\boldsymbol{h} = \mu_0 \boldsymbol{H}/M_s$. According to this, the four energy terms for a sample of volume V are defined as follows.

(1) External field energy $E_{ext.field}$:

$$E_{ext.field} = -\mu_0 \int_V \boldsymbol{M}(\vec{r}) \bullet \boldsymbol{H}_{ext}(\vec{r}) dV = -M_s^2 \int_V \boldsymbol{m}(\vec{r}) \bullet \boldsymbol{h}_{ext}(\vec{r}) dV \quad . \tag{6-10}$$

Here $\boldsymbol{h}_{ext}(\vec{r})$ is the reduced external field (which can be non-uniform) and the "•" represents vector dot product.

(2) Exchange energy E_{exch}:

The exchange interaction has its basis in the quantum mechanical exchange interaction of neighboring electron spins with the result that the electron spins of the atoms tend to align parallel or antiparallel to each other [24]. The continuum approximation to this quantum mechanical term can be written as

$$E_{exch} = A\int_V [(\nabla m_x)^2 + (\nabla m_y)^2 + (\nabla m_z)^2]dV \quad . \tag{6-11}$$

Here A is the exchange stiffness constant and m_x, m_y, m_z are the components of $\boldsymbol{m}$ along the x, y, z axes respectively.

(3) Anisotropy energy E_{anis}:

The magnetocrystalline anisotropy tends to align the magnetization along the crystalline axis in the material. Two common crystal types are usually considered. For uniaxial symmetry the anisotropy energy is given by

$$E_{anis} = K_u \int_V (1 - m_z^2)dV \quad , \tag{6-12}$$

where K_u is the anisotropy constant and the above equation assumes a uniaxial magnetic anisotropy along the z-axis. For cubic symmetry the energy is

$$E_{anis} = K_c \int_v (m_x^2 m_y^2 + m_y^2 m_z^2 + m_x^2 m_z^2)dV \quad . \tag{6-13}$$

(4) Demagnetizing or stray field energy E_{demag} [95]:

$$E_{demag} = -K_d \mu_0 \int_v \boldsymbol{m}(\vec{r}) \bullet \boldsymbol{h}_{demag}(\vec{r}) dV \quad , \tag{6-14}$$

where the K_d is the stray field energy constant $K_d = M_s^2 / 2\mu_0$ ($=2\pi M_s^2$ in the Gaussian system), $\boldsymbol{h}_{demag}$ is the demagnetizing or stray field defined by the two conditions: $roth_{demag}=0$ and $div\boldsymbol{h}_{demag}=-div\boldsymbol{m}$. Therefore, the demagnetizing field can be represented as a gradient of a scalar magnetic potential

$$\boldsymbol{h}_d(\vec{r}) = -\nabla\phi(\vec{r}) \quad , \tag{6-15}$$

where the potential $\phi(\vec{r})$ is derived with the tools of potential theory from the "magnetic volume charges" $Q(\vec{r}) = -div\boldsymbol{m}(\vec{r})$ in analogy with the corresponding electrostatic problem. Hence, (6-14) can be rewritten as [96]

$$E_{demag} = K_d \mu_0 \int_V Q(\vec{r})\phi(\vec{r}) dV \quad . \tag{6-16}$$

Magnetic surface charge ($\boldsymbol{m} \bullet \boldsymbol{n}$ at a free surface with normal $\boldsymbol{n}$, or $(\boldsymbol{m}_1 - \boldsymbol{m}_2) \bullet \boldsymbol{n}$ at an interface between two materials with reduced magnetization $\boldsymbol{m}_1$ and $\boldsymbol{m}_2$) will also contribute to the potential ϕ and to the demagnetizing energy.

To find the equilibrium magnetization distribution, the total energy E_{tot} must be minimized with respect to the magnetization configuration under two conditions:

- The absolute value of the magnetization is constant and is equal to the saturation to the saturation magnetization of the ferromagnetic body under consideration, leading to the constraints in reduced units

$$m_x^2 + m_y^2 + m_z^2 = 1 \quad . \tag{6-17}$$

- The normal derivative of the magnetization on a free surface should vanish, *i.e.*

$$\partial \boldsymbol{m} / \partial \boldsymbol{n} = 0 \quad . \tag{6-18}$$

6.3.2 The discrete formulation of micromagnetics

The continuous magnetization within the ferromagnetic body can be approximated by a discrete distribution over a finite number of points. The direction of magnetization at each of these points is free to vary arbitrarily. The integrals and derivatives in the continuous energy expressions are replaced by finite sums and differences in terms of these unknown magnetization components. The total energy is then minimized with respect to the discrete distribution through an iterative calculation. This approach has the significant advantage that the equilibrium magnetization configuration and corresponding energy are generated in the course of the minimization.

In our micromagnetic modeling, the ferromagnetic body is taken as a homogeneous infinite sheet parallel to the x-z plane with width a along the x coordinate

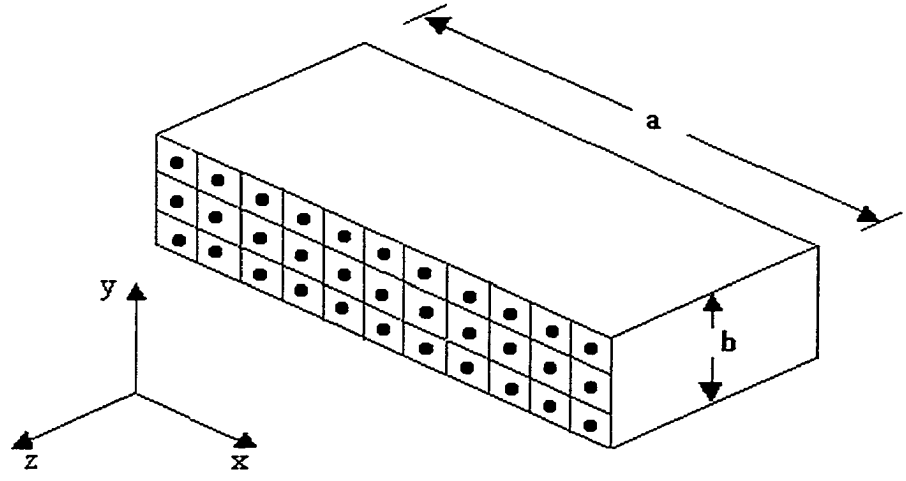

Figure 6-1 Discrete partition for the two-dimensional micromagnetic problem

and thickness b along the y coordinate as shown in Figure 6-1. The region $(0 \le x \le a,\ 0 \le y \le b)$ is partitioned into $N_x \times N_y$ cubes of side Δ. This implies that both the width a and thickness b are integral multiples of the cell size Δ. The restriction to a square cross section has the distinct advantage that the demagnetizing factors for the individual cube do not introduce any artificial symmetries in the discrete characterization. Also, certain symmetries in the magnetostatic interactions between cubes may be exploited.

The cubes are indexed as $1 \le i \le N_x$ and $1 \le j \le N_y$. Each cube is then assumed to exhibit uniform magnetization . The direction of magnetization $\boldsymbol{m}$ is free to vary over the grid of points $\{1 \le i \le N_x, 1 \le j \le N_y\}$, but $\boldsymbol{m}$ must satisfy (6-17) at each point of the grid. Furthermore, the boundary conditions have to be considered according to (6-18). This can be solved by mirroring the grid as shown in Figure 6-2, which makes it continuing outside the actual boundary.

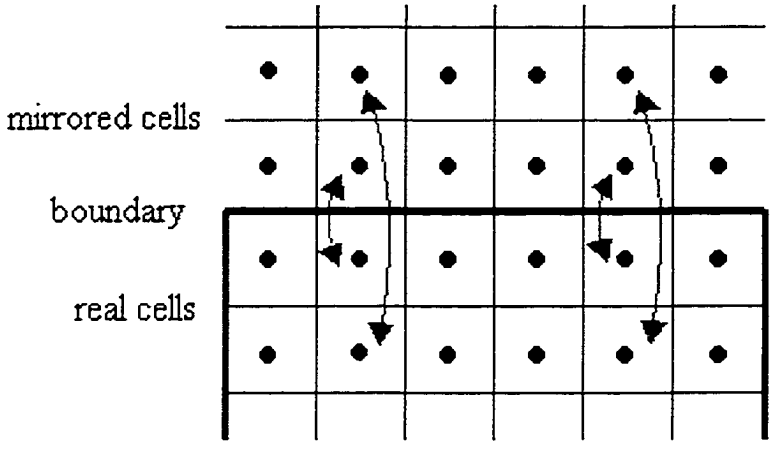

Figure 6-2 The boundary condition can be fulfilled by a continuation at the grid with mirror cells

The energy expressions are developed directly in terms of the discrete distribution $\{\boldsymbol{m}(i,j)\}$. The discrete formulation of external field energy, exchange energy, anisotropy energy and demagnetizing energy are defined as follows.

(1) External field energy $E_{ext.field}$:

$$E_{ext.field} = -M_s^2 \sum_{i=1}^{N_x} \sum_{j=1}^{N_y} \boldsymbol{m}(i,j) \bullet \boldsymbol{h}_{ext}(i,j) \quad . \tag{6-19}$$

Here, $\boldsymbol{h}_{ext}(i,j)$ is the reduced external field at the grid position (i,j).

(2) Exchange energy E_{exch}:

For the discrete magnetization $\boldsymbol{m}(i,j)$, there are several choices for the representation of (6-11) that correspond to a particular choice of interpolation of the magnetization between grid points.

- Four-neighbor dot product

The most commonly reported representation of the exchange energy is a four neighbor dot product [97, 98]:

$$E_{exch} = A \sum_{i=1}^{N_x} \sum_{j=1}^{N_y} \sum_{nn=1}^{4} (1 - \boldsymbol{m}(i,j) \bullet \boldsymbol{m}_{nn}) \quad . \tag{6-20}$$

The inner sum is performed over the 4 nearest neighbors of the grid point (i,j). Using this representation of the exchange energy, the exchange field at the grid point (i,j) is given by

$$\boldsymbol{H}_{exch}(i,j) = \frac{2A}{\mu_0 M_s^2 \Delta^2} \left[\boldsymbol{m}(i+1,j) + \boldsymbol{m}(i-1,j) + \boldsymbol{m}(i,j+1) + \boldsymbol{m}(i,j-1) - 4\boldsymbol{m}(i,j) \right] . \tag{6-21}$$

- Eight-neighbor dot product

In this scheme [99], the magnetization between the discretization gird points is interpolated from the moments at the four nearest grid points. Inside a cell with moments $\boldsymbol{m}(i,j)$, $\boldsymbol{m}(i+1,j)$, $\boldsymbol{m}(i,j+1)$ and $\boldsymbol{m}(i+1,j+1)$ at the four corners, the magnetization $\boldsymbol{m}(x,y)$ is given by

$$\begin{aligned}\boldsymbol{m}(x,y) = (1-x)(1-y)\boldsymbol{m}(i,j) + xy\boldsymbol{m}(i+1,j+1) \\ +(1-x)y\boldsymbol{m}(i,j+1) + x(1-y)\boldsymbol{m}(i+1,j)\end{aligned} \quad , \tag{6-22}$$

where x and y are in units of the grid spacing. This interpolation allows the magnetization of $\boldsymbol{m}$ to be continuous everywhere.

Using this interpolation, the gradients appearing in (6-11) are found from straightforward differentiation of (6-22). The exchange equation is given by

$$E_{exch} = \frac{A}{3}\sum_{i=1}^{N_x}\sum_{j=1}^{N_y}\sum_{nn=1}^{8}(1-\boldsymbol{m}(i,j)\bullet\boldsymbol{m}_{nn}) \quad , \tag{6-23}$$

where the inner sum is over the four nearest and four next-nearest neighbors of node (i,j). The corresponding exchange field at the grid point (i,j) can be expressed as

$$\begin{aligned}\boldsymbol{H}_{exch}(i,j) = \frac{2A}{3\mu_0 M_s^2\Delta^2}[\boldsymbol{m}(i+1,j)+\boldsymbol{m}(i-1,j)+\boldsymbol{m}(i,j+1)+\boldsymbol{m}(i,j-1) \\ +\boldsymbol{m}(i+1,j+1)+\boldsymbol{m}(i-1,j+1)+\boldsymbol{m}(i+1,j-1)+\boldsymbol{m}(i-1,j-1)-8\boldsymbol{m}(i,j)]\end{aligned} \quad . \tag{6-24}$$

(3) Anisotropy energy E_{anis}:

For uniaxial anisotropy along the z axis, the anisotropy energy E_{anis} is

$$E_{anis} = K_u\sum_{i=1}^{N_x}\sum_{j=1}^{N_y}[1-m_z^2(i,j)] \quad . \tag{6-25}$$

Here, $m_z(i,j)$ is the z-axis component of magnetization at the grid point (i,j). The uniaxial anisotropy field components along the x, y, z axes at the grid point (i,j) are

$$H_x^{anis}(i,j)=0,\ H_y^{anis}(i,j)=0,\ H_z^{anis}(i,j)=\frac{2K_u}{\mu_0 M_s^2}m_z(i,j) \quad . \quad (6\text{-}26)$$

For cubic anisotropy, the anisotropy energy E_{anis} can be expressed as

$$E_{anis}=K_c\sum_{i=1}^{N_x}\sum_{j=1}^{N_y}[m_x(i,j)^2 m_y(i,j)^2+m_y(i,j)^2 m_z(i,j)^2+m_x(i,j)^2 m_z(i,j)^2] \quad .(6\text{-}27)$$

The corresponding anisotropy fields along the three axes at the grid point (i,j) are

$$H_x^{anis}=-\frac{2K_c}{\mu_0 M_s^2}m_x(i,j)[m_y(i,j)^2+m_z(i,j)^2] \quad ,$$

$$H_y^{anis}=-\frac{2K_c}{\mu_0 M_s^2}m_y(i,j)[m_x(i,j)^2+m_z(i,j)^2] \quad , \text{ and}$$

$$H_z^{anis}=-\frac{2K_c}{\mu_0 M_s^2}m_z(i,j)[m_x(i,j)^2+m_y(i,j)^2] \quad . \quad (6\text{-}28)$$

(4) Demagnetizing or stray field energy E_{demag}:

Because of its non-local character, the demagnetizing energy is the most difficult of all the energy terms to calculate efficiently. It is convenient to separate the magnetostatic energy into two parts: the self energies of the individual cubes and the interaction energies between cubes. Since the magnetization within each cube is constrained to be uniform, there are no effective free poles in the interior of the cubes.

Suppose $\boldsymbol{h}_{demag}(i,j;k,l)$ denotes the stray field contribution generated by $\boldsymbol{m}(k,l)$ inside the cell (i,j), if $(i,j)\neq(k,l)$, $\boldsymbol{h}^{demag}(i,j;k,l)$ can be calculated as [98]:

$$h_x^{demag}(i,j;k,l) = A(k-i,l-j)m_x(k,l) + C(k-i,l-j)m_y(k,l) \quad , \qquad (6\text{-}29)$$

$$h_y^{demag}(i,j;k,l) = C(k-i,l-j)m_x(k,l) - A(k-i,l-j)m_y(k,l) \quad . \qquad (6\text{-}30)$$

The formulae for *A(i,j)* and *C(i,j)* are given as follows:

$$A(i,j) = \arctan\frac{2(2i-1)}{(2i-1)^2+4j^2-1} - \arctan\frac{2(2i+1)}{(2i+1)^2+4j^2-1} \quad , \qquad (6\text{-}31)$$

$$C(i,j) = -\frac{1}{2}\ln\frac{4i^4+8i^2j^2-8ij+4j^4+1}{4i^4+8i^2j^2+8ij+4j^4+1} \quad . \qquad (6\text{-}32)$$

The self-field, that is, the field inside the cube generated by the magnetization of the cube itself, will be included separately. As a consequence, we can assume *A(0,0)=0* and *C(0,0)=0*. Summing (6-29) and (6-30) and including the self-field, the demagnetizing field at the grid point *(i,j)* can be expressed as

$$h_x^{demag}(i,j) = \sum_{k,l(k,l)\neq(i,j)} [A(k-i,l-j)m_x(k,l) + C(k-i,l-j)m_y(k,l)] - \frac{1}{2}m_x(i,j) \quad ,(6\text{-}33)$$

$$h_y^{demag}(i,j) = \sum_{k,l(k,l)\neq(i,j)} [C(k-i,l-j)m_x(k,l) - A(k-i,l-j)m_y(k,l)] - \frac{1}{2}m_y(i,j) \quad .(6\text{-}34)$$

A direct calculation of these demagnetization field using the above formulae is extremely computationally intensive. The computation of the whole demagnetizing field needs the order of $(N_x^2 \times N_y^2)$ floating point multiplications. However, the sums in (6-33) and (6-34) have the form of a convolution. As is well known [74] and has already been demonstrated in numerical micromagnetics [100], the computation of convolution sums for large data fields can be substantially speeded up using the convolution theorem and fast Fourier transform (FFT). As mentioned before this is mainly based on the fact that

FFT on a field with N points can be done in $N\log_2 N$ steps and it is much fewer than N^2 for large N.

After we obtain the expression for the demagnetizing field, the demagnetizing energy can be calculated as

$$E_{demag} = -K_d \mu_0 \sum_{i=1}^{N_x} \sum_{j=1}^{N_y} \boldsymbol{m}(i,j) \bullet \boldsymbol{h}_{demag}(i,j) \quad . \tag{6-35}$$

6.3.3 Energy minimization algorithm

After we obtain the expression for the effective field, the right-hand side of (6-5) is complete. The numerical integration of this equation is performed using a first order Euler step to prime the predictor-corrector ODE (ordinary differential equation) solver [74]. A fourth order Runge-Kutta solver is also included in the code which is used as a backup in case the predictor-corrector fails to find a valid step.

After each integration step, it is verified that the total energy of the system has really decreased. If this is the case, the integration step is accepted, otherwise the step is repeated with reduced step size. This procedure is continued until the following condition is reached

$$\max\left|\boldsymbol{m}(i,j) \times \boldsymbol{h}_{eff}(i,j)\right| \le \varepsilon \quad \text{for all } 1 \le i \le N_x, 1 \le j \le N_y \quad , \tag{6-36}$$

where ε is a predefined converge value and its value is typically chosen to be $10^{-6} \sim 10^{-4}$. This condition assures that the component of the effective field perpendicular to the local magnetization vector is simultaneously small at all points. In this way the algorithm leads at least to a local minimum of the micromagnetic energy under the constraint of constant magnitude of the magnetization vector.

6.4 Magnetostriction

The dimension of a ferromagnetic material may change under some circumstances and this effect is called magnetostriction. There are two main types of magnetostriction: spontaneous magnetostriction arising from the ordering of magnetic moments into domains at the Curie temperature, and field-induced magnetostriction. In both cases, the magnetostriction λ is simply defined as the fractional change in length:

$$\lambda = \frac{\Delta l}{l} \quad . \tag{6-37}$$

The value of λ measured at magnetic saturation is called the saturation magnetostriction λ_s, and when the word "magnetostriction" is used without qualification, λ_s is usually meant.

Table 6-1 Magnetostriction coefficients of iron and nickel

Material	λ_{100} (10^{-6})	λ_{111} (10^{-6})
Iron	21	-21
Nickel	-46	-24

The saturation magnetostriction λ_s exhibited by a cubic crystal in a direction defined by the cosines β_1, β_2, β_3 relative to the crystal axes, when it changes from the demagnetized state to saturation in a direction defined by the cosines α_1, α_2, α_3, is given by

$$\lambda_s = \frac{3}{2}\lambda_{100}(\alpha_1^2\beta_1^2 + \alpha_2^2\beta_2^2 + \alpha_3^2\beta_3^2 - \frac{1}{3}) + 3\lambda_{111}(\alpha_1\alpha_2\beta_1\beta_2 + \alpha_2\alpha_3\beta_2\beta_3 + \alpha_3\alpha_1\beta_3\beta_1) \quad . \tag{6-38}$$

where λ_{100} is the saturation magnetostriction measured along the <100> direction and λ_{111} is the saturation magnetostriction along the <111> direction. The magnetostriction constants λ_{100} and λ_{111} of iron and nickel are listed in Table 6-1.

The saturation magnetostriction of a hexagonal crystal is given by the following equation:

$$\begin{aligned}\lambda_s = {} & \lambda_A[(\alpha_1\beta_1 + \alpha_2\beta_2)^2 - (\alpha_1\beta_1 + \alpha_2\beta_2)\alpha_3\beta_3] \\ & + \lambda_B[(1-\alpha_3^2)(1-\beta_3^2) - (\alpha_1\beta_1 + \alpha_2\beta_2)^2] \\ & + \lambda_C[(1-\alpha_3^2)\beta_3^2 - (\alpha_1\beta_1 + \alpha_2\beta_2)\alpha_3\beta_3] \\ & + 4\lambda_D(\alpha_1\beta_1 + \alpha_2\beta_2)\alpha_3\beta_3\end{aligned} \quad . \tag{6-39}$$

where the direction cosines in the above equation are not relative to the hexagonal axes, but to orthogonal axes x, y, z. The magnetostriction constants of cobalt are:

$$\lambda_A = -45\times10^{-6}, \qquad \lambda_B = -95\times10^{-6} \quad ,$$
$$\lambda_C = 110\times10^{-6}, \qquad \lambda_D = -100\times10^{-6} \quad .$$

The magnetostriction constants are usually very small: λ_s is typically of the order of 10^{-5} or 10^{-6}, and they usually decrease in absolute magnitude as the temperature increases and will reach zero at the Curie point. Although the direct magnetostrictive effect is small there exists an inverse effect which causes such properties as permeability and the shape of the hysteresis loop to be highly dependent on stress in many materials. Magnetostriction therefore has many practical consequences, and a great deal of research has accordingly devoted to it.

6.5 Main contribution: Modeling of effects of stress on magnetic properties

6.5.1 Effect of stress on magnetization

The effects of stress on magnetization is normally referred to as magnetomechanical effect. It has been shown experimentally that there is a close relationship between the magnetostriction λ of a material and its magnetic behavior under stress.

Stress can create an easy axis of magnetization. Therefore, when stress (residual or applied) is present, stress anisotropy must be considered along with any other anisotropies that may exist. It is a uniaxial anisotropy, and the corresponding magnetoelastic energy E_{me} is defined as [17]

$$E_{me} = -\frac{3}{2}\lambda_{100}|\sigma|(\alpha_1^2\gamma_1^2 + \alpha_2^2\gamma_2^2 + \alpha_3^2\gamma_3^2)$$

$$-3\lambda_{111}|\sigma|(\alpha_1\alpha_2\gamma_1\gamma_2 + \alpha_2\alpha_3\gamma_2\gamma_3 + \alpha_3\alpha_1\gamma_3\gamma_1) \quad . \qquad (6\text{-}40)$$

where $|\sigma|$ is the stress magnitude, α_1, α_2, α_3 are the direction cosines of $\boldsymbol{M}$, and γ_1, γ_2, γ_3 are the direction cosines of $\boldsymbol{\sigma}$ with respect to the crystal axes.

Like the energy terms introduced before, the magnetoelastic energy E_{me} and the corresponding effective field $\boldsymbol{H}_{me}$ can be integrated into the LLG equation to model how the magnetic moments change under an applied stress. The discrete formulation of the magnetoelastic energy E_{me} can be expressed as a function of unit magnetization vector m and unit stress vector $\boldsymbol{\delta} = \boldsymbol{\sigma}/|\sigma|$, where $|\sigma|$ is the magnitude of $\boldsymbol{\sigma}$.

$$E_{me} = \sum_{i=1}^{N_x}\sum_{j=1}^{N_y}\{-\frac{3}{2}\lambda_{100}|\sigma(i,j)|[m_x(i,j)^2\delta_x(i,j)^2 + m_y(i,j)^2\delta_y(i,j)^2 + m_z(i,j)^2\delta_z(i,j)^2] - 3\lambda_{111}|\sigma(i,j)|[m_x(i,j)m_y(i,j)\delta_x(i,j)\delta_y(i,j) + m_y(i,j)m_z(i,j)\delta_y(i,j)\delta_z(i,j) + m_z(i,j)m_x(i,j)\delta_z(i,j)\delta_x(i,j)]\} \quad (6\text{-}41)$$

where the $|\sigma(i,j)|$ is the magnitude of the stress at grid position (i,j). If the stress is uniform, $|\sigma(i,j)| = |\sigma|$. $\delta_x(i,j)$, $\delta_y(i,j)$ and $\delta_z(i,j)$ are the x, y, z components of unit stress vector $\boldsymbol{\delta}$ at the gird position (i,j) respectively.

The corresponding magnetoelastic fields along the three axes at the grid point (i,j) are

$$H_x^{me} = \frac{1}{\mu_0 M_s^2}\{3\lambda_{100}|\sigma(i,j)|m_x(i,j)\delta_x(i,j)^2 + 3\lambda_{111}|\sigma(i,j)|[m_y(i,j)\delta_y(i,j)\delta_x(i,j) + m_z(i,j)\delta_z(i,j)\delta_x(i,j)]\},$$

$$H_y^{me} = \frac{1}{\mu_0 M_s^2}\{3\lambda_{100}|\sigma(i,j)|m_y(i,j)\delta_y(i,j)^2 + 3\lambda_{111}|\sigma(i,j)|[m_x(i,j)\delta_x(i,j)\delta_y(i,j) + m_z(i,j)\delta_z(i,j)\delta_y(i,j)]\},$$

$$H_z^{me} = \frac{1}{\mu_0 M_s^2}\{3\lambda_{100}|\sigma(i,j)|m_z(i,j)\delta_z(i,j)^2 + 3\lambda_{111}|\sigma(i,j)|[m_x(i,j)\delta_x(i,j)\delta_z(i,j) + m_y(i,j)\delta_y(i,j)\delta_z(i,j)]\}. \quad (6\text{-}42)$$

6.5.2 Modeling results and discussion

The modeling was based on a public domain micromagnetics program OOMMF (Object Oriented Micromagnetic Framework) [101], which is developed by the National Institute of Standards and Technology (NIST Gaithersburg). The magnetoelastic energy E_{me} and the corresponding effective field $\boldsymbol{H}_{me}$ were added to the code, which is written in C++ and TCL/TK, to model the effects of stress on magnetic moments. All the

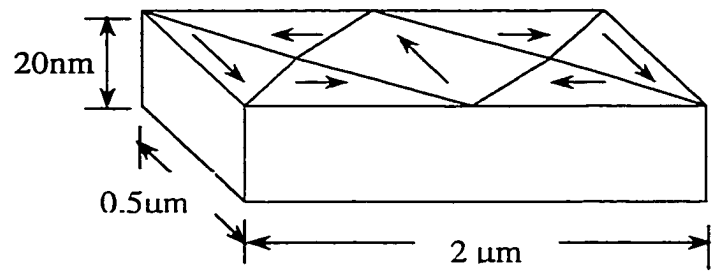

Figure 6-3 Dimension of the rectangular element

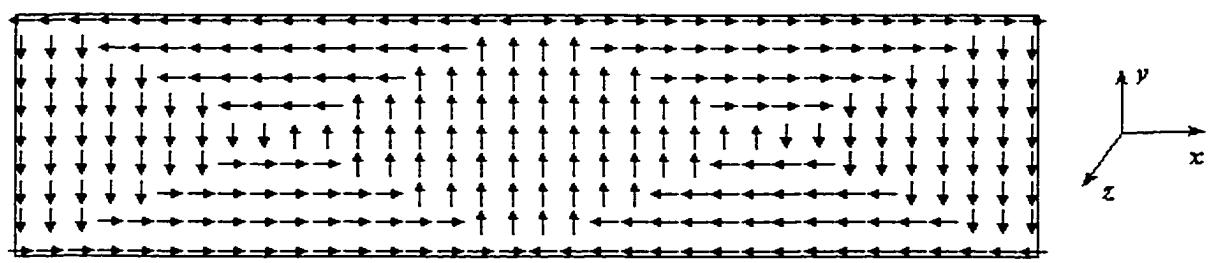

Figure 6-4 Initial configuration of the magnetic moments

simulations were operated on the Windows 98 platform.

A 2 μm wide, 0.5 μm high and 20 nm thick rectangular element with cell size 20nm shown in Figure 6-3 was used in the present study. The demagnetizing field was obtained by calculating the average field in each cell [101] using the formulae from [102]. Figure 6-4 shows the initial configuration of the magnetic moments that contains seven domains.

6.5.2.1 Simulation 1: Effects of stress on magnetic moments

In this simulation, the stress σ was applied on the materials of iron (M_s=1.7e6A/m, K_1 =4.8e4Jm^{-3}, λ_{100}=21e-6, λ_{111}=-21e-6) and nickel (M_s=0.48e6A/m, K_1

=-5.7e4Jm^{-3}, λ_{100}=-46e-6, λ_{111}=-24e-6) respectively along the x direction. Figure 6-5 and Figure 6-6 show the equilibrium configuration of the magnetic moments of iron under the 1GPa tensile and compressive stress respectively. The results show that under the tensile applied stress, the magnetic moments of iron will rotate towards the direction of stress. And when the compressive stress is applied, the magnetic moments of iron will rotate towards the direction which is perpendicular to the applied stress.

By applying an external stress, a further anisotropy is created. If the material has a positive magnetostriction such as iron, when a tensile stress is applied, the induced easy

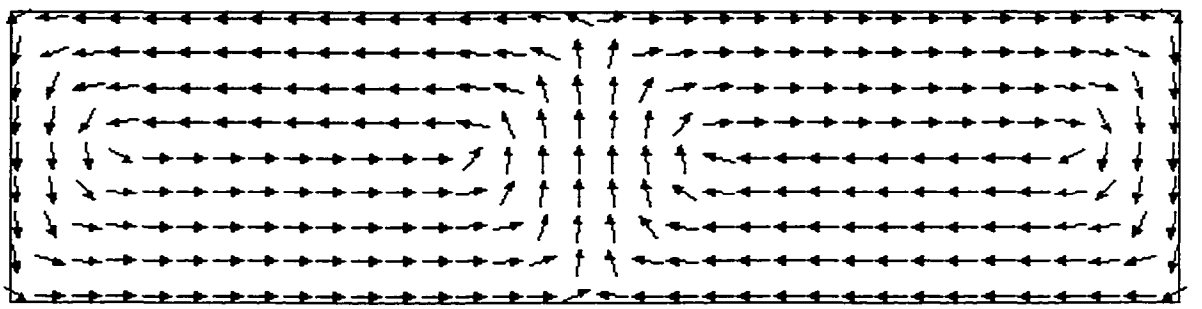

Figure 6-5 Equilibrium configuration of magnetic moments of iron under the 1GPa tensile stress

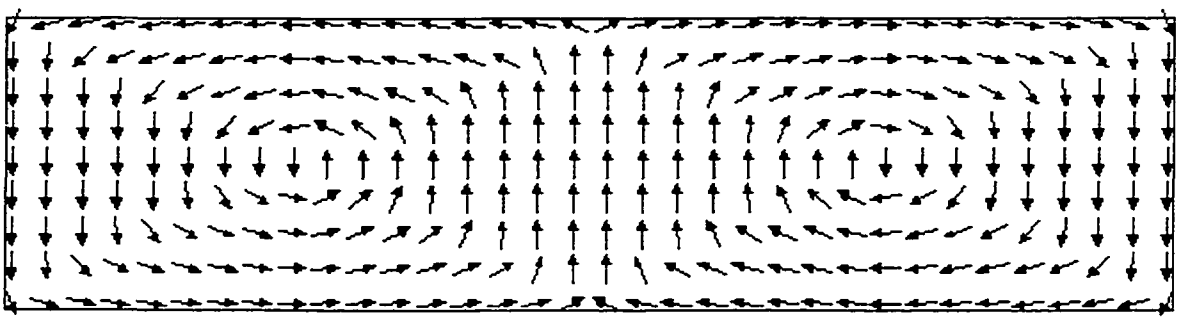

Figure 6-6 Equilibrium configuration of magnetic moments of iron under the 1GPa compressive stress

axis will align along the direction of stress. And when a compressive stress is applied, the induced easy axis will align perpendicular to the direction of stress. However, if the material has a negative magnetostriction such as nickel, the opposite effect will be observed when the external stress is applied as shown in Figure 6-7 and Figure 6-8.

6.5.2.2 Simulation 2: Effects of stress on magnetic properties of nickel thin film

In this simulation, both the stress σ and the magnetic field $\boldsymbol{H}$ were applied along the x direction. The applied field amplitude is 80 kA/m. When calculating the magnetization curves the applied field was stepped (step size = 1600A/m) through in a linear manner. At the end of each field step, when the magnetic moments attained an

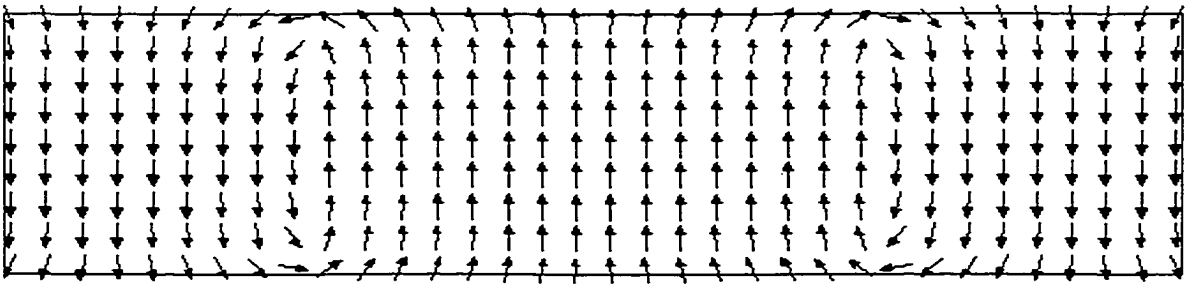

Figure 6-7 Equilibrium configuration of magnetic moments of nickel under the 500MPa tensile stress

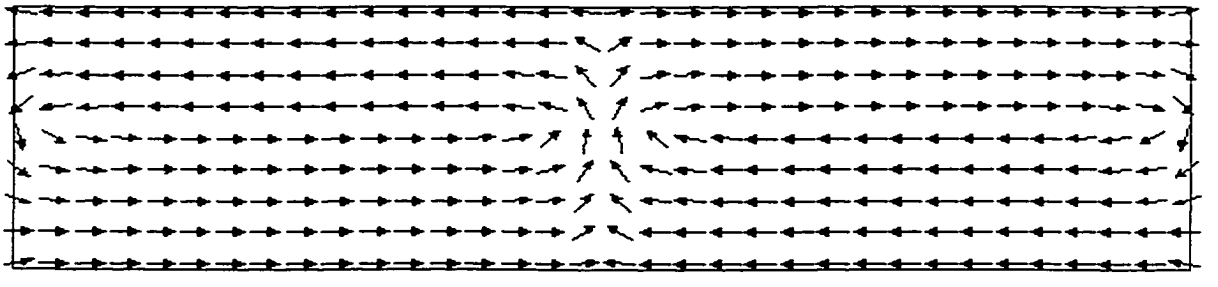

Figure 6-8 Equilibrium configuration of magnetic moments of nickel under the 500MPa compressive stress

equilibrium configuration, the x-components of the magnetic moments were summed over the grid to obtain the magnetization component of the model system in the x-direction which was then plotted against the applied field to obtain the hysteresis loop. Figure 6-9 and Figure 6-10 show the simulated hysteresis loops for a nickel thin film under different levels of tensile and compressive stresses. The hysteresis loop displays systematic changes under the applied stresses.

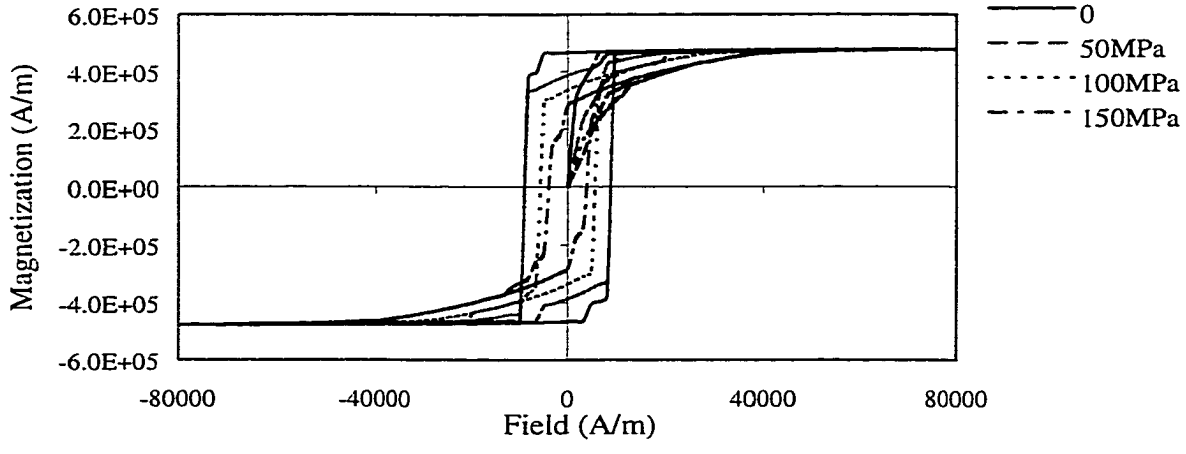

Figure 6-9 Hysteresis loops of nickel thin film under tensile stresses ($\sigma//H$)

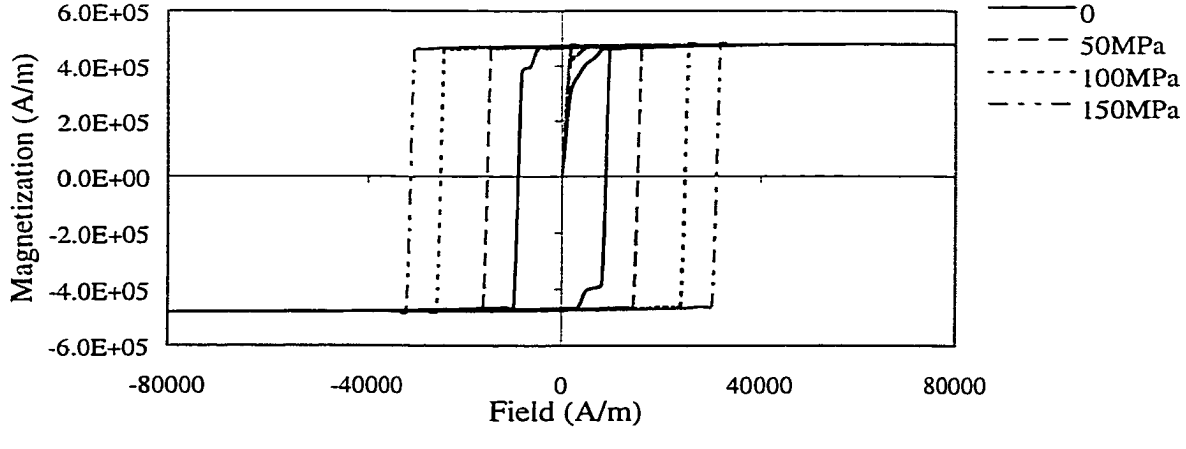

Figure 6-10 Hysteresis loops of nickel thin film under compressive streeses ($\sigma//H$)

Figure 6-11 shows the variation of coercivity due to the applied stress in nickel thin films (relative to the unstressed case). The results show that the coercivity increases significantly with increasing compressive stress and decreases with increasing tensile stress. The modeling results are in good agreement with the experimental data on nickel film [92] but are quite different from those obtained from bulk nickel samples [103]. Such differences can be attributed to the different effects of applied stresses on two different mechanisms of magnetization reversal, namely irreversible domain rotation and domain wall movement [104].

It has been pointed out that when the reversal process is dominated by irreversible domain rotation, the field required to switch the domain magnetization (i.e. the coercivity) will increase if the easy axis induced by the external stress is parallel to the applied field (e.g. compressive stress applied to nickel along the field direction) [104]. This can be explained by considering coherent rotation of domain magnetization against the stress-induced uniaxial anisotropy under an applied field. As described by the Stoner-Wolfarth model [105], the critical field at which the domain magnetization switches abruptly increases with the anisotropy. Therefore it is expected that the coercivity of the model system, whose magnetization reversal process involves essentially irreversible rotation of magnetic moments, will increase with increasing compressive stress applied in the field direction. Similarly the coercivity will decrease if the easy axis induced by the external stress is perpendicular to the applied field (e.g. tensile stress on nickel along the field direction). For the bulk materials, the predominant mechanism is domain wall movement. Quantitative predictions of the effects of stress on magnetic properties of bulk

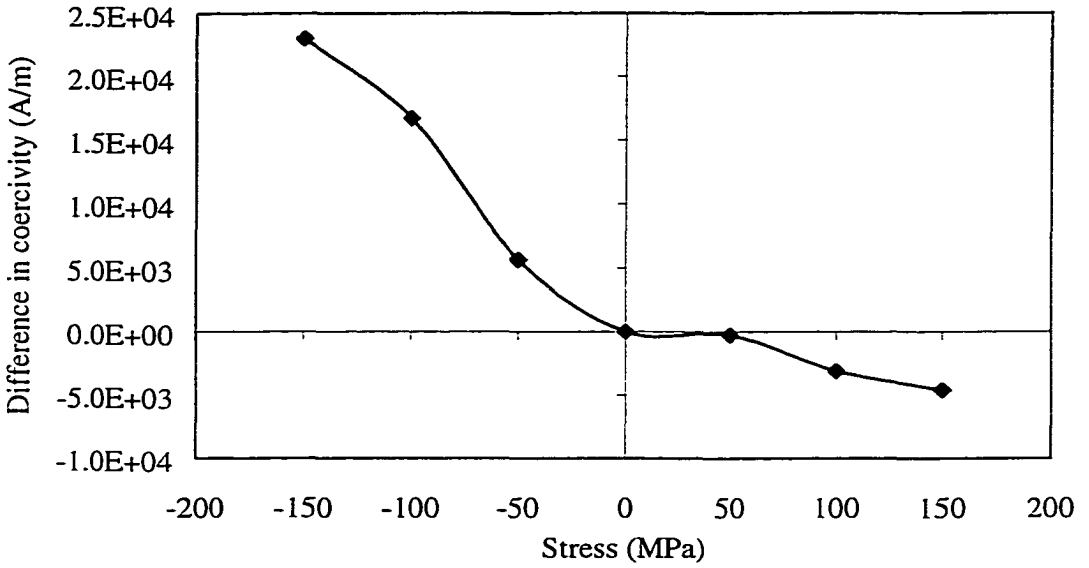

Figure 6-11 The variation of coercivity of nickel thin film under stress ($\sigma I/H$)

materials has been give by Sablik-Jiles model [90, 91], and were found in good agreement with experimental results [92].

Figure 6-12 shows the variation of the remanence in nickel thin films at different stress levels. The results show that the remanence increases with increasing compressive stress and decreases with increasing tensile stress. This can be interpreted based on the argument given above. A tensile stress in the field direction induces an anisotropy perpendicular to the applied field. As the applied field is reduced from saturation, due to the stress-induced anisotropy the domain magnetization may partially rotate reversibly away from the field direction before it suddenly switches to the opposite direction. This effect of reversible rotation becomes more pronounced as the stress-induced anisotropy increases. As a result the remanence decreases with tensile stress. Compressive stress did

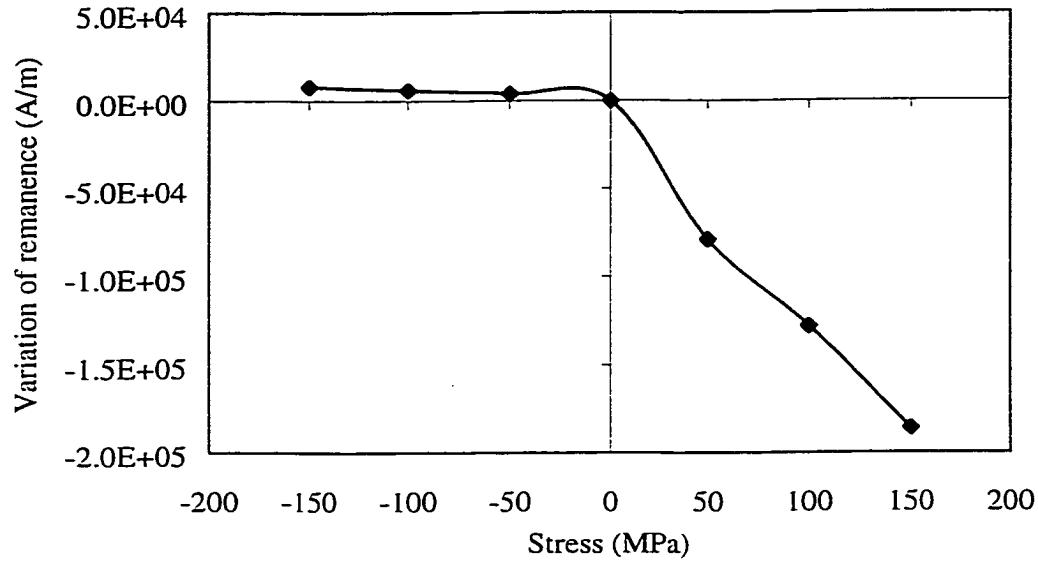

Figure 6-12 The variation of remanence of nickel thin film under stress ($\sigma//H$)

not change the remanence so much because the remanence in the unstressed state was very close to the saturation value, as shown in Figure 6-10.

6.6 Conclusion

A new micromagnetic model has been developed for investigating the effect of stress on the magnetic properties of thin films. This effect has been implemented by including the magnetoelastic energy term into the Landau-Lifshitz-Gilbert (LLG) equation. Magnetization curves of a nickel film were calculated under both tensile and compressive stresses of various magnitudes applied along the field direction. The modeling results show that both coercivity and remanence increased with increasing compressive stress but decrease with increasing tensile stress. The results are in good agreement with the previous experimental results and can be interpreted in terms of the

effects of the applied stresses on the irreversible rotation of magnetic moments during magnetization reversal under an applied field.

7 GENERAL CONCLUSION

In this study, the magnetic Barkhausen effect and its application have been systematically investigated experimentally, theoretically and computationally. The effect of stress on magnetic properties of thin film has also been studied using the micromagnetic (Landau-Lifschitz-Gilbert) modeling approach.

A new multi-functional system for measurement of Barkhausen emission has been developed as part of the research for this thesis. The organization of this system, together with the procedures incorporated into the software, allows flexible control of applied fields and multivariate analysis of the BE signals. Furthermore, Barkhausen effect was measured on two plain carbon steels with different carbon contents. The differences in the Barkhausen results of the samples indicate that Barkhausen effect can be used as a method for material characterization.

It is known that magnetic Barkhausen signal is affected by grain boundaries, carbides, inclusions and dislocations. The individual effects can be distinguished from each other under certain conditions. In the case of carburization, the extensive carbide precipitation due to carbon diffusion dominates the microstructural variation and strongly influences the hardness. These carbide particles pin the domain walls. When carbon was removed it became easier for domain walls to overcome the pinning site. The net effect is an increase in the BE signal with decrease in the carbon content. Furthermore, it has been shown that in the uncarburized region, the Barkhausen signal remains almost constant. This suggests that BE measurement can be used to monitor wear-induced material loss in case-hardened steel. Changes in signal levels were large, in some instances these were greater than 100%, which indicates the high sensitivity of Barkhausen emissions to surface condition. This high sensitivity confirms the practical viability of the Barkhausen

method even in situations where there is likely to be ambient electromagnetic noise. In practice, grinding damage will often occur in a single direction leading to surface anisotropy. The experimental results have shown that the detected Barkhausen signal depends on the orientations of the sensor under these conditions. If this direction is known and does not change from location to location on the surface, then the Barkhausen measurement can be reliably applied. Otherwise the presence of surface anisotropy needs to be taken into account in interpreting the measurements.

Because of its inherent complexity and intrinsic stochastic character, the quantitative description of the Barkhausen effect has proved to be extremely difficult. Nevertheless concurrent research on the description of the underlying processes of the Barkhausen effect has led to the development of theoretical models such as ABBM and JSW models. However, both of these models have their own limitations. The assumptions of ABBM model limit its use to experiments where the differential permeability and time derivative of applied field are constant. The JSW model assumes that the Barkhausen activity in a given time interval is proportional to the rate of change of the irreversible magnetization which can be calculated from hysteresis model. However it is not possible to model the frequency response of the Barkhausen signal using the JSW model. A new BE model incorporating ideas from both of these previous models is presented in this thesis. The Jiles-Atherton hysteresis model was integrated into this new model to calculate the irreversible permeability of the sample. As a result, the new model allows for changes in permeability with applied field and can be used to investigate the BE signal according to the variations of the hysteresis loop. The modeling results are compared with the experimental data in the time and frequency domain separately to test its validity. It shows that the new model can accurately reproduce the experimental BE signals.

In this thesis, a new micromagnetic model has been developed for investigating the effect of stress on the magnetic properties of thin films. This effect has been implemented by including the magnetoelastic energy term into the Landau-Lifshitz-Gilbert (LLG) equation. Magnetization curves of a nickel film were calculated under both tensile and compressive stresses of various magnitudes applied along the field direction. The modeling results show that both coercivity and remanence increase with increasing compressive stress but decrease with increasing tensile stress. The results are in good agreement with the previous experimental results reported in the literature and can be interpreted in terms of the effects of the applied stresses on the irreversible rotation of magnetic moments during magnetization reversal under an applied field.

APPENDIX

[1] "Nondestructive characterization of case-hardened steel", M.J.Johnson, J.Zhou, N.Nakagawa, D.C.Jiles and **B.Zhu,** *Electromagnetic Nondestructive Evaluation (IV)*, edited by S.S.Udpa et al. IOS Press, 2000.

[2] "Evaluation of wear-induced material loss in case-hardened steel", M.J.Johnson, J.Zhou, **B.Zhu**, N.Nakagawa and D.C.Jiles, *Review of Progress in Quantitative Nondestructive Evaluation*, edited by D.O.Thompson and D.E.Chimenti, 2000.

[3] "Multi-functional magnetic Barkhausen emission measurement system", **B.Zhu**, M.J.Johnson, C.C.H.Lo and D.C.Jiles, to be published in *IEEE Transactions on Magnetics*, 2001.

[4] "Evaluation of wear-induced material loss in case-hardened steel using magnetic Barkhausen emission measurement", **B.Zhu**, M.J.Johnson and D.C.Jiles, to be published in *IEEE Transactions on Magnetics*, 2001.

[5] "The effects of aging time and temperature on the magnetic properties of nickel alloys", M.J.Johnson, **B.Zhu**, C.C.H.Lo, D.C.Jiles and R.E.Shannon, to be published in *Review of Progress in Quantitative Nondestructive Evaluation*, 2001.

[6] "Devivation of a non-linear ABBM model for the calculation of Barkhausen effect", S.J.Lee, **B.Zhu**, C.C.H.Lo, D.M.Clatterbuck and D.C.Jiles, to be published in *Review of Progress in Quantitative Nondestructive Evaluation*, 2001.

[7] "Micromagnetic Modeling of the Effects of Stress on Magnetic Properties", **B.Zhu**, C.C.H.Lo, S.J.Lee and D.C.Jiles, accepted for publication in *Journal of Applied Physics*.

[8] "Application of non-linear Barkhausen model incorporating anhysteretic susceptibility to annealed low carbon Fe sample", S.J.Lee, **B.Zhu**, C.C.H.Lo, D.M.Clatterbuck and D.C.Jiles, submitted to the *IEEE Transactions on Magnetics*.

Electromagnetic Nondestructive Evaluation (IV)
S.S. Udpa et al. (Eds.)
IOS Press, 2000

Nondestructive Characterization of Case-Hardened Steel

M. J. Johnson, J. Zhou, N. Nakagawa
D. C. Jiles and B. Zhu
Center for Nondestructive Evaluation
Iowa State University
Ames, Iowa 50011-3042, U.S.A.

Abstract. The measurement of case depth on carburized steel still presents some practical problems. At low frequencies and with the use of large-diameter coils, eddy currents can be used to obtain a fairly reliable measurement of case depth. However, at higher frequencies and with small-diameter coils, conditions often dictated by sample geometry, measurements can be inaccurate. It has been found that permeability measurements made on case-hardened steel samples correlate well with case depth and are largely independent of the effects of tempering. Pulsed eddy current (PEC) and magnetic Barkhausen measurements were shown to be useful in determining the extent of wear-induced material loss from case-hardened steels.

1. Introduction

The measurement of case-depth in carburized steel samples remains a challenging NDE problem. To date we have shown how measurements are made more complicated by the varying microstructural conditions that can exist in steel [1]. This variability can arise as a result of differences in the post-carburizing treatment or because of normal batch-to-batch material variations. The consequence of this variability is that a given inspected component may be of acceptable quality but will have an NDE response indicative of incorrect carburization. Until recently, very little was known about these effects. A set of carburized steel discs has been produced for the purpose of studying the effects of quenching and tempering on NDE measurements. Magnetic hysteresis and pulsed eddy-current measurements were found to be less sensitive to subtle microstructural changes while maximizing sensitivity to changes in case depth.

In addition, the evaluation of wear-induced material loss in case-hardened steel was also shown to be possible using magnetic hysteresis and pulsed eddy-current measurements. Case-hardened steels are frequently used in high-wear applications where friction between moving parts will slowly lead to erosion of the case. It is important to be able to characterize the case loss so that components can be replaced prior to failure. The challenges in determining case erosion are twofold: Firstly, the action of friction on a component will modify its near-surface microstructure, and secondly, the hardness depth profile will be different to that of a newly hardened component meaning that knowledge acquired from measurements on standard case-hardened steel samples may not necessarily apply. Despite these complications, it should be possible to determine wear-induced material loss by using magnetic and pulsed eddy-current techniques.

2. Measurements on case-hardened samples

There are a number of reasons why the measurement of case depth is difficult [1]. Eddy-current penetration depth, even at the low-frequency end of a typical commercial instrument's capability, is often considerably less than the case depth of the sample being measured (around 0.5 to 2.5 mm). In addition, surface properties can vary from sample to sample in a manner that is completely unrelated to case depth. For example, the concept of a thin magnetic 'dead layer' of reduced permeability was proposed by Rose [2] for soft magnetic materials such as nickel. In magnetically hard materials such as steel, this layer is unlikely to be as pronounced, however, even a small effect could have a strong influence on magnetic Barkhausen and moderate- to high-frequency eddy-current measurements. In addition, near-surface microstructure is related to the heat-treatment conditions after carburizing. So, for example, variations in tempering will have a marked effect on surface magnetic properties [3] but will have little effect on case depth. Assuming these variations in surface properties are acceptable in terms of product quality then a means by which their effects can be removed from the eddy-current and magnetic measurements is required. We have explored the use of magnetic and pulsed eddy-current techniques as a means to enhance our ability to characterize case-hardened steel. To better understand how results can be altered by different heat-treatment conditions, case-hardened samples have been acquired that have been subjected to both standard and nonstandard heat-treatment conditions. Initial studies cover the effects of tempering, a procedure that slightly softens the steel making it less prone to cracking, on magnetic and pulsed eddy-current measurements.

A set of gas-carburized steel discs was obtained for the purpose of studying the effects of tempering on the NDE measurements. The discs, cut from a rod of 8620 steel, were 75 mm in diameter and 25 mm thick. Nominal case depths ranged from 0.5 to 2.50 mm with three samples at each depth, A, B and C. Samples from sets A and B were nominally identical whereas those from set C were not tempered after quenching.

Magnetic hysteresis measurements (obtained using the Magnescope, a magnetic inspection instrument developed at the Center for NDE) and pulsed eddy-current measurements were carried out on the samples. It was found that some of the parameters obtained from the hysteresis measurements correlated well with case depth. Coercivity was found to be a particularly sensitive parameter, Fig. 1, although the differential permeability, Fig. 2, and magnetic remanence were also good. Coercivity measurements carried out on the tempered and untempered samples exhibited clear differences whereas tempering had little effect on the maximum differential permeability results. Clearly, using coercivity measurements alone one would be unable to distinguish between the effects of tempering and case depth. However, measurements of the maximum differential permeability are much less sensitive to the effects of tempering and could possibly be used as an independent measure of case depth.

Pulsed eddy-current measurements [4] were also carried out. In these experiments, the response of an unhardened sample was taken as a reference and subtracted from all subsequent measurements. Under these conditions, a good relationship was observed between case depth and peak pulse amplitude for samples with case depths up to around 2 mm. For samples with treatment depths greater than 2 mm, the eddy currents did not penetrate sufficiently far to enable an accurate measurement.

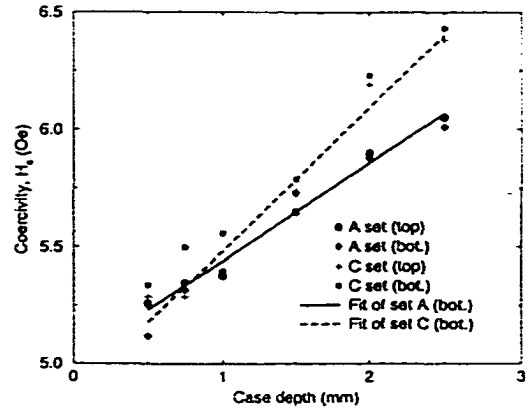

Fig. 1. Measurements of coercivity as a function of case depth. Three measurements were carried out on each side of the sample (to check for treatment uniformity) and an average value taken. Set A samples were treated normally whereas set C samples were not tempered after quenching.

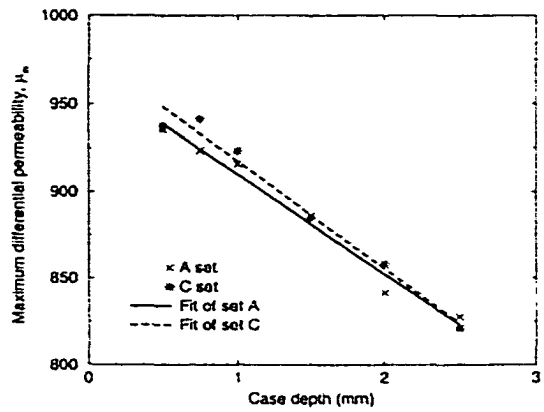

Fig. 2. Measurements of maximum differential permeability, μ_m, as a function of case depth. Results shown are the average of three measurements taken on either side of the sample. This parameter is less sensitive to tempering.

3. Measurement of wear-induced material loss

The evaluation of wear-induced material loss in case-hardened steel samples has also shown to be possible using magnetic and pulsed eddy-current measurements. Case-hardened steels are frequently used in high-wear applications where friction between moving parts will slowly lead to erosion of the case. If it were possible to monitor wear rates, components could be replaced in the most timely and cost-effective manner. However, there are some complications involved with this type of measurement: Firstly, the action of friction on a component will modify its near-surface microstructure, and hence magnetic permeability, in a way that will depend on the exact nature of wear and will be difficult to predict. Secondly, the shape of the hardness depth profile will vary as material is removed. Despite these complications, it should be possible to determine wear-induced material loss by using magnetic and pulsed eddy-current techniques.

To carry out the study, two of the gas-carburized steel discs were selected. Material was removed from each disc by surface grinding in increments ranging from around 100 μm to nearly 300 μm. Disc 1 was also polished and etched so that micrographs could be obtained. Vickers micro-hardness indentation tests were also carried out on Disc 1. Magnetic Barkhausen measurements (obtained using the Magneprobe, an inspection instrument developed at the Center for NDE) were conducted before and after each grinding and/or polishing operation. The surface of Disc 2 was found to be highly anisotropic due to the surface grinding action, Fig. 3. The anisotropy had a strong effect on the Barkhausen measurements since the applied field was mostly uniaxial. In fact, a plot of peak RMS Barkhausen activity versus the angular position of the probe produced a near-sinusoidal response, Fig. 4. Peaks in the Barkhausen response occur at probe orientations of around 0° and 180° and correspond to directions parallel to the surface grinding pattern. A good relationship was observed, for both Disc 1 and Disc 2, between the amount of material removed and the magnetic Barkhausen activity, Fig. 5. From the hardness profile of Disc 2, Fig. 6, it can be seen that a further 0.5 to 0.6 mm of material can be removed before the case hardened layer is completely gone. We would expect to observe further increases in Barkhausen activity down to a depth of 1.5 mm below the original surface, i.e. to a point where the exposed material becomes completely soft. This illustrates the suitability of the Barkhausen technique to monitoring wear-induced material loss. In practice, grinding damage will often occur in a single direction leading to surface anisotropy. If this direction is known and remains constant then the Barkhausen technique can be reliably applied. Fig. 7 shows the microstructure at various different depths. The hard surface is characterized by a fine microstructure (acicular martensite) containing many domain-wall pinning sites; Barkhausen activity from this region of the steel is low. A coarser microstructure, consisting of acicular and lath martensites, is found deeper below the surface; this region will give rise to relatively high levels of Barkhausen activity.

Pulsed eddy-current measurements show a general trend of decreasing pulse amplitude with material loss, Fig. 8. This is because, as with the case-depth measurements, a reference signal is obtained from a soft or unhardened sample. This means that the signal amplitude gets less as the properties of the measurement sample approach those of the reference sample. As material is removed from the case-hardened steel disc, the surface properties of the disc approach those of untreated steel and so the measurement pulse shape and amplitude will approach that obtained from the reference sample.

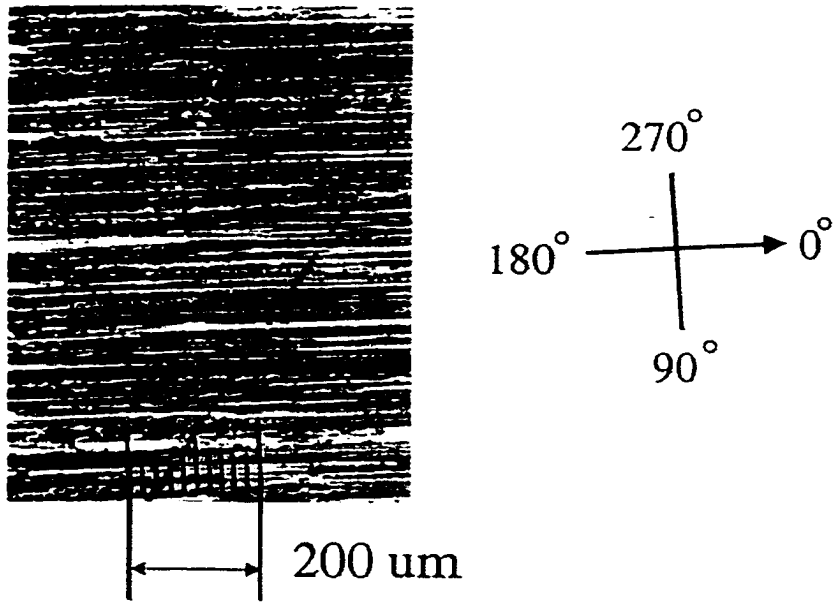

Fig. 3. The surface of Disc 2 is highly anisotropic due to the surface grinding action. This will have an effect on the Barkhausen measurements since the applied field is mostly uniaxial.

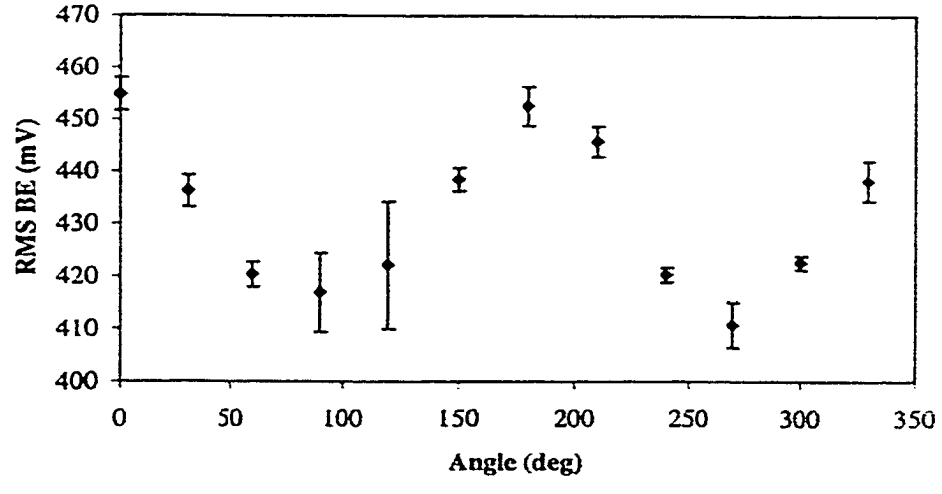

Fig. 4. The effects of surface anisotropy on the Barkhausen emission (BE) measurements of Disc 2. The RMS Barkhausen signal peaks in directions parallel to the surface grinding direction and is minimized in the perpendicular direction.

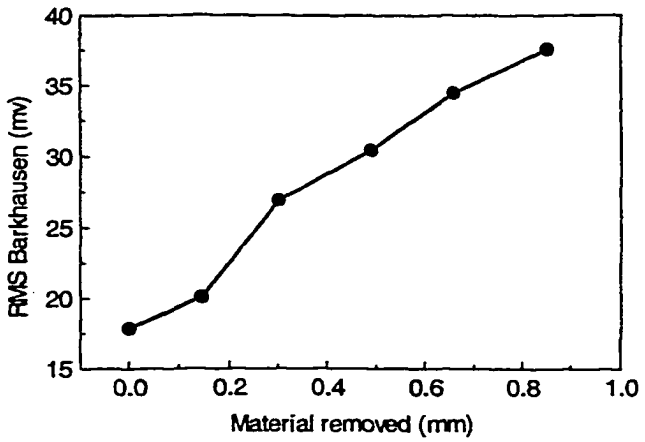

Fig. 5. RMS Barkhausen activity from Disc 2 as a function of the amount of material removed. Note that this particular experiment is not complete and significant further increases in Barkhausen activity can be expected as more material is removed.

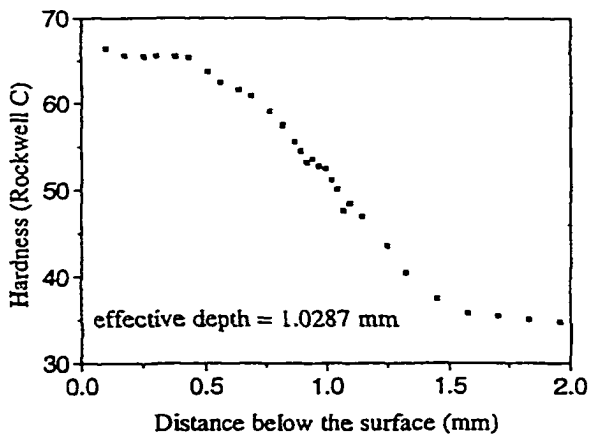

Fig. 6. Hardness profile obtained by performing a Rockwell micro-hardness traverse on a sectioned sample of Disc 2.

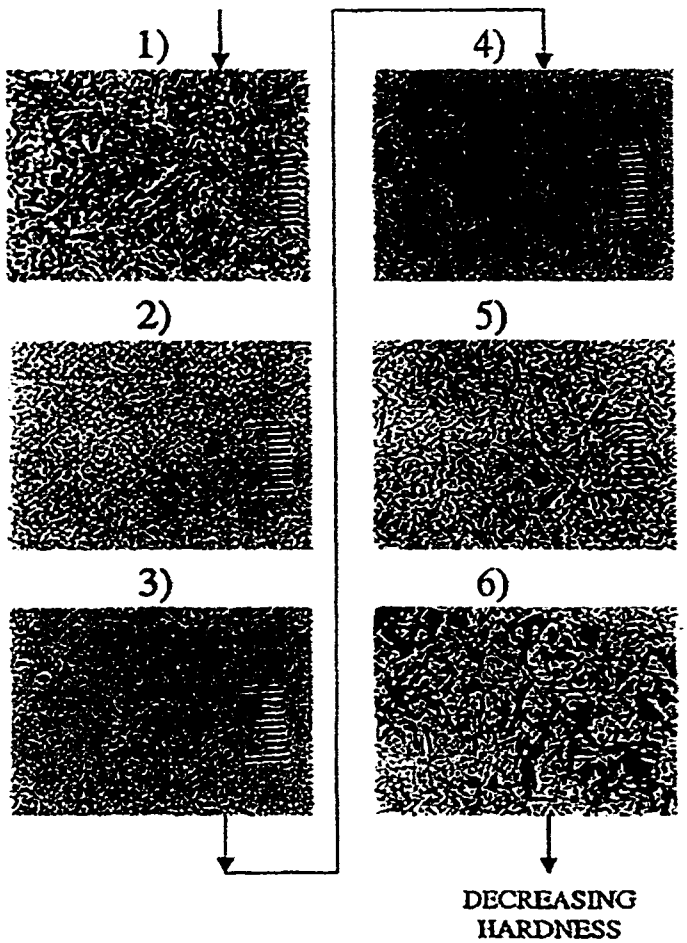

Fig. 7. Micrographs from the polished disc (Disc 1) after successive amounts of material were removed. 1, 2. Acicular martensite indicating a high carbon content. Retained austenite (white regions) are also observed. 3. Acicular martensite. The volume fraction of retained austenite is smaller than that observed in Fig. 1 and 2, showing a lower carbon content in this layer. 4,5 and 6. Mixture of acicular and lath martensites. The volume fraction of lath martensite (dark regions) is higher for a deeper layer indicating a decrease in carbon content with depth below the case-hardened surface.

4. Conclusions

Results have shown how the measurement of certain magnetic hysteresis parameters, namely the maximum differential permeability, can be used as an approximate measurement of case depth even when other microstructural variations, such as those caused by tempering, are occurring. Further work needs to be carried out to see if the same behavior is observed with samples that have been incorrectly quenched. Barkhausen and pulsed eddy-current measurements were found to

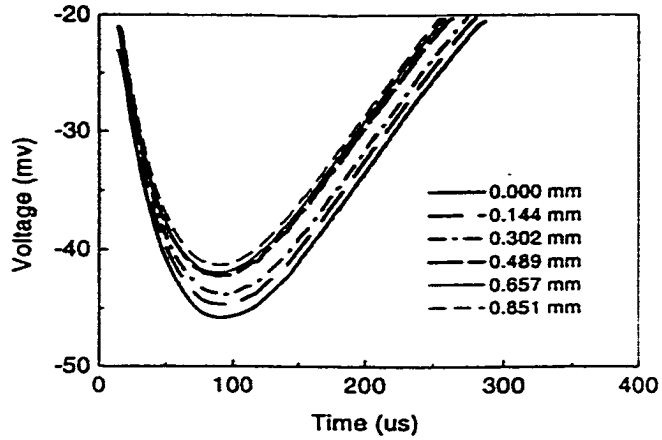

Fig. 8. Pulsed eddy-current response after surface grinding (Disc 2) The pulse amplitude decreases as material is removed and the properties of the test specimen approach those of soft steel.

correlate well with wear-induced material loss simulated by grinding. The Barkhausen measurements were highly sensitive to surface finish and some sample preparation was necessary. Pulsed eddy-current measurements on the other hard were found to be completely insensitive to surface finish. The relative sensitivity of the pulsed eddy-current technique was, however, considerably less than that of the Barkhausen approach.

Pulsed eddy-current measurements may provide the most convenient means by which to evaluate case depth, however, signal-to-noise levels must first be improved. Increasing the outer-diameter of the probe coil, which will increase eddy-current penetration depth, most easily carries this out. Because of the complex nature of the case-hardened materials, it is still not possible to describe a complete characterization system that will work under all circumstances. Further work is currently under way involving very-low frequency eddy-current measurements along with existing pulsed eddy-current and magnetic measurements techniques in order to more fully understand the materials. When this work is complete it should be possible define a working case-depth characterization system.

Acknowledgements

This work was supported by the NSF Industry/University Cooperative Research Centers Program. Samples were provided by Caterpillar, Inc.

References

[1] M. J. Johnson, H. Cao, J. C. Moulder, in Review of Progress in Quantitative NDE 18B, edited by D. O. Thompson and D. E. Chimenti, 1733 (Plenum, New York) 1999.

[2] J. H. Rose, C-C. Tai and J. C. Moulder, in Review of Progress in Quantitative NDE 16A, edited by D. O. Thompson and D. E. Chimenti, 249 (Plenum, New York) 1997.

[3] V. Moorthy, S. Vaidyanathan, T. Jayakumar and B. Raj, Philosophical Magazine A 77, 1499, 1998.

[4] J. R. Bowler and D. J. Harrison, in Review of Progress in Quantitative NDE 11A, edited by D. O. Thompson and D. E. Chimenti, 241 (Plenum, New York) 1992.

EVALUATION OF WEAR-INDUCED MATERIAL LOSS IN CASE-HARDENED STEEL

M. J. Johnson, J. Zhou, B. Zhu and N. Nakagawa
Center for Nondestructive Evaluation
Iowa State University
Ames, Iowa 50011-3042, U.S.A.

D. C. Jiles
Ames Laboratory
Iowa State University
Ames, Iowa 50011-3020, U.S.A.

INTRODUCTION

Despite the complicated microstructural conditions that can exist in steel [1], it has been demonstrated how certain magnetic and pulsed eddy-current techniques can be used for the evaluation of case depth in carburized steel samples [2]. In addition, the evaluation of wear-induced material loss in case-hardened steel has also been shown to be possible using magnetic hysteresis and pulsed eddy-current measurements. Case-hardened steels are frequently used in high-wear applications where friction between moving parts will slowly lead to erosion of the case. It is important to be able to characterize the case loss so that components can be replaced prior to failure. The challenges in determining case erosion are twofold: Firstly, the action of friction on a component will modify its near-surface microstructure, and secondly, the hardness depth profile will be different to that of a newly hardened component meaning that knowledge acquired from measurements on standard case-hardened steel samples may not necessarily apply. Despite these complications, it should be possible to determine wear-induced material loss by using magnetic and pulsed eddy-current techniques.

MEASUREMENT OF WEAR-INDUCED MATERIAL LOSS

Case-hardened components in high-load applications will slowly wear, i.e. the case-hardened layer will become eroded. If it were possible to monitor wear rates, components could be replaced in the most timely and cost-effective manner. However, there are some complications involved with this type of measurement. The frictional forces that lead to wear will modify the component's near-surface microstructure which will cause variations in the surface magnetic permeability. These permeability variations can be difficult to predict and will depend on the exact nature of wear. In addition, the shape of the hardness depth profile will vary as material is removed. Despite these complications, it should be

CP509, *Review of Progress in Quantitative Nondestructive Evaluation*, edited by D. O. Thompson and D. E. Chimenti

possible to determine wear-induced material loss by using magnetic and pulsed eddy-current techniques.

To carry out the study, two gas-carburized steel discs (referred to as Discs 1 and 2) were obtained from an industrial source. The two discs had nominal case depths, according to the Rockwell-C scale, of 1.03 mm and 1.24 mm. Material was removed from each disc by surface grinding in increments ranging from around 100 μm to nearly 300 μm. Disc 1 was also polished and etched so that micrographs could be obtained. Vickers micro-hardness indentation tests were also carried out on Disc 1. Magnetic hysteresis measurements were conducted before and after each grinding and/or polishing operation. The surface of Disc 2 was found to be highly anisotropic due to the surface grinding action, Fig. 1. The anisotropy had a strong effect on the Barkhausen measurements since the applied field was mostly uniaxial. In fact, a plot of peak RMS Barkhausen activity versus the angular position of the probe produced a near-sinusoidal response, Fig. 2. Peaks in the Barkhausen response occur at probe orientations of around 0° and 180° and correspond to directions parallel to the surface-grinding pattern. A good relationship was observed, for both Disc 1 and Disc 2, between the amount of material removed and the magnetic Barkhausen activity, Figs. 3 to 5. From the hardness profile of Disc 2, Fig. 5, it can be seen that a further 0.5 to 0.6 mm of material can be removed before the case hardened layer is completely gone. We would expect to observe further increases in Barkhausen activity down to a depth of 1.5 mm below the original surface, i.e. to a point where the exposed material becomes completely soft. This illustrates the suitability of the Barkhausen technique to monitoring wear-induced material loss. In practice, grinding damage will often occur in a single direction leading to surface anisotropy. If this direction is known and remains constant then the Barkhausen technique can be reliably applied. Fig. 6 shows the microstructure at various different depths. The hard surface is characterized by a fine microstructure (acicular martensite) containing many domain-wall pinning sites; Barkhausen activity from this region of the steel is low. A coarser microstructure, consisting of acicular and lath martensites, is found deeper below the surface; this region will give rise to relatively high levels of Barkhausen activity.

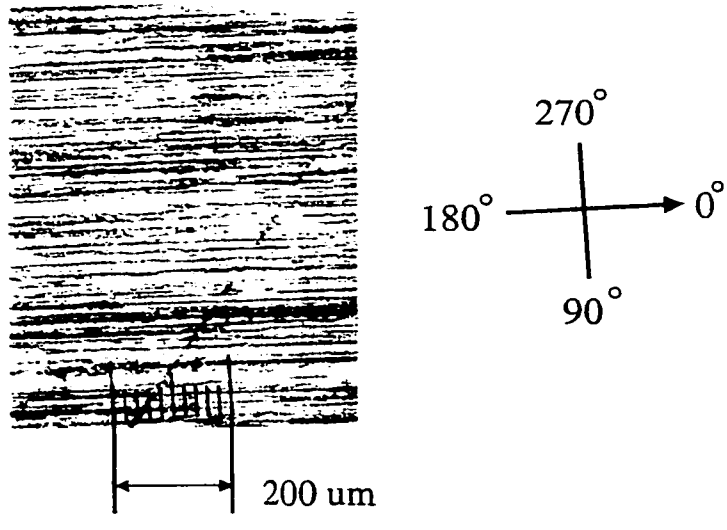

Fig. 1. The surface of Disc 2 is highly anisotropic due to the surface grinding action. This will have an effect on the Barkhausen measurements since the applied field is mostly uniaxial.

Pulsed eddy-current measurements [3] show a general trend of decreasing pulse amplitude with material loss, Fig. 7. This is because, as with regular case-depth measurements [2], a reference signal is obtained from a soft or unhardened sample. This means that the signal amplitude gets less as the properties of the measurement sample approach those of the reference sample. As material is removed from the case-hardened steel disc, the surface properties of the disc approach those of untreated steel and so the measurement pulse shape and amplitude will approach that obtained from the reference sample.

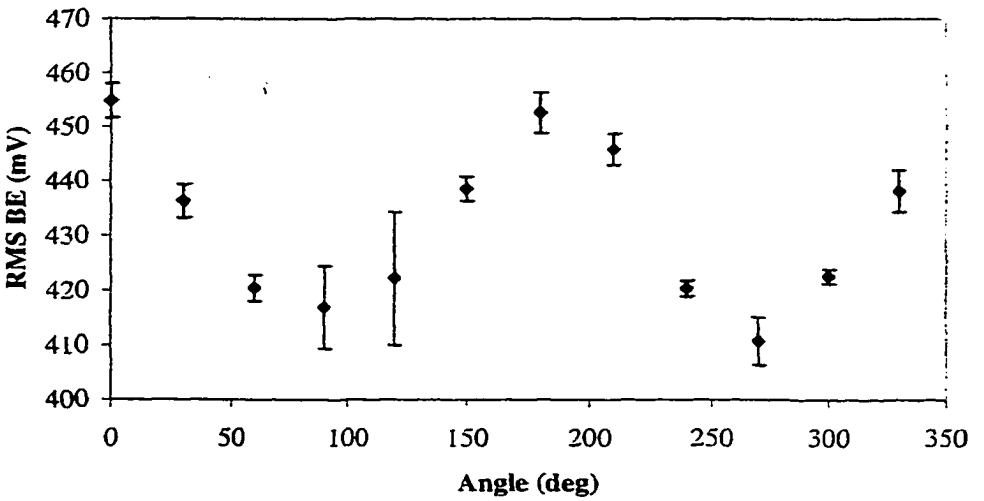

Fig. 2. The effects of surface anisotropy on the BE measurements of Disc 2. The RMS Barkhausen signal peaks in directions parallel to the surface grinding direction and is minimized in the perpendicular direction.

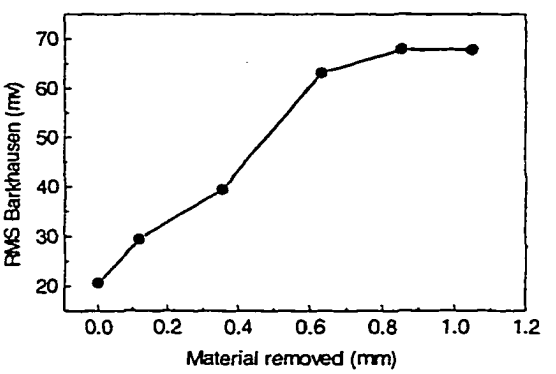

Fig. 3. RMS Barkhausen activity from Disc 1 as a function of the amount of material removed. Note that the increase in Barkhausen activity begins to taper off as the amount of material removed approaches the case depth.

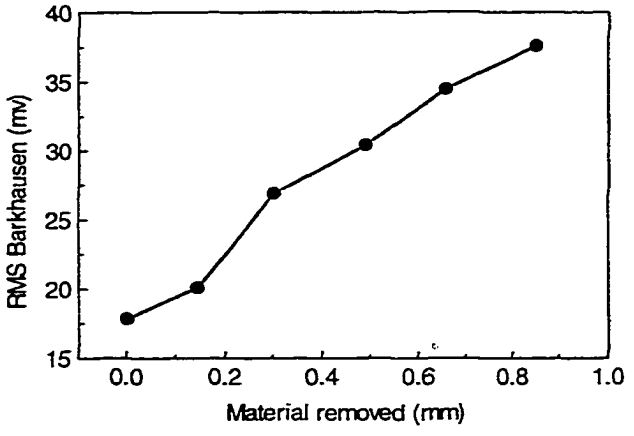

Fig. 4. RMS Barkhausen activity from Disc 2 as a function of the amount of material removed. Note that this particular experiment is not complete and significant further increases in Barkhausen activity can be expected as more material is removed.

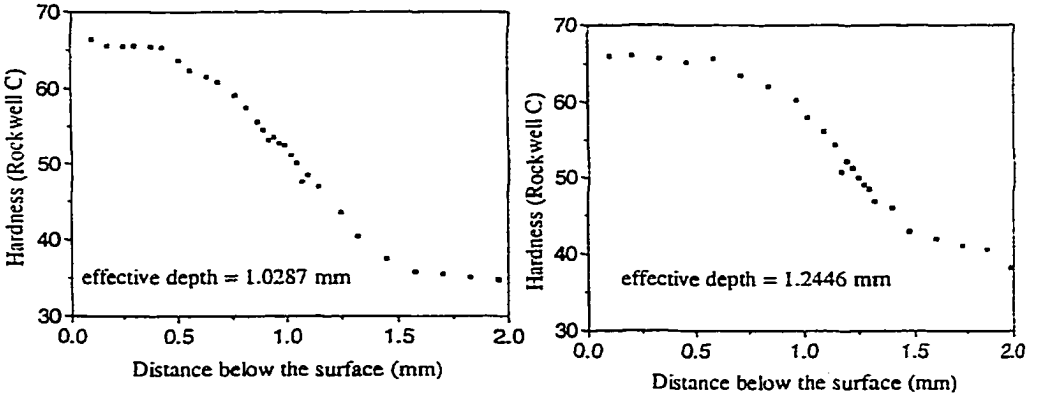

Fig. 5. Hardness profile obtained by performing a Rockwell micro-hardness traverse on a sectioned sample of Disc 1 (left) and Disc 2 (right).

CONCLUSIONS

Magnetic Barkhausen and pulsed eddy-current measurements were found to correlate well with wear-induced material loss simulated by grinding. The Barkhausen measurements were highly sensitive to surface finish and some sample preparation was necessary. Pulsed eddy-current measurements on the other hard were found to be completely insensitive to surface finish. The relative sensitivity of the pulsed eddy-current technique was, however, considerably less than that of the Barkhausen approach. It should be possible to increase pulsed eddy-current sensitivity by using a larger diameter probe coil. A larger probe coil will lead to greater eddy-current penetration and therefore improved sensitivity to deeply case-hardened samples.

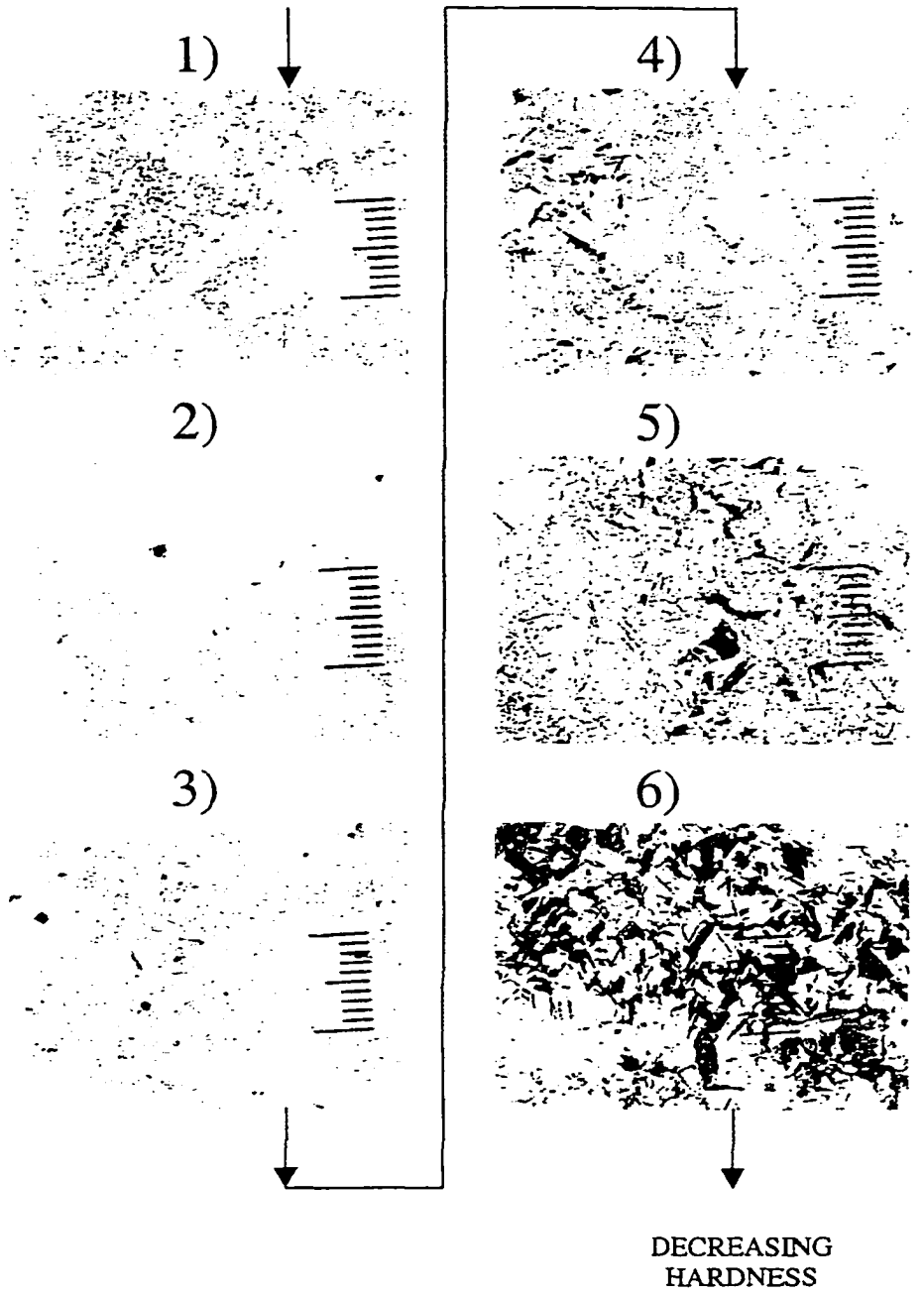

Fig. 6. Micrographs from the polished disc (Disc 1) after successive amounts of material were removed. 1, 2. Acicular martensite indicating a high carbon content. Retained austenite (white regions) are also observed. 3. Acicular martensite. The volume fraction of retained austenite is smaller than that observed in 1 and 2, showing a lower carbon content in this layer. 4,5 and 6. Mixture of acicular and lath martensites. The volume fraction of lath martensite (dark regions) is higher for a deeper layer indicating a decrease in carbon content with depth below the case-hardened surface.

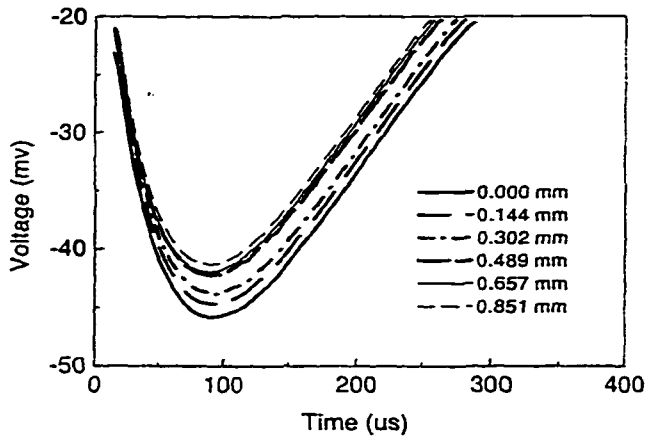

Fig. 7. Pulsed eddy-current response after surface grinding (Disc 2). The pulse amplitude decreases as material is removed and the properties of the test specimen approach those of soft steel.

ACKNOWLEDGEMENTS

This work was supported by the NSF Industry/University Cooperative Research Centers Program. Samples were provided by Caterpillar, Inc.

REFERENCES

1. M. J. Johnson, H. Cao, J. C. Moulder, in Review of Progress in Quantitative NDE, Vol. 18B, edited by D. O. Thompson and D. E. Chimenti (Plenum, New York, 1999), p.1733.
2. J. H. Rose, C-C. Tai and J. C. Moulder, in Review of Progress in Quantitative NDE, Vol. 16A, edited by D. O. Thompson and D. E. Chimenti (Plenum, New York, 1997), p. 249.
3. M. J. Johnson, J. R. Bowler, in Review of Progress in Quantitative NDE, Vol. 17, 1997.
4. J. R. Bowler and D. J. Harrison, in Review of Progress in Quantitative NDE 11A, edited by D. O. Thompson and D. E. Chimenti, 241 (Plenum, New York) 1992.

Multi-functional Magnetic Barkhausen Emission Measurement System

B.Zhu, M.J.Johnson, C.C.H.Lo and D.C.Jiles

Abstract-- **The Barkhausen effect can be used as a method for material characterization. Recently a system has been developed which can be used to make magnetic Barkhausen emission measurements and perform multi-functional analysis of the results. The organization of this system, together with the procedures incorporated into the software, allows flexible control of applied fields and multivariate analysis of the Barkhausen signal emissions.**

Index Terms—**Barkhausen effect, material characterization.**

I. Introduction

THE measurement of magnetic Barkhausen emission (BE) of materials has received little attention in the past. Nevertheless it is now becoming of increasing interest, particularly in the area of non-destructive evaluation or material assessment. It has been realized that the nature of BE is closely related to the microstructure and stress state of the materials [1,2] and therefore measurement of BE signals can be used to evaluate the microstructure or stress level of materials [3,4,5,6].

Efforts have been focused on the relationship between the BE measurement parameters such as RMS voltage or amplitude of BE signals and their dependence on the various changes in microstructure or stress. Theoretical models of BE by Bertotti *et al.* [7,8,9] and by Jiles *et al.* [10,11,12] allow various characteristics of these signals such as the variance, pulse height distribution and power spectral density to be described mathematically. This provides a basis for a more fundamental study of the phenomenon and allows the relationship between the BE characteristics and properties of materials to be studied. These advances in the theoretical studies of BE also suggest the need for further development of measurement system that can be used to measure various characteristics of BE for comparison with theoretical modeling results.

In this study a new computer-controlled system for making Barkhausen emission measurement on material has been developed, based on our previous Magneprobe system [13]. This system was designed for detection and analysis of BE signals from a material for non-destructive evaluation. The versatility of the system arises from the fact that it offers a range of analysis techniques. System developments included the hardware for generating an alternating magnetic field and detection of the BE signal, and software for instrument control and data analysis. Furthermore, this system can be used to sample BE signals at a rate of 5 MHz with a voltage resolution of 1.2 mV (14 bit, 5 V full scale). This represents a significant improvement over the previous 400 kHz, 12 bit system. The algorithms embedded in the software enable rapid collection and analysis of the BE signals measured under precisely controlled conditions. This paper describes the organization of the system and the procedures incorporated into the software which allows a flexible control and precise analysis of the Barkhausen emission.

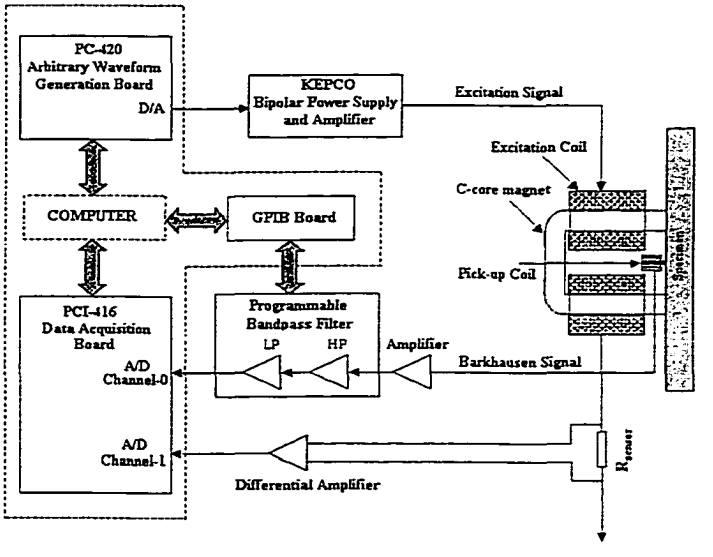

Fig. 1. Block diagram of system hardware

II. HARDWARE

A schematic diagram of the hardware configuration is shown in Fig. 1. The entire system is operated under computer control. It includes a two-channel arbitrary waveform generation (AWG) card which can generate signals at up to 10 MHz with a frequency resolution of 0.012% and an accuracy of ±0.012% of the frequency used. The signal amplitude range is 20 V peak-to-peak and the resolution is 0.05% of full scale. Seven third order Butterworth low-pass

Manuscript received January 28, 2000 This work was supported by the Center for Nondestructive Evaluation, an NSF Industry/University Cooperative Research Center at Iowa State University.

The authors are with the Center of NDE, Iowa State University, Ames, IA, 50011.

filters with different cut-off frequencies are embedded on each output channel of the AWG card to ensure high spectral purity of the excitation signal. This card can be used to produce any form of excitation signal in order to excite Barkhausen events. The excitation signal is amplified by a bipolar power supply and delivered to the excitation coil which is wound on a c-core magnet. This generates an alternating magnetic field in the c-core magnet and the sample. The BE signal detected by a pick-up coil is amplified and filtered using a high-pass filter to remove the low-frequency interference such as that coupled from the excitation coil and 60 Hz power line frequency noise. The low-pass filter then removes high-frequency noise and harmonics. The voltage gains of the filters can be adjusted to provide additional amplification of the signal. The output signal of the band-pass filter is fed into the channel-0 of a high-performance PCI data acquisition card which allows accurate sampling of the BE signals. This card has two simultaneous (14-bit, 5 MHz sampling rate) A/D channels and the input section of each channel connects to a very high speed wide-band low noise amplifier. A GPIB card is used to communicate with a programmable filter unit which has a frequency range from 1 Hz to 2 MHz. In order to obtain consistent measurement results, the voltage signal across a resistor R_{sensor} is input to the A/D channel-1 on the data acquisition card (as shown in Fig. 1) and used as the trigger signal. The system starts collecting BE data when this trigger signal passes the zero crossing point during the rising edge. It guarantees that the acquired BE signal always has the same phase relationship with the excitation current. Fig. 2 shows the relationship between the current and the Barkhausen signal obtained from a plain carbon steel sample (0.2wt% C).

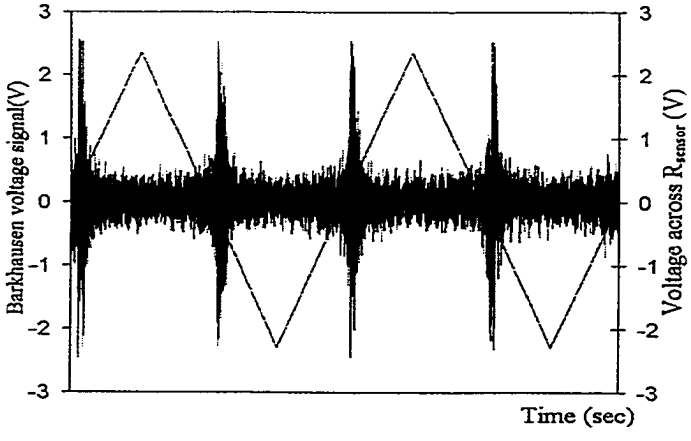

Fig. 2. Current vs Barkhausen signal

III. SOFTWARE

The unique capabilities of the Magneprobe system are derived largely from the control and data analysis software Magsoft which is a 32 bit application program written in Visual C++6.0 under the Windows 98 environment. The structure of the software is shown in Fig. 3. From the user interface, the operator can perform any function in the program. The waveform generation module allows setting the amplitude, frequency and offset of the excitation signal. The data acquisition module allows setting sampling clock rate, clock source (internal or external), number of sampling cycles, trigger rate and trigger source for the A/D card. The filter setting module is used to send GPIB commands to the filters to control the filter settings including the input and output gains, frequency range, filter mode (high-pass, low-pass, band-pass or band-reject) and filter type (Elliptical, Butterworth or Bessel).

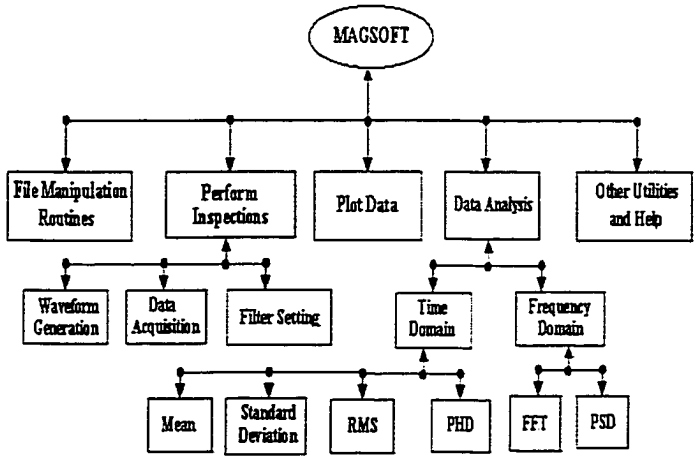

Fig. 3. Block diagram of system software hierarchy

To prepare for a measurement, the hardware needs to be set up properly first, and then the system will start collecting BE data automatically when it becomes stable. The acquired data can be analyzed by a number of algorithms including standard deviation, Root Mean Square (RMS), Fast Fourier Transform (FFT), Power Spectral Density (PSD) and Pulse Height Distribution (PHD). The results in time and frequency domains can also be displayed on the screen and then saved to data files for further analysis.

IV. EXPERIMENTAL RESULTS

The Magneprobe system has been used to study the effects of microstructure of plain carbon steel samples on BE signals. The compositions of the samples S1 and S2 that were used are listed in Table I. Both samples were found to have a ferrite/pearlite structure. The volume fraction of pearlite Vp of the samples were measured and the results are listed in Table I.

TABLE I
COMPOSITION AND MICROSTRUCTURE

Sample	Carbon content (wt%)	Volume fraction of pearlite V_p (%)
S1	0.20	17
S2	0.45	56

BE measurements were made using a 2 Hz excitation signal with triangular waveform generated by the AWG card. The lower and higher cut-off frequencies of the filters were 5 kHz and 250 kHz respectively. Voltage gains of 10dB and 40dB were used in the high-pass and low-pass filtering stages respectively. The filtered signal was sampled at 500 kHz using an internal clock. The BE signals and the corresponding RMS values measured from the samples S1 and S2 are shown in Figs. 4 and 5 respectively. It was found that S2 gave stronger BE signals with larger RMS value than S1.

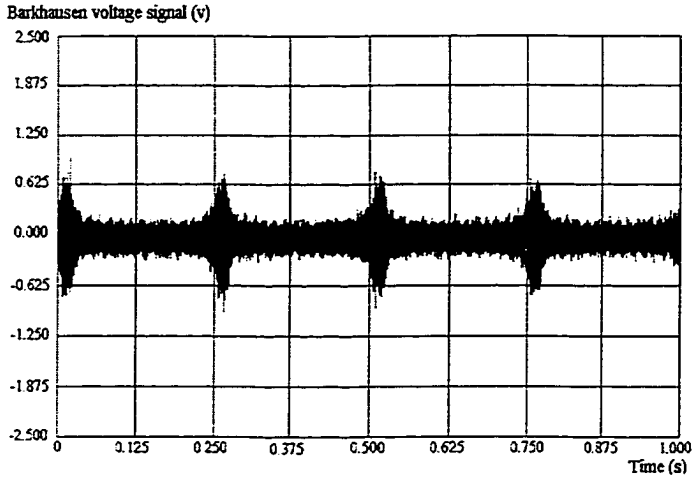

Fig. 4. Raw Barkhausen data from S1 (RMS:97mV)

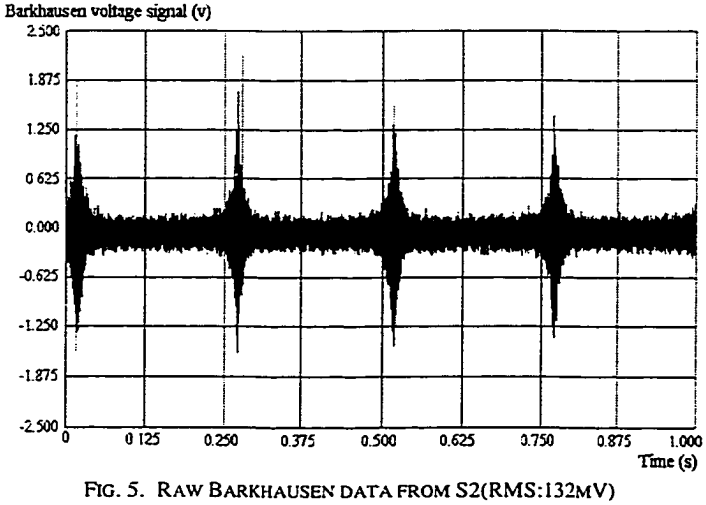

FIG. 5. RAW BARKHAUSEN DATA FROM S2(RMS:132MV)

The BE profiles of the samples, which were obtained by averaging the rectified BE signals over 300 cycles are shown in Figs. 6 and 7. The BE profiles of S1 was found to have two distinguishable peaks, while the BE profile of S2, however, shows a sharp peak at around the coercive point due to the irreversible domain wall motion [14]. The observed differences in BE profiles between these two samples suggests that the samples may have different irreversible magnetization processes during the hysteresis loop.

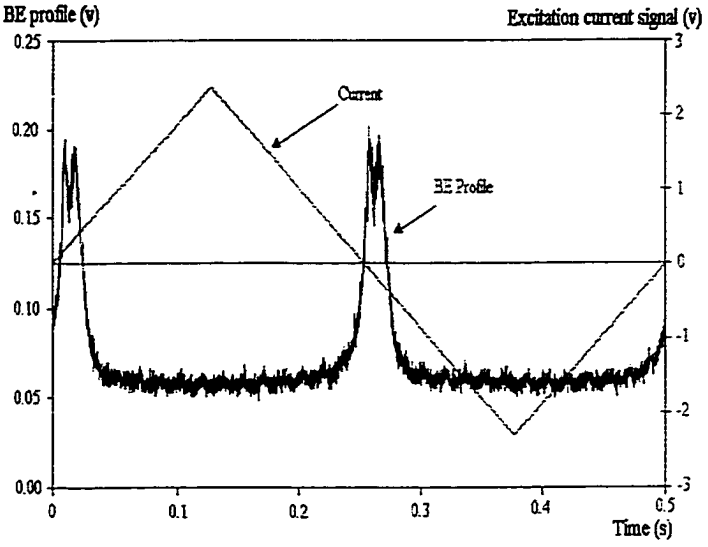

Fig. 6. BE profile over one hysteresis loop for S1

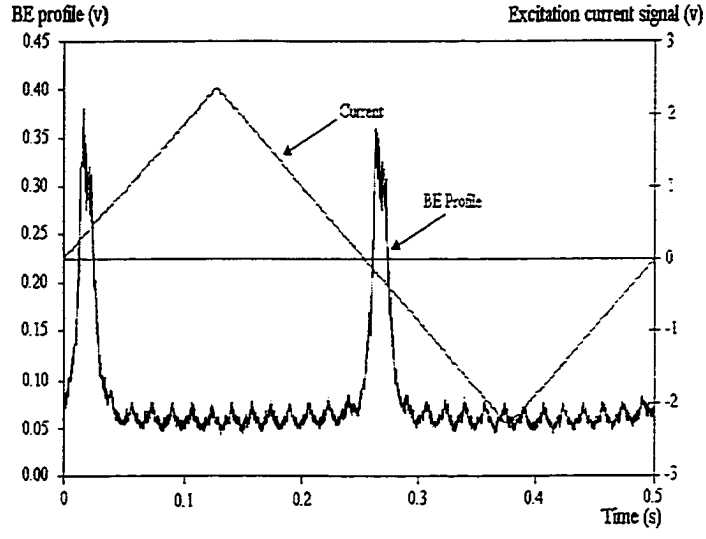

Fig. 7. BE profile over one hysteresis loop for S2

The frequency spectra (FFT) of the BE signals are shown in Figs. 8 and 9 for the samples S1 and S2 respectively. Both spectra have similar frequency components, although the spectrum obtained from S1 shows stronger Fourier components than those found in the FFT of S2. It has been shown in a recent theoretical study of BE signals that the high frequency components of PSD (and correspondingly the FFT spectrum) of BE signals diminish as the correlation length, which represents the range of interaction of domain walls with pinning sites, increases [15]. The observed difference in FFT spectrum between S1 and S2 could be caused by the difference in pinning site density between the samples. Further systematic studies are necessary to investigate how the FFT spectrum (and hence PSD) vary with the correlation length and how this parameter is related to the length scale of the pinning sites for domain walls in materials.

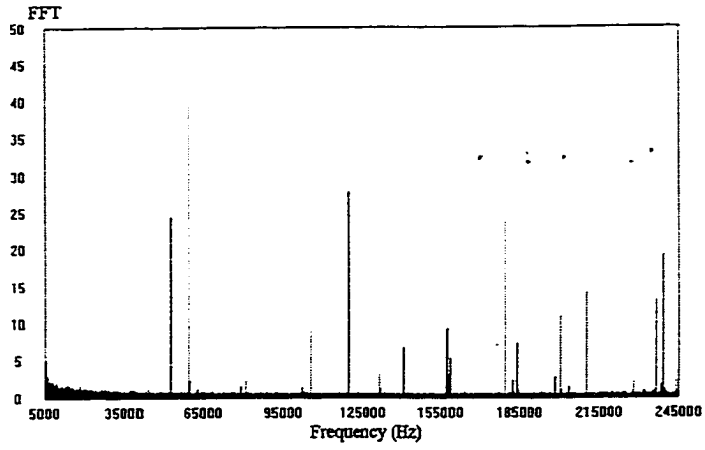

Fig. 8. Frequency spectrum of S1

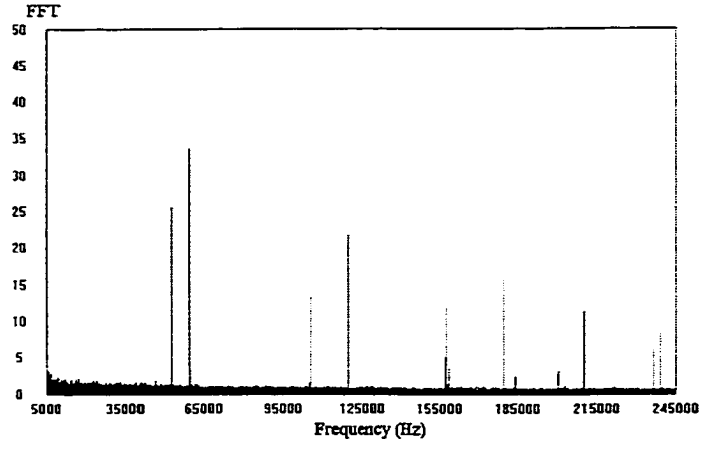

Fig. 9. Frequency spectrum of S2

The pulse height distribution (PHD) spectra of the BE signals are shown in Fig. 10. The PHD spectra are very similar in the low amplitude regime of Barkhausen pulses (up to 0.3 V). This is attributed to the dominance of the background noise in the acquired signals in this regime.This is indicated in Fig. 11 which shows the PHD of the background noise measured without applying any excitation field to the samples. Important information about the Barkhausen pulses can be extracted from the PHD spectra in the high amplitude regime (signal pulses larger than 0.2 V as indicated by "A" in Fig. 10). As Fig. 12 shows, PHD spectrum of the BE signals of S2 displays a longer tail extending to large pulse heights than that of S1. The present results are consistent with the results obtained in a previous study of BE signals in plain carbon steels with different pearlite contents [16], and can be explained in terms of the difference in pearlite content between the samples. A Barkhausen event, or pulse, can be interpreted as individual or collective jumps of domain walls as they overcome pinning sites. The larger the jump following unpinning, the larger the voltage change corresponding to that jump. It has been shown that cementite lamellae in pearlites are strong pinning sites for domain walls [17]. Therefore the domain walls in S2, which has higher pearlite content, experience stronger pinning force. During the hysteresis cycle, once the local fields acting on the domain walls in S2 overcome the pinning forces these domain walls can jump further than those in S1 before they become pinned again. This gives rise to stronger Barkhausen pulses in S2 than in S1, and thus accounts for the wider range of BE jump size in S2 than in S1.

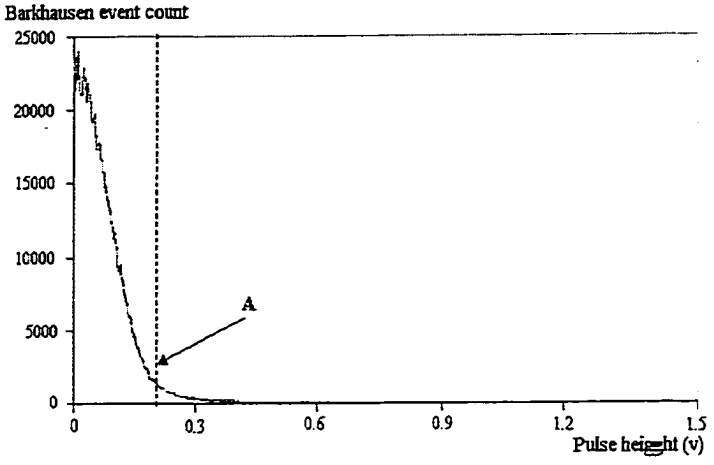

Fig. 10. Pulse height distribution of BE signals

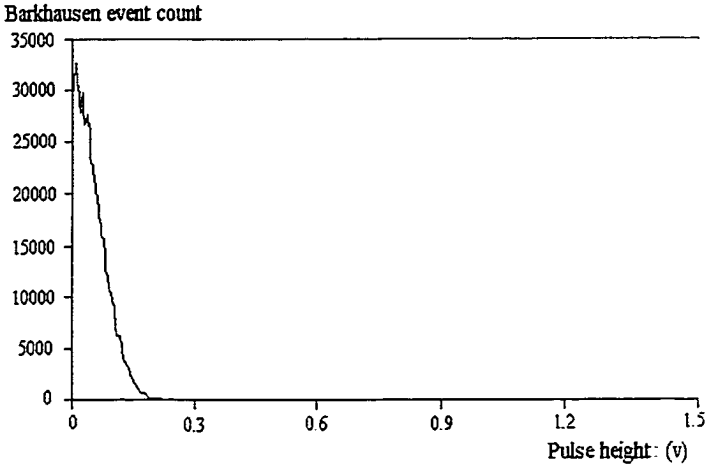

Fig. 11. Pulse height distribution of background

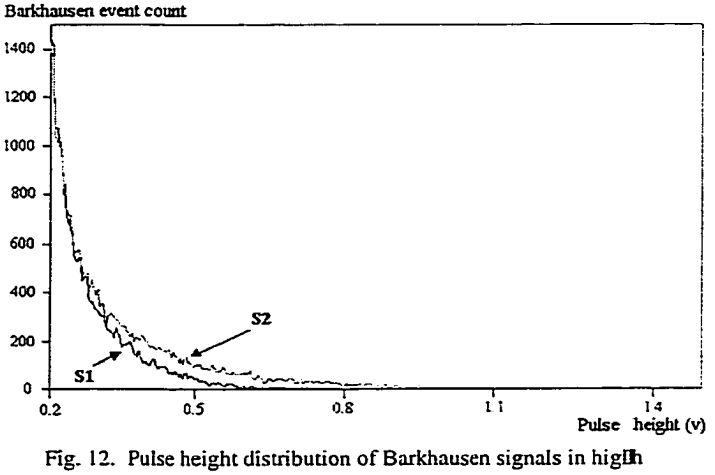

Fig. 12. Pulse height distribution of Barkhausen signals in high amplitude range

V. CONCLUSION

A new multi-functional system for measurement of Barkhausen emission has been developed. This system provides the capability for making a range of Barkhausen emission measurements and analyzing the results in a variety of ways. The measurements can be made easily and rapidly through the use of system software. The various inspection procedures contained in the software make the system very flexible, and since they are in software, new procedures can be easily added, allowing evolution of the instrument to meet new needs.

VI. REFERENCES

[1] G.A.Matzkanin, R.E.Beissner and C.M.Teller, SWRI Report, No.NTIAC-79-2,1979.

[2] Report, No.NTIAC-79-2, 1979.

[3] D.C.Jiles, NDT International, vol. 21, pp. 311, 1988.

[4] M.J.Johnson, J.Zhou, N.Nakagawa, D.C.Jiles and B.Zhu, Electromagnetic Nondestructive Evaluation (IV), edited by S.S.Udpa *et al*, pp.127, IOS Press, 2000

[5] W.A.Theiner, and I.Alpeter, New procedures in nondestructive testing: proceedings of the Germany-U.S.workshop, edited by P.Höller, Springer-Verlag, New York, 1983.

[6] W.A.Theiner, I.Alpeter and R.Kern, Nondestructive Characterization of Materials II, edited by J.F.Bussiere, Plenum Press, New York, 1986.

[7] L.Clapham, T.W.Krause, H.Olsen, B.Ma, D.L.Atherton, P.Clark and T.M. Holden, Nondestructive Testing and Evaluation International, vol. 28, pp. 73, 1995.

[8] G. Bertotti, IEEE Transactions on Magnetics, vol. 24, pp. 621, 1988.

[9] B. Alessandro, C.Beatrice, G.Bertotti, and A.Montorsi, Journal of Applied Physics, vol. 68, pp. 2901, 1990.

[10] B. Alessandro, C.Beatrice, G.Bertotti, and A.Montorsi, Journal of Applied Physics, vol. 68, pp. 2908, 1990.

[11] D.C.Jiles, L.B.Sipahi and G. Williams, Journal of Applied Physics, vol. 75, pp. 5380, 1993.

[12] D.C.Jiles and L.Suominen, IEEE Transactions on Magnetics, vol. 30, pp.4924, 1994.

[13] A.Mitra, L.B.Sipahi, M.R.Govindaraju and D.C.Jiles, Journal of Magnetism and Magnetic Materials, vol. 153, pp. 231, 1995.

[14] A.P.Parakka and D.C.Jiles, Journal of Magnetism and Magnetic Materials, vol. 140-144, pp. 1841, 1995.

[15] D.C.Jiles, Czech Journal of Physics, vol. 50, no.8, pp. 893, 2000.

[16] D.M.Clatterback, V.J. Garcia, M.J.Johnson and D.C.Jiles, submitted to the Journal of Applied Physics.

[17] L.Clapham, C.Jagadish and D.L.Atherton, , Acta metallurgica et materialia, vol.39, no.7, pp.1555, 1991.

[18] M.G. Hetherington and J.P. Jakubovics, JA. Szpunar ad B.K. Tanner, Philosophical magazine B, vol. 56, pp. 561, 1987.

Evaluation of Wear-induced Material Loss in Case-Hardened Steel Using Magnetic Barkhausen Emission Measurement

B.Zhu, M.J.Johnson and D.C.Jiles
Center for NDE, Iowa State University, Ames, IA 50011

Abstract—**The feasibility of using magnetic Barkhausen emission (MBE) measurement for the evaluation of wear-induced material loss in case-hardened steel is discussed in this paper. MBE measurements were carried out on two gas-carburized steel discs and material was removed from each disc by surface grinding. It has been observed that the MBE level increases with more material removed. This suggests that the MBE measurements would help in monitoring wear-induced material loss.**

Index Terms— **Case hardened, material loss, MBE**

I. INTRODUCTION

Case-hardened components are frequently used in high wear applications where friction between moving parts will slowly lead to erosion of the case. Hence, if it were possible to monitor wear rates, components could be replaced in the most timely and cost-effective manner.

The magnetic Barkhausen emission (MBE) phenomenon is found in ferromagnetic materials which is attributed to the irreversible movement of magnetic domain walls overcoming the obstacles in their path during magnetization. For case-hardened steels, the carbon content increases the number of defects or pinning sites and hence improve hardness. These pinning sites also change the behavior of domain walls and thus the MBE level, and therefore measurement of MBE signals can be used for evaluation of case depth on surface modified steels[1][2].

It is known that during carburization, the concentration gradient below the carburized surface and the depth of carburization vary continuously with exposure time. The subsurface carbon concentration strongly influences the hardness and the MBE level. Thus, surface MBE measurement can be related to the changes in the subsurface carbon concentration and hence, with appropriate calibration, the depth of material loss can be estimated.

II. EXPRRIMENTAL PROCEDURE

To carry out the study, two gas-carburized steel discs (Disc 1 and 2) were used. The two discs have nominal case depths of 1.03mm and 1.24mm respectively. Material was removed from each disc by surface grinding in increments ranging from around 100um to nearly 300um.Disk1 was also polished in order to remove the surface anisotropy. Vicker's hardness tests were also carried out on Disc 1.

The surface of Disc2 was found to be highly anisotropic due to the surface grinding action. The anisotropy had a strong effect on the Barkhausen measurement since the applied field was mostly uniaxial. A plot of peak RMS Barkhausen activity versus the angular position of the probe produced a near sinusoidal response as shown in Fig.1. Peaks in the Barkhausen response occur at probe orientations of around 0° and 180° and correspond to directions parallel to the surface-grinding pattern.

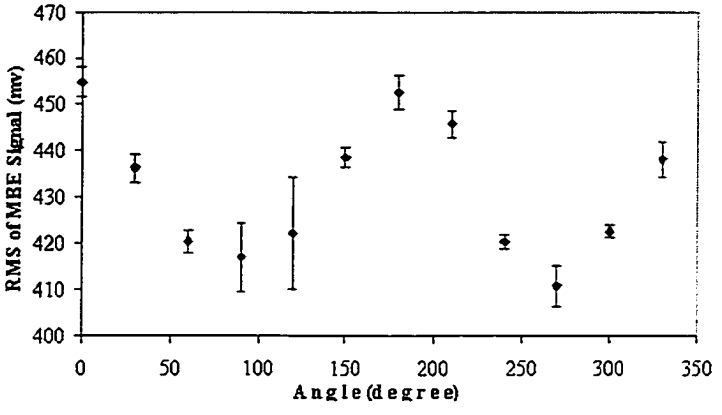

Fig.1. The RMS of MBE signal versus angular position of the probe

The Barkhausen signal was picked up by our computer-controlled MBE measurement system – Magneprobe[3]. Its system diagram is shown in Fig.2.

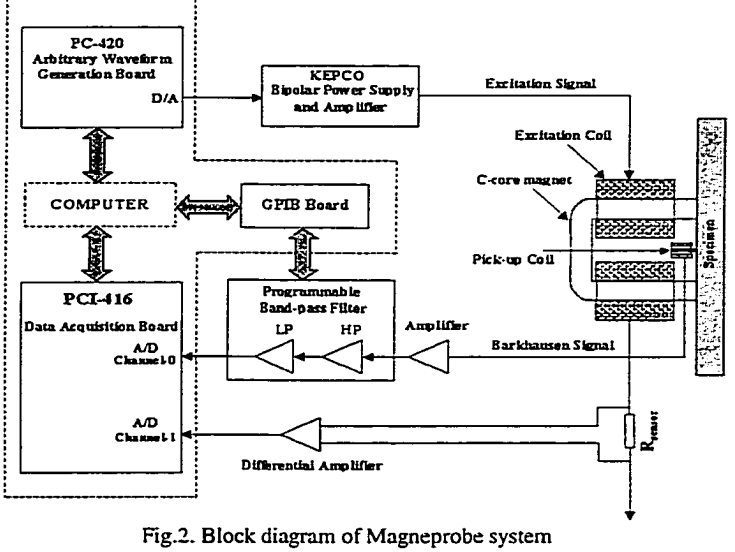

Fig.2. Block diagram of Magneprobe system

Manuscript received February 14,2000. This work was supported by the NSF Industry/University Cooperative Research Program.

B.Zhu, M.J.Johnson and D.C.Jiles, 515-294-4140, e-mail: binzhu@iastate.edu, marcusj@iastate.edu, gauss@ameslab.gov

III. RESULTS AND DISCUSSION

A good relationship was observed, for both Disc 1 and Disc 2, between the amount of material removed and the magnetic Barkhausen activity as shown in Fig.3 and 4. This illustrates the suitability of the MBE measurement to monitor wear-induced material loss. In practice, grinding damage will often occur in a single direction leading to surface anisotropy. If this direction is known and remains constant then the MBE measurement can be reliably applied.

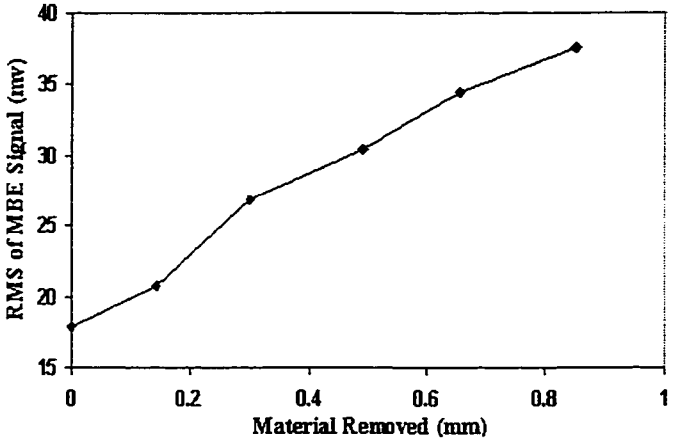

Fig.3. RMS of MBE signal from Disc 1 as a function of the amount of material removed.

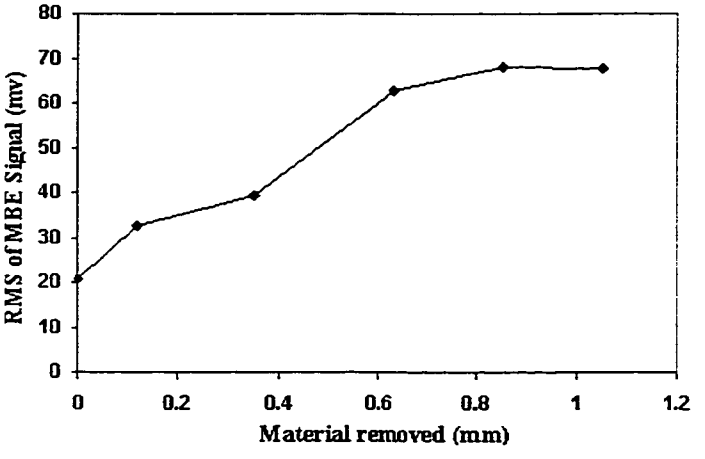

Fig.4. RMS of MBE signal from Disc 2 as a function of the amount of material removed.

Figure 5 shows the relationship between the amount of the material removed and the surface hardness. The vicker hardness decreases with more material removed due to the decrease in carbon content.

It is known the MBE signal is affected by grain boundaries, carbides, inclusions, dislocations, etc. The individual effects could be distinguished, however, only under certain conditions. In case of carburization, the extensive carbide precipitation due to carbon diffusion would dominate the micro-structural variation and would strongly influence the hardness. The carbide precipitates pin the domain walls and increase the critical field to overcome this resistance. And the net effect is the increase in the RMS of MBE signal with decrease in the carbon content. Furthermore, it has been shown that in the uncarburized region, the MBE signal would remain constant[4].

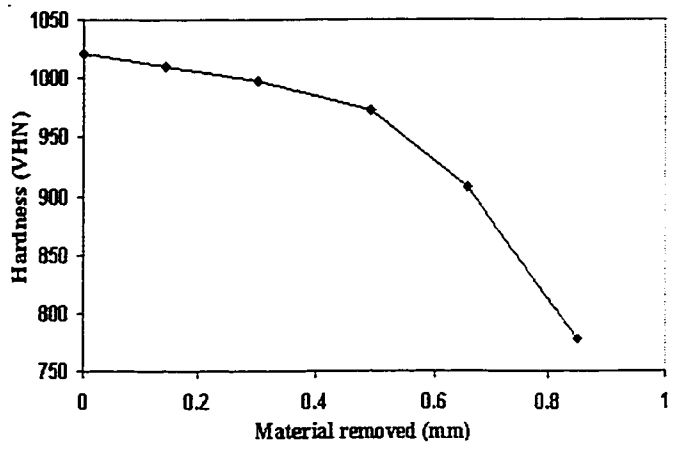

Fig.5. Vicker's hardness value of Disc 1 as a function of material removed

IV. CONCLUSIONS

This study shows that MBE signal varies with the amount of the material removed. This suggests that magnetic Barkhausen measurement can be used to monitor the wear-induced material loss in case-hardened steel.

V. REFERENCES

[1] G.Bach, K.Goebbels and W.A.Theiner, "Characterization of hardening depth using Barkhausen noise measurement", *Materials Evaluation*, vol.46, pp.1576-1580, 1988.

[2] M.Dubois and M.Fiest, "Evaluation of case depth on steels by Barkhausen noise measurement", *Materials Science and Technology*, vol.11, pp.264-267,1995.

[3] B.Zhu, M.J.Johnson, C.C.Lo and D.C.Jiles, "Multi-functional magnetic Barkhausen emission measurement system", submitted to *IEEE Trans.Magn.*

[4] S.Vaidyanathan, V.Moorthy, T.Jayakumar and B.Raj, "Evaluation of carburization depth in service exposed ferritic steel using magnetic Barkhausen noise analysis", *Materials Evaluation*, pp. 449-452, 1998

THE EFFECTS OF AGING TIME AND TEMPERATURE ON THE MAGNETIC PROPERTIES OF NICKEL ALLOYS

M. J. Johnson[1], B. Zhu[1], C. C. H. Lo[1], D. C. Jiles[1] and R. E. Shannon[2]

[1]Center for Nondestructive Evaluation, Iowa State University, Ames, IA 50011

[2]Siemens Westinghouse Power Corporation, 1310 Beulah Road, Pittsburgh, PA 15235

Abstract. The development of NDE tools for the detection of creep and fatigue damage in nickel alloys must be preceded by a more fundamental understanding of the changes occurring during creep in these materials. Metallurgical phase changes can occur during the normal operating life of a component due to the effects of aging and high temperatures; these changes, and their effect on NDE measurements, must be determined. We have conducted vibrating-sample magnetometer (VSM) experiments on Inconel 738 samples that were aged between 100 hours and 3200 hours at temperatures between 732°C and 954°C.

INTRODUCTION

Market trends toward selling large industrial gas turbines with long-term programs for maintenance and parts replacement drive the need for extending service life. This program establishes the basis for nondestructive material evaluation to determine remaining life of blade materials. This investigation is part of an integrated program to advance NDE technologies to improve gas-turbine service life. The overall objectives are to identify material damage accumulation in hot section components, especially blades, and assess the feasibility of using NDE techniques to relate these characteristics to remaining life.

One material of common interest is Inconel 738, nominally a paramagnetic nickel alloy. Some areas of interest include the evolution of microstructure at elevated temperatures as well as the study of creep and fatigue damage [1]. The difficulties involved with this kind of study are substantial; the work presented here forms a foundation for further investigation. In order to address the question of how NDE may be used for assessment of remaining lifetime we must first look at some more fundamental issues. More specifically, we have investigated changes in microstructure and how these relate to magnetic measurements as a result of exposure to elevated temperatures for long periods of time. At this stage the samples have not been exposed to mechanical work.

The measurements have been carried out using highly sensitive, laboratory-based measurement equipment that is not particularly suitable for field NDE measurements. At the end of the paper we comment on possible designs for a portable measurement system capable of similar sensitivity.

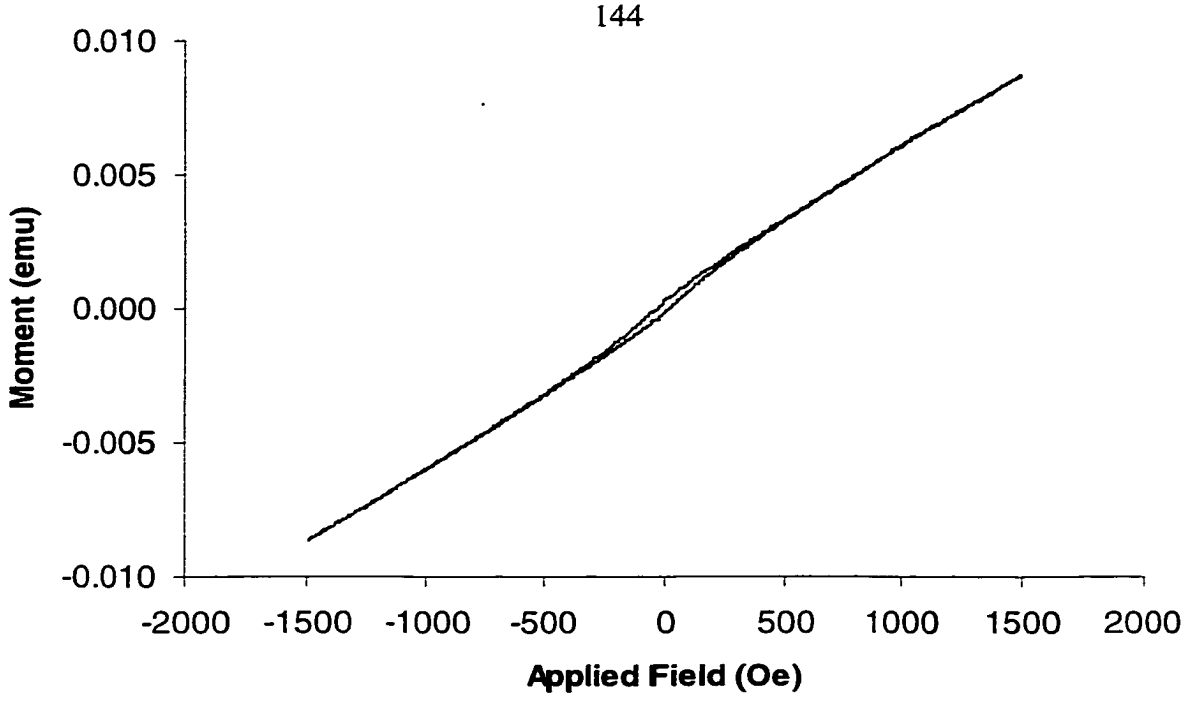

Figure 1. Magnetization curve for a typical Inconel sample obtained using the vibrating-sample magnetometer. The loop appears to vary linearly with applied field at higher induction levels.

EXPERIMENTAL MEASUREMENTS

A number of Inconel blocks were obtained and placed in an aging-furnace at temperatures between 732°C and 954°C for periods of time ranging from 100 to 3200 hours. Once complete, cubes of material approximately 30 mm^3 in volume were cut from the time-temperature aged specimens using electric-discharge machining (EDM) .

Inconel 738 is nominally a paramagnetic material and any time-, temperature– or creep-induced phase changes are unlikely to lead to significant ferromagnetic behavior. For this reason a highly sensitive method is required to characterize the magnetic properties of the Inconel. Such a high sensitivity is available from the vibrating-sample magnetometer (VSM) [2]. The VSM moves a sample in and out of a coil within a high-field region between the poles of an electromagnet. This provides a measure of the difference in induction, $\Delta\mathbf{B}$, between the coil in air and the coil surrounding the magnetized sample. The technique gives a direct measure of the magnetization, **M**, of the sample. The VSM allows magnetization to be measured with sensitivity down to 5×10^{-3} A/m (5×10^{-6} emu/cc) [3]. This compares with the saturation magnetization of iron or steel of 1.7×10^{6} A/m, meaning that the system can detect typically down to one billionth of the saturation magnetic moment per unit volume of iron or steel.

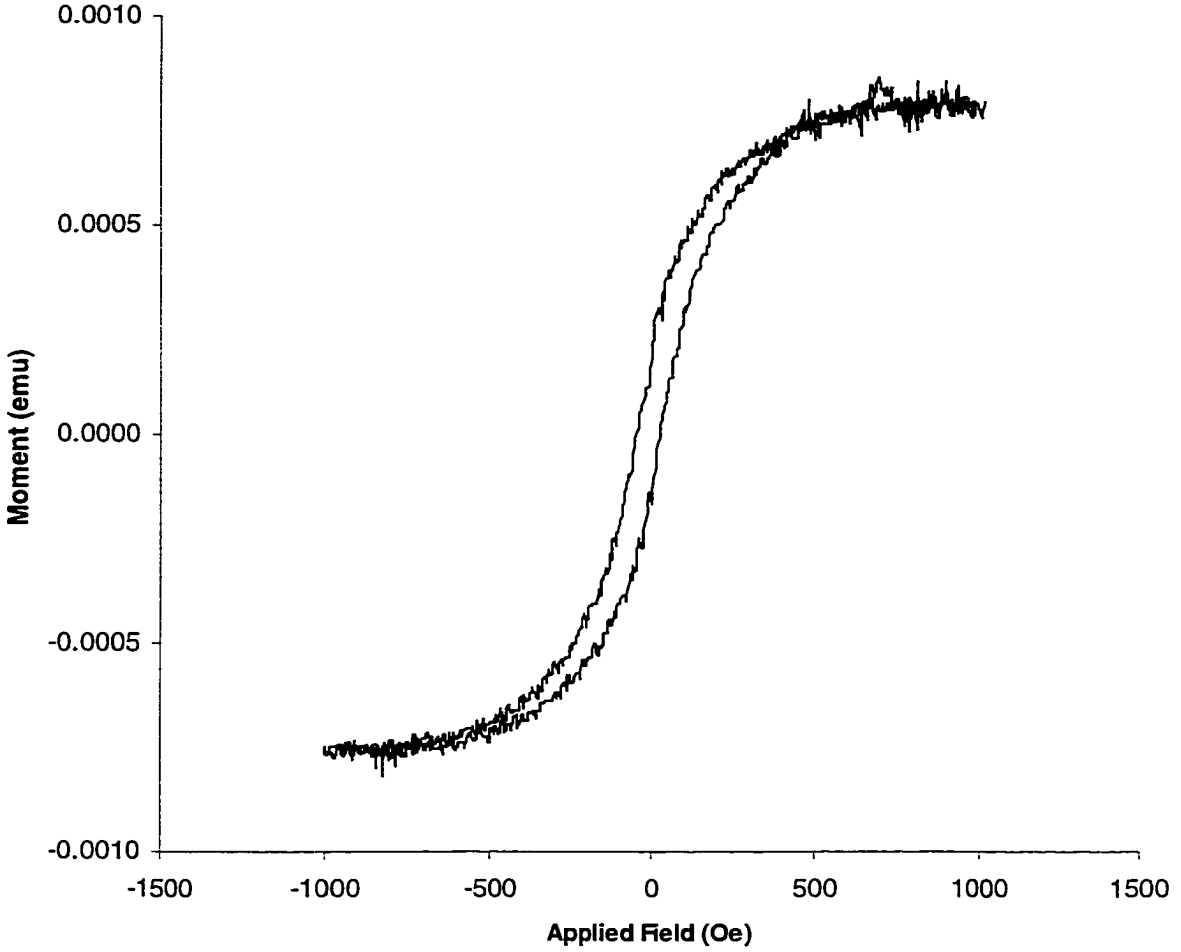

Figure 2. The paramagnetic component has been subtracted to leave the familiar hysteresis curve. Values for coercivity, core loss and remanence etc. can now be obtained.

The measured magnetization curves, Fig. 1 for example, consist of the combined effects of a ferromagnetic and paramagnetic response. Normally, when looking at ferromagnetic materials such as steel, the paramagnetic response is insignificant. However, Inconel has only a very small ferromagnetic moment, which is comparable in magnitude to that due to the paramagnetism. The paramagnetic response, $\mathbf{M_p}$, is linear with applied field while the ferromagnetic response saturates at around 500 Oe. The two terms combine to give the total magnetization,

$$\mathbf{M} = \mathbf{M_p} + \mathbf{M_s}. \tag{1}$$

It is possible to separate the two components making up **M** by looking at the signal well past the saturation point of $\mathbf{M_s}$. This is achieved by calculating the gradient at the loop tips and subtracting from **M** a linear fit based on the two values. The hysteresis loop is then replotted as shown in Fig. 2, and exhibits the more familiar hysteretic behavior.

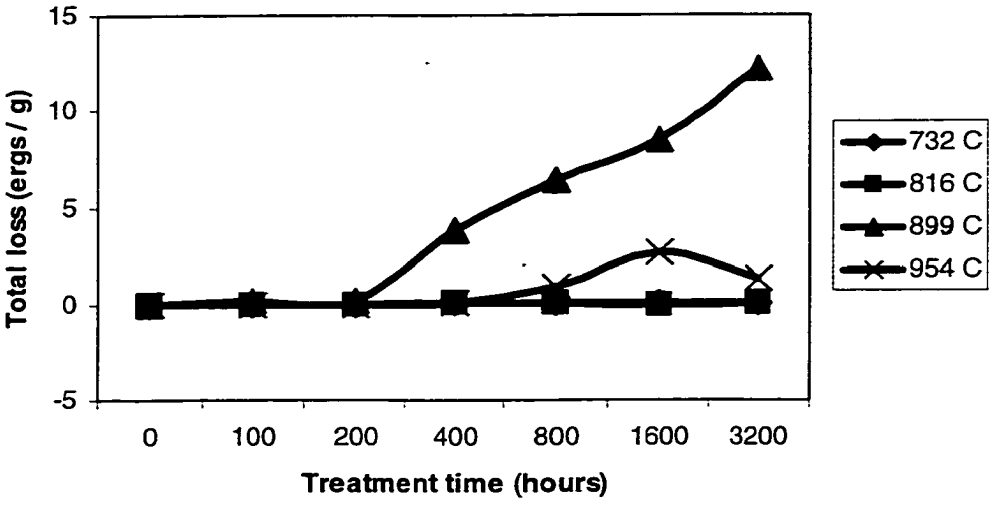

Figure 3. VSM results showing coercivity as a function of treatment time and temperature. Results show a sharp rise in ferromagnetic behavior (evident from an increase in loss) for the 899°C sample at around 400 hours. Ferromagnetic activity appears to decrease with the 954°C sample.

The above procedure was carried out on the time-temperature aged Inconel samples. After subtraction of the paramagnetic component it was possible to calculate some standard hysteresis parameters from the curves. In this study, the total loss and coercivity were calculated and were found to vary systematically with aging time, aging temperature and the changes in structure of the materials as determined from micrographs and SEM pictures.

RESULTS AND INTERPRETATION

VSM measurements of the total loss and susceptibility are given in Figs. 3 and 4. From both of these sets of results we can make a number of observations. 1) There are no ferromagnetic phases present (or their volume fractions were too small to detect) in the 732°C or 816°C samples over the entire range of treatment times. 2) The 899°C sample develops a fairly strong ferromagnetic phase after 400 hours of annealing. This phase continues to grow rapidly up until around 1000 hours at which point growth continues steadily but somewhat more slowly. 3) At 954°C the ferromagnetic phase is weaker and develops more slowly. There is some evidence that the phase diminishes after very long treatment times.

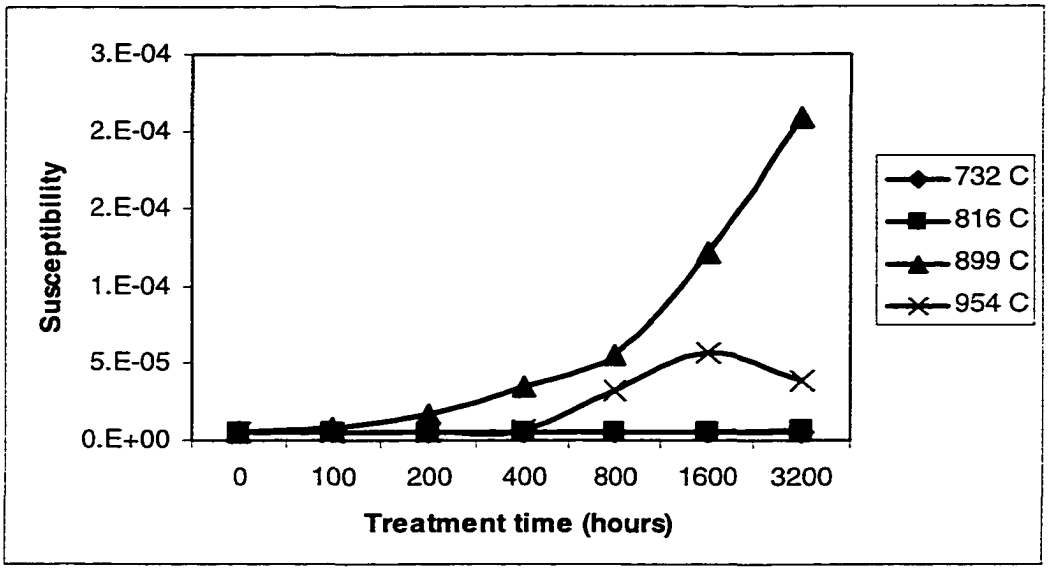

Figure 4. VSM results showing susceptibility as a function of treatment time and temperature. Results show a sharp rise in ferromagnetic behavior (evident from an increase in susceptibility) for the 899°C sample at around 400 hours. Ferromagnetic activity appears to decrease with the 954°C sample.

Clearly a ferromagnetic phase begins to form after extended periods at elevated temperatures although the effect seems to diminish at higher temperatures and after long times. This behavior could provide the key to magnetic NDE measurements for evaluation of remaining lifetime as the effects of aging should precede creep or fatigue damage. Before any further work can be carried out, the microstructural conditions that lead to these signal variations must be determined, for this purpose a set of micrographs were produced, as shown in Fig. 5.

The micrographs in Fig. 5 represent the Inconel sample that was aged at 899°C. After 400 hours there is some weak evidence of the needle-like phases beginning to form. The phases are more pronounced after 800 hours and almost dominate the image after 1600 hours. Growth of the needle-like phase corresponds well with changes in total loss (Fig. 3) and susceptibility (Fig. 4). This indicates that the needle-like phase is ferromagnetic. Micrographs taken from the sample aged at 954°C show considerably less evidence of the ferromagnetic phase. Once again, this result correlates well with the magnetic measurements.

In order to aid identification of the new phase, a microprobe analysis was carried out. The top left image in Fig. 6 shows a composite image of the specimen where the needle-likes phases that are responsible for the hysteretic behavior show up very clearly. There were strong signals characteristic of nickel and titanium. In Fig. 6 (Bottom) the microprobe analysis detected both niobium and zirconium. Using this information it has been possible to eliminate a number possible phases for our list of candidates. As shown in Table 1 we are left with a list of three possibilities for the unknown needle-like phase. At this time we are still investigating the true chemical composition of this phase.

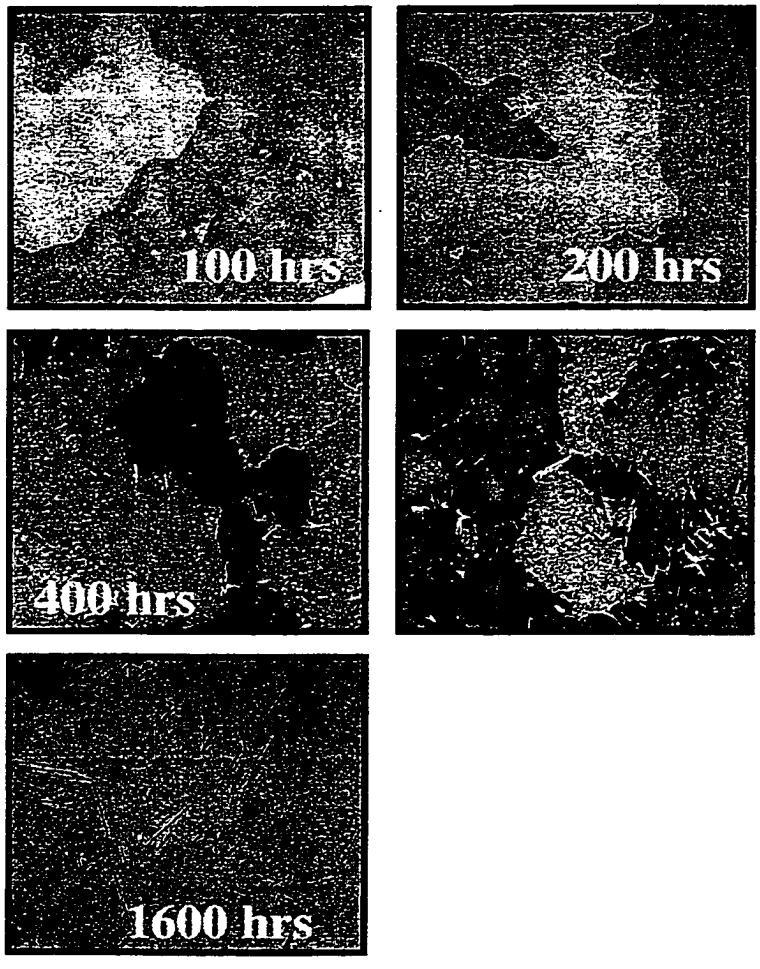

Figure 5. Optical micrographs (magnification x 100) showing the evolution of needle-like phase in Inconel at 899°C. These phases are thought to be ferromagnetic and therefore responsible for the variations in VSM measurements that were observed.

CONCLUSIONS

We have found that the magnetic properties of Inconel 738 change quite significantly at elevated temperatures during the aging process. The change involves a transition from paramagnetic to ferromagnetic behavior at 899°C after about 400 hours. Magnetic measurements indicate the presence of ferromagnetism, for example core-loss increases with time. The rate of increase tails off after about 1000 hours. Micrographs clearly show the evolution of a needle-like phase that coincides with the appearance of ferromagnetism. In addition, microprobe analysis confirms the presence of a new phase. Interestingly, the 954°C sample shows less magnetic response indicating that this higher temperature is not preferred by the new phase. Also, micrographs of these samples show considerably less evidence of the needle structure. There is a link between time and temperature that means that the needle phase could actually appear at lower temperatures given enough time. After an analysis of the results the new phase was suspected to be either Laves, Eta or Delta. Studies are continuing to identify this phase.

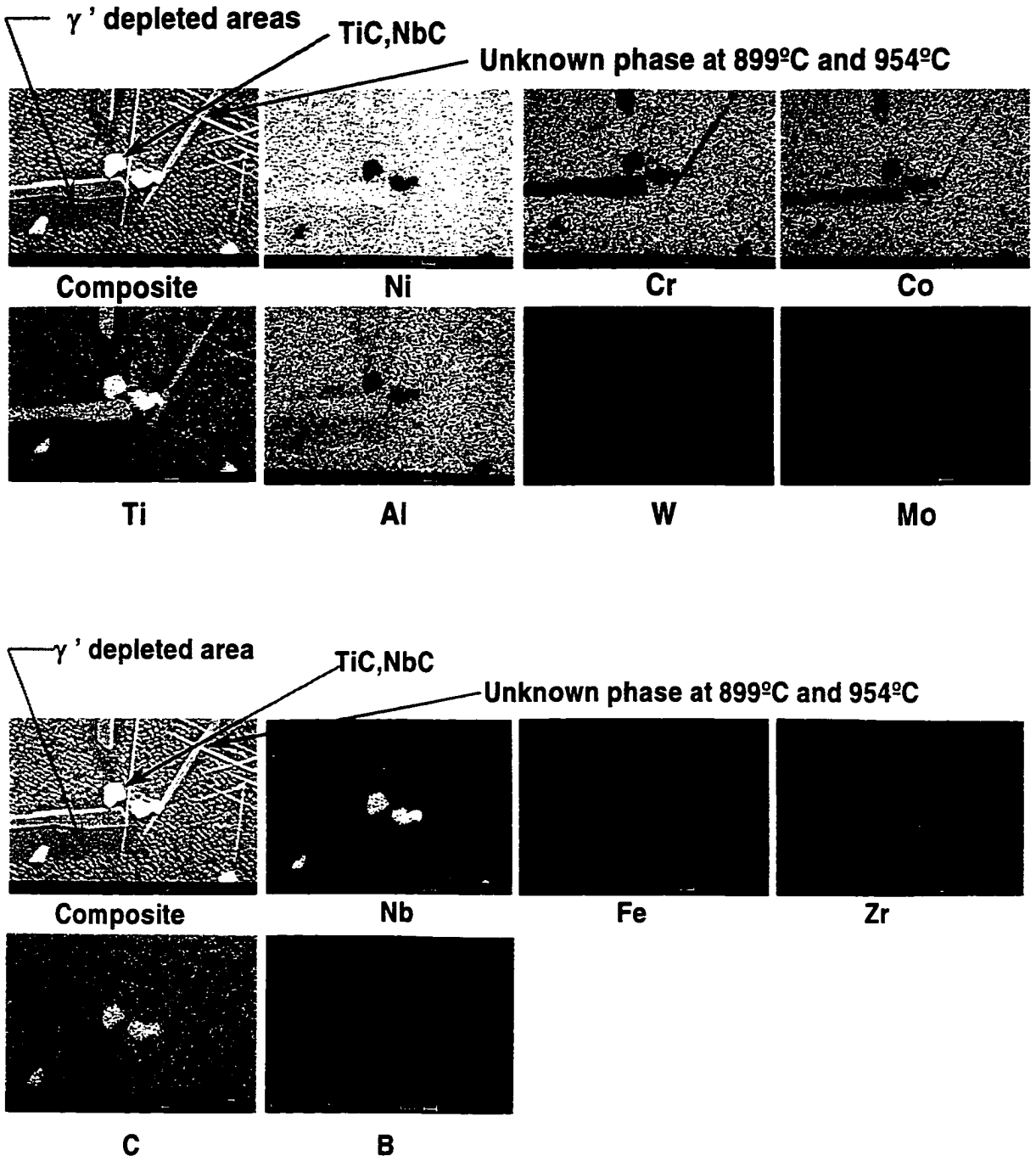

Figure 6. Electron microprobe analysis on Inconel sample aged at 899°C for 1600 hours. Top: The composite image clearly shows the needle-like phase thought to be responsible for increased ferromagnetic activity. There are strong nickel and titanium signals. Bottom: There are strong Niobium and Zirconium signals.

Table 1. Composition eliminations and remaining possibilities for the needle-like phase.

Unknown phases eliminated		
Name	***Composition***	
Sigma	(Cr,Mo)x(Ni,Co)y	
MC	TiC	
M23C6	(Cr21Mo2C6)	
Mu	Mo6(Fe,Co)	
M6C	(Ni,Co)4(Mo,W)2C	
Unknown Phases being considered		
Name	***Composition***	***Comments***
Laves	(Ni2Nb) maybe with Mo	Why Ti ?
Eta	(Ni3Ti)	Why Nb ?
Delta	(Ni3Nb)	Why Ti ?

The results presented here suggest that it may be possible to use magnetic measurements to determine the time and temperature operating history of gas turbine components consisting of Inconel 738, especially if they are exposed to temperatures exceeding the design limits. Evidence of operation in excessive temperature ranges can lead to the early onset of creep damage thereby reducing the life of the affected components. The VSM system used to carry out these experiments is not suitable for NDE use. However, work is being carried out to find out if it is possible to make measurements of a similar sensitivity using a surface probe and field-measurement system.

REFERENCES

1. Czech, N., Kirchner, F., and Stamm, W., (1996) *Elevated Temperature Coatins: Science and Technology II*, Edited by N. B. Dabotre and J. M. Hampikian, The Minerals, Metal & Materials Society, pp 361 – 371.
2. Foner, S., (1959) *Rev. Sci Inst.*, 30, 548
3. Jiles, D., (1998) *Introduction to Magnetism and Magnetic Materials*, 2nd Edition, Chapman and Hall.

DERIVATION OF A NON-LINEAR ABBM MODEL FOR THE CALCULATION OF BARKHAUSEN EFFECT

S.J. Lee[1], B. Zhu[1], C.C.H. Lo[1], D.M. Clatterbuck[2], and D.C. Jiles[1]

[1]Ames Laboratory, Iowa State University, Ames, Iowa 50011

[2]Lawrence Berkeley National Lab and Department of Materials Science and Mineral Engineering, University of California, Berkeley, CA 74270

Abstract. The Alessandro, Beatrice, Bertotti, and Montorsi (ABBM) model can describe the dynamics of domain wall motion in a ferromagnetic material which is subjected to a smoothly varying external magnetic field. The assumptions of this model limit its use to experiments where the differential permeability and time derivative of applied field are constant. In this paper, the non-linear permeability of the sample is incorporated into the ABBM model by extracting the differential permeability at different points on the B,H plane from the Jiles-Atherton (J-A) hysteresis model.

INTRODUCTION

The abrupt change in the magnetization curve of a ferromagnetic material known as the Barkhausen effect occurs when a ferromagnetic material is subjected to an external varying magnetic field. The origin of the effect is due mainly to sudden discontinuous domain wall motion caused by imperfections of the material. The domain walls may move continuously if there are no imperfections in the material. The imperfections such as inclusions, dislocations, grain boundaries, and voids may form random pinning sites and pin the domain wall motion until an external energy is provided enough to overcome the local energy barriers created by the pinning sites. The domain wall jumps occurs at this point and moves to the next available metastable state.

The Barkhausen signal can be detected using a coil encircling a sample while it is being magnetized. The abrupt change in magnetization induces an electrical voltage in the coil. The Barkhausen effect is very sensitive to the changes in the microstructure and stress of a material. Owing to this sensitivity, the Barkhasuen measurements can be used for the nondestructive evaluation of a ferromagnetic material in the application areas such as assessing the quality of heat treatment, measuring surface treatment depth, detecting grinding burns, and characterizing computer storage and recording media.

MODELS FOR THE BARKHAUSEN EFFECT

In order to analyze the experimental data in a systematic way, models are necessary to connect the Barkhausen signal to material microstructure. There have been two models describing the magnetic Barkhausen effect. The Alessandro, Beatrice, Bertotti, and Montorsi (ABBM) [1] model assumes that the rate of change of magnetic flux ϕ can be described as

$$\sigma G \dot{\phi} = H_a - (H_m + H_P), \tag{1}$$

where σ is the electrical conductivity, G is a geometry-dependent dimensionless coefficient (which reduces to G=0.1356 if a wide slab is considered), H_a is an external applied field, H_m is a field mainly from magnetostatic contribution, and H_P is the pinning field from structural disorder. The pinning field H_P is assumed to be a random function of the domain wall position and can be expressed as

$$\frac{dH_P}{d\phi}+\frac{H_P-<H_P>}{\xi}=\frac{dW}{d\phi}, \tag{2}$$

where ξ is the correlation length which represents the interaction range between the domain wall and the pinning sites. The white noise function W(ϕ) is characterized by $<dW>=0$ and $<|dW|^2>=2Ad\phi$ where A is a constant describing the variance of the fluctuations. ABBM model assumes a parabolic free energy potential and the form of H_m can be approximated from the parabolic potential by

$$H_m=\frac{\phi}{S\mu} \tag{3}$$

where S is the specimen cross-sectional area and μ is permeability of the system. From time derivative of Eqs. (1) and (3), the ABBM equation for the description of the Barkhausen events can be obtained as

$$\frac{d\dot{\phi}}{dt}+\frac{\dot{\phi}-<\dot{\phi}>}{\tau}=-\frac{1}{\sigma G}\frac{dH_P}{dt}, \tag{4}$$

where $\tau=\sigma GS\mu$. The assumptions of this model limit its use to experiments where the differential permeability and time derivative of applied field are constant. The ABBM model can not incorporate the magnetic hysteresis of a material which plays an important role in the Barkhasuen effects. Due to these limitations, the ABBM model is not ideal for applications in real situations.

The model of Jiles, Sipahi, and Williams (JSW) [2] describes the Barkhausen effect over the entire hysteresis loop. The JSW model assumes that the Barkhausen activity in a given time interval is proportional to the rate of change of the magnetization which can be calculated from hysteresis models. To consider the random nature of the Barkhausen activity, the model assumes that the number of Barkhausen activity in a given time period is related to the number of activity in the previous time period by some small random increment. This model can be described using the equation

$$\dot{M}_{JS}(t_n)=<M_{disc}>\chi'_{irr}\dot{H}[N'(t_{n-1})+\delta_{and}\sqrt{N'(t_{n-1})}, \tag{5}$$

where M_{JS} represents the Barkhausen activity in terms of the "jump sum", $<M_{disc}>$ is the average jump size, χ'_{irr} is the irreversible differential susceptibility which can be determined from hysteresis model, $\dot{H}$ is the rate of change of magnetic field with time, and δ_{rand} is a random number with mean of zero and standard deviation of unity. This model is

similar to the ABBM model in mathematical structure when the correlation distance in ABBM model is infinite. The JSW model can incorporate the stress effects on the Barkhausen activity by calculating the stress effects on the differential permeability of a material. Disadvantage of this model is that the Barkhausen signal according to time variation has not been incorporated in this model.

A new model [3] incorporating ideas from both of these models has been proposed. The new model assumes that the pinning field and domain wall velocity behave according to the ABBM model, but allows the rate of change of the magnetic flux to vary around a moving average, which is derived from the shape of the experimental hysteresis curve and the applied magnetic field waveform. As a result, the new model allows for changes in permeability with applied field and can accurately reproduce the frequency response of experimental Barkhausen signals. The model employs irreversible magnetization I_{irr} rather than magnetic flux ϕ because the Barkhausen jumps actually correspond to irreversible changes in magnetization rather than changes in magnetic induction. The model can be written in terms of I_{irr} as

$$\frac{d\dot{I}}{dt}+\frac{\dot{I}_{irr}-<\dot{I}_{irr}>}{\tau}=-\frac{1}{\sigma GS}\frac{dH_P}{dt}, \tag{6}$$

where $\tau=\sigma GS\chi'_{irr}$ and χ'_{irr} is the irreversible differential susceptibility. Both $<\dot{I}_{irr}>$ and τ are functions of the position on the hysteresis curve due to the non-linear, muti-valued properties of the differential susceptibility. $<\dot{I}_{irr}>$ and χ'_{irr} are related to each other through the applied field waveform by

$$<\dot{I}_{irr}>=\chi'_{irr}\dot{H}_a(t) \tag{7}$$

The permeability/susceptibility and applied field wave form should be recorded from experiment in order to simulate the Barkhausen effects.

Any viable hysteresis model can be used to calculate χ'_{irr}. In this work, an existing hysteresis model [4] used for the modeling of the nonlinear characteristics of soft and hard magnetic materials was employed to obtain the non-linear permeability. The algorithm of this hysteresis model yields five parameters, M_S, a, k, α and c from experimental *B-H* loops. The derivation and the physical interpretation of these five model parameters have been discussed previously [5]. The obtained magnetic permeability from the modeled hysteresis curve was incorporated into the magnetostatic field H_m, which is used for the calculation of the Barkhausen signal [6]. This approach allows quantitative comparisons to be made between the experiments and the model.

EXPERIMENTAL MEASUREMENTS

To compare the model with experiment, hysteresis loop and Barkhausen emission (BE) measurements were made on 0.18 wt% C plain carbon steel samples. During the measurements a 2 Hz magnetizing field with a sinusoidal waveform was applied to the sample. The surface magnetic field *H* was measured using a Hall sensor. The output of a search coil wound on the sample was integrated to give the induction. This signal was also filtered using a band-pass filter (500 Hz to 200 kHz) to obtain the BE signals. The

integrated voltage picked up by the search coil is shown in the insert of Fig. 1. From the integration over time of this quantity, the hysteresis loop represented by solid line can be derived as shown in Fig. 1. The dotted line is a modeled hysteresis loop obtained from the chosen hysteresis model.

RESULTS AND DISCUSSION

The five hysteresis model parameters from experimental data for 0.18 wt% C plain carbon steel sample were M_S=1.39×10^6 (A/m), a=3500 (A/m), k=950 (A/m), α=1.0×10^{-4}, and c=0.01, respectively. The hysteresis loop from the model is shown in Fig. 1 as a dotted line. Since Barkhausen signal is induced by irreversible changes in magnetization, the irreversible part of differential permeability (μ'_{irr}) or the irreversible part of differential susceptibility (χ'_{irr}) should be obtained from the J-A model for the calculation of Barkhausen signal. The relation between μ'_{irr} and χ'_{irr} is given by $\mu'_{irr} = \mu_o(1+\chi'_{irr})$. From the magnetization curve, one can derive the differential susceptibility $\chi'_{irr} = dM_{irr}/dH$. The calculated μ'_{irr} is incorporated into the magnetostatic field, H_m for the Barkhausen calculation. The maximum of μ_{irr} appears near coercivity and minimum appears at saturated magnetization. Between these values, μ'_{irr} shows a non-linear behavior. The Barkhausen model incorporating the non-linearity of the differential permeability, is able to generate Barkhausen signal which closely resembles the experimental data as shown in Fig. 2.

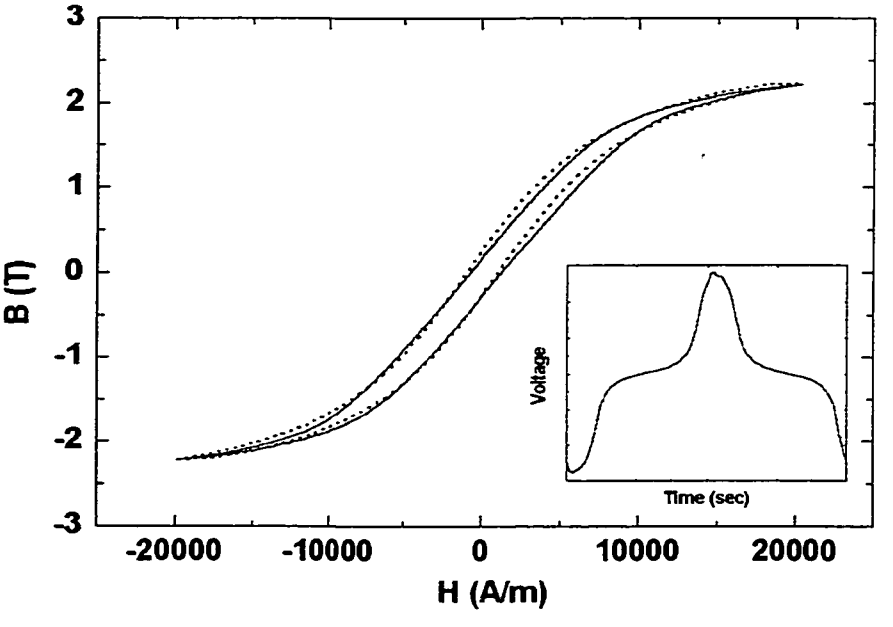

FIGURE 1. The solid line stands for the hysteresis loop for 0.18wt% C plain carbon steel. The dotted line is a modeled hysteresis loop. Insert: The integrated voltage picked up by the search coil.

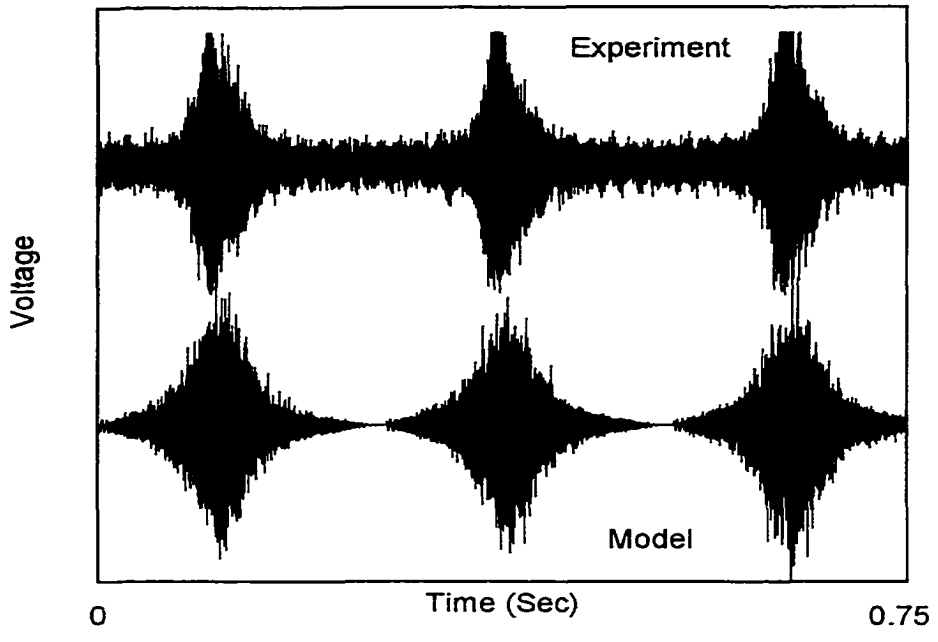

FIGURE 2. Comparison of the experimental and modeled Barkhausen signal in the time domain.

The extended model allows the investigation of the Barkhausen signal variation according to the hysteresis loop change. To simulate the effect of hysteresis loop change to the Barkhausen signal, only the effective domain density was varied. Figure 3 shows the hysteresis loops from the J-A model. Number 3 indicates the modeled hysteresis loop obtained for the 0.18wt% C plain carbon steel sample. The other four (1,2,4, and 5) loops are obtained by varying the value of the "a" parameter, sometimes referred to as the effective domain density. Numbers 1, 2, 4, and 5 stand for the values of effective domain densities of 1500 (A/m), 2500 (A/m), 4500 (A/m), and 5500 (A/m), respectively. As the values of the effective domain density changes, the hysteresis loops rotate on the M, H plane. The slope of hysteresis loop 1 is the largest near the coercivity and that of hysteresis loop 5 is the smallest near the coercivity.

The root mean square (RMS) values of the Barkhausen signal obtained using the irreversible differential permeability from the modeled hysteresis loops is shown in Fig. 4. The numbers shown in Fig. 4 represent the RMS values of the modeled Barkhausen signal corresponding to the values of the effective domain density used for the hysteresis loops as shown in Fig. 3. For the 0.18 wt% C plain carbon steel sample, the Barkhausen activity decreases as the slope of hysteresis loop near the coercivity decreases. The combination of these two complementary models allows the investigation of the Barkhausen signal with change of the hysteresis loops which is sensitive to the external loads.

CONCLUSIONS

The Barkhausen model of Alessandro, Beatrice, Bertotti, and Montorsi describes the dynamics of domain activity with a restriction of constant permeability and constant rate of change of applied field. Due to these restrictions, the model is not an ideal model for real

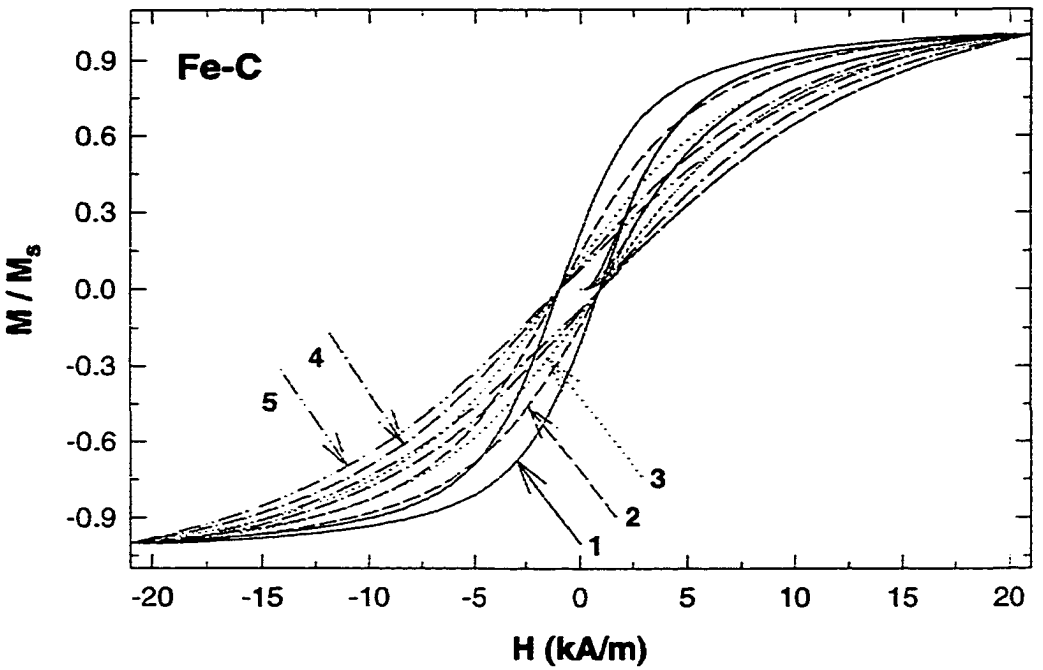

FIGURE 3. The modeled hysteresis loops for different values of the "a" parameter. Numbers 1, 2, 3, 4, and 5 stand for the values of "a" of 1500, 2500, 3500, 4500, and 5500 (A/m), respectively.

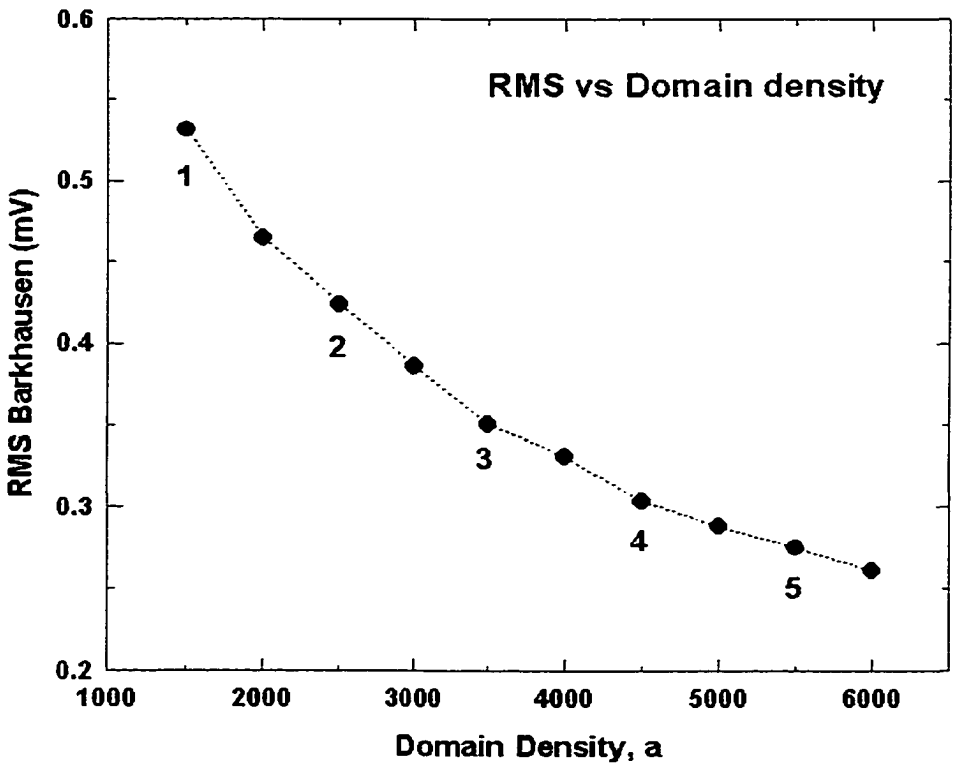

FIGURE 4. The root mean square (RMS) values of the modeled Barkhausen signals for different values of domain density.

applications. The extended model incorporating the non-linear permeability from hysteresis model can describe the Barkhausen effect over the whole hysteresis loop, not restricted to the coercivity point. The extended model allows the simulation of the Barkhausen signal variation according to the change of the hysteresis loop due to the changes in the microstructure, stress, frequency or waveform of the applied field.

ACKNOWLEDGEMENTS

This research was supported by Center for Nondestructive Evaluation at Iowa State University. This is an NSF sponsored Industry/University Cooperative Research Center.

REFERENCES

1. B. Alessandro, C. Beatrice, G. Bertotti, and A. Montorsi, J. Appl. Phys. 68, 2901 (1990).
2. D.C. Jiles, L.B. Sipahi, G. Williams, J. Appl. Phys. 73, 5830 (1993).
3. D.M. Clatterbuck, V. J. Garcia, M. J. Johnson, D. C. Jiles, J. Appl. Phys. 87, 4771 (2000).
4. D.C. Jiles and D.L. Atherton, J. Magn. Magn. Mater. 61, 48 (1986).
5. D.C. Jiles, J.B. Thoelke, M.K. Devine, IEEE Trans. Magn. 28, 27 (1992).
6. G. Bertotti, "Hysteresis in magnetism", Academic Press, San Diego, p. 268 (1998).

Micromagnetic Modeling of the Effects of Stress on Magnetic Properties

B. Zhu[a], C.C.H. Lo[a], S.J. Lee[a] and D.C. Jiles[a,b]

[a] Ames Laboratory, USDOE, Ames, IA 50011, U.S.A.

[b] Department of Materials Science and Engineering, Iowa State University, Ames, IA 50011, U.S.A.

Abstract

A micromagnetic model has been developed for investigating the effect of stress on the magnetic properties of thin films. This effect has been implemented by including the magnetoelastic energy term into the Landau-Lifshitz-Gilbert (LLG) equation. Magnetization curves of a nickel film were calculated under both tensile and compressive stresses of various magnitudes applied along the field direction. The modeling results show that both coercivity and remanence increase with increasing compressive stress but decrease with increasing tensile stress. The results are in good agreement with the previous experimental results and can be interpreted in terms of the effects of the applied stresses on the irreversible rotation of magnetic moments during magnetization reversal under an applied field.

1.Introduction

Applications of magnetic thin films have increased in the areas of information storage and sensor devices. Computational micromagnetics has proven a useful tool as it leads to a deeper

understanding of magnetization processes in thin films through visualization of the simulated reversal processes for the magnetic moments.

Although stress has an important role in magnetism [1], it is surprising that modeling of magnetization processes in thin films in the presence of external stresses has received little attention. A magnetomechanical model has been developed by Sablik and Jiles [2, 3] to describe the stress effect on magnetic properties of bulk materials. However, recent experimental results obtained from nickel thin films [4] showed a stress dependence of the hysteresis loop properties different from the predictions of the Sablik-Jiles model. Such differences can be attributed to the different mechanisms of magnetization reversal in thin films and bulk materials [4]. In order to investigate the stress effect in magnetic thin films, a new micromagnetic model based on the Landau-Lifshitz-Gilbert (LLG) equation [5] has been developed. The magnetoelastic energy term [6] induced by an external stress was included in the Gibbs free energy of the material. The magnetic moment configuration was calculated by solving the LLG equation. The modeling results show that the hysteresis loop properties, such as coercivity and remanence, change drastically with applied stress in a way different from that of bulk magnetic materials. These results are in good agreement with experimental data on nickel thin films reported in the literature [4].

2. Micromagnetic Model of stress effect

In the micromagnetics approach an equilibrium magnetization configuration of a ferromagnetic body can be found by minimizing its total Gibbs free energy E_{tot} which can be written as a sum of several energy contributions:

$$E_{tot} = E_{field} + E_{exch} + E_{anis} + E_{demag} + E_{me} \quad , \tag{1}$$

where E_{field} is the energy contribution due to an external field (the Zeeman energy term), E_{exch} is the exchange energy, E_{anis} is the magnetocrystalline anisotropy energy, E_{demag} is the demagnetizing or stray field energy and E_{me} is the magnetoelastic energy. In general, the effective field $\boldsymbol{H}_{eff}$ acting on a given magnetic moment can be defined as the derivative of energy with respect to magnetization ,

$$\boldsymbol{H}_{eff} = -\frac{1}{\mu_0}\frac{\partial E}{\partial \boldsymbol{M}} \quad . \tag{2}$$

Correspondingly, the effective field can be written as a sum of several field components:

$$\boldsymbol{H}_{eff} = \boldsymbol{H}_{field} + \boldsymbol{H}_{exch} + \boldsymbol{H}_{anis} + \boldsymbol{H}_{demag} + \boldsymbol{H}_{me} \quad , \tag{3}$$

where $\boldsymbol{H}_{field}$ is the external applied field, $\boldsymbol{H}_{exch}$ is the exchange coupling field, $\boldsymbol{H}_{anis}$ is the magnetocrystalline anisotropy field, $\boldsymbol{H}_{demag}$ is the magnetostatic field and $\boldsymbol{H}_{me}$ is the effective field induced by stress via magnetoelastic coupling. At equilibrium, the magnetization vector $\boldsymbol{M}$ is parallel to $\boldsymbol{H}_{eff}$ and the total free energy reaches a minimum. This condition is usually solved by integration of the LLG equation [5] which is given by:

$$\frac{d\boldsymbol{M}}{dt} = -\gamma \boldsymbol{M} \times \boldsymbol{H}_{eff} - \frac{\gamma\alpha}{M_s}\boldsymbol{M} \times (\boldsymbol{M} \times \boldsymbol{H}_{eff}) \quad , \tag{4}$$

where M_s is the saturation magnetization, γ is the gyromagnetic ratio and α is the damping coefficient.

When the magnetic material is under an applied stress, the magnetoelastic energy E_{me} induced by the stress has to be included in Gibbs free energy (Eq. (1)). For cubic materials, the magnetoelastic energy E_{me} under an applied stress σ is given by [6]:

$$E_{me} = -\frac{3}{2}\lambda_{100}\sigma(\alpha_1^2\gamma_1^2 + \alpha_2^2\gamma_2^2 + \alpha_3^2\gamma_3^2) - 3\lambda_{111}\sigma(\alpha_1\alpha_2\gamma_1\gamma_2 + \alpha_2\alpha_3\gamma_2\gamma_3 + \alpha_3\alpha_1\gamma_3\gamma_1) \quad , \quad (5)$$

where λ_{100} and λ_{111} are the magnetostrictions of the material along the <100> and <111> directions respectively, α_1, α_2, α_3 are the directional cosines of $\boldsymbol{M}$ and γ_1, γ_2, γ_3 are the directional cosines of σ with respect to the crystal axes. The corresponding effective field $\boldsymbol{H}_{me}$ can be calculated from Eq. (2) and then incorporated into the LLG equation (Eq. (4)) to simulate how the magnetic moments change under the magnetic field in the presence of the applied stress.

3. Results and discussion

The model system is a two-dimensional grid of width a (x direction) and height b (y direction) extending infinitely along the z direction . The grid is divided into a number of square cells. The magnetic moments are positioned at the center of each cell. Each of these magnetic moments is free to rotate in three dimension but its magnitude is kept constant. The Von Neumann type boundary condition ($\partial M / \partial n = 0$) is assumed in the calculation.

The simulation is based on the algorithm provided by NIST [7] and the material parameters of nickel (M_s=0.48e6A/m, K_1 =-5.7e3Jm^{-3}, λ_{100}=-46e-6, λ_{111}=-24e-6) were used. A 2 μm wide, 0.5 μm high and 20 nm thick rectangular element with cell size 20nm was used in the present study. The demagnetizing field was obtained by calculating the average field in each cell [7] using the formulae from [8].

The initial configuration of magnetic moments contained seven domains. Both the stress and the magnetic field were applied along the long axis of the rectangular element (the x direction). The applied field amplitude is 80 kA/m. When calculating the magnetization curves the applied field was stepped (step size = 1600A/m) through in a linear manner. At the end of each field step, when the magnetic moments attained an equilibrium configuration, the x-components of the magnetic moments were summed over the grid to obtain the magnetization component of the model system in the x-direction which was plotted against the applied field to obtain the hysteresis loop.

Figs 1 and 2 show the simulated hysteresis loops for a nickel thin film under different levels of tensile and compressive stresses. The hysteresis loop displays systematic changes under the applied stresses.

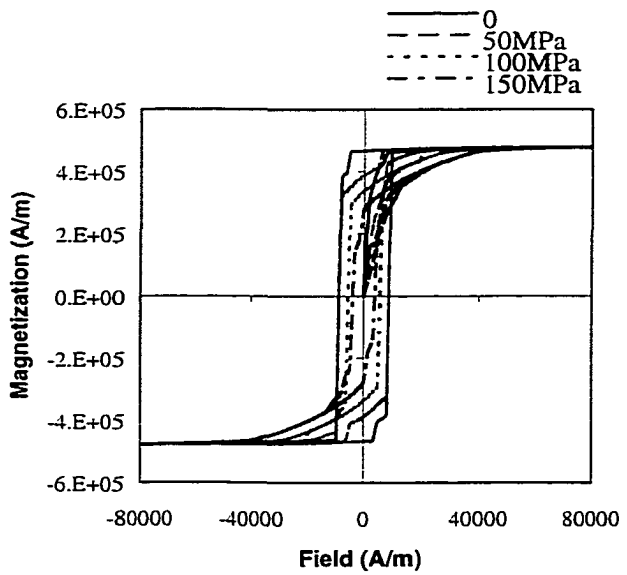

Figure 1 Hysteresis loops under tensile stresses

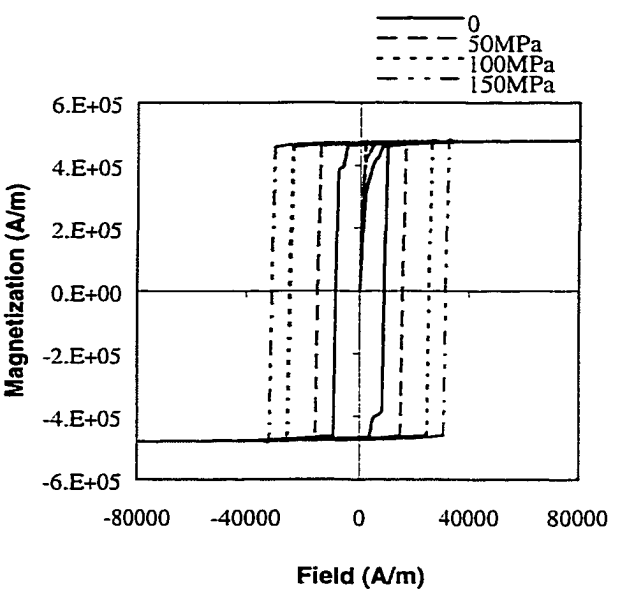

Figure 2 Hysteresis loops under compressive stresses

Fig. 3 shows the variation of coercivity due to the applied stress (relative to the unstressed case). The results show that the coercivity increases significantly with increasing compressive stress and decreases with increasing tensile stress. The modeling results are in good agreement with the experimental data on nickel film [4] but are quite different from those obtained from bulk nickel samples [9]. Such differences can be attributed to the different effects of applied stresses on two different mechanisms of magnetization reversal, namely irreversible domain rotation and domain wall movement [10]. It has been pointed out that when the reversal process is dominated by irreversible domain rotation, the field required to switch the domain magnetization (i.e. the coercivity) will increase if the easy axis induced by the external stress is parallel to the applied field (e.g. compressive stress applied to nickel along the field direction) [10]. This can be explained by considering coherent rotation of domain magnetization against the stress-induced uniaxial anisotropy under an applied field. As described by the Stoner-Wolfarth model [11], the critical field at which the domain magnetization switches abruptly increases with the anisotropy. Therefore it is expected that the coercivity of the model system, whose magnetization reversal process involves essentially irreversible rotation of magnetic moments, will increase with increasing compressive stress applied in the field direction. Similarly the coercivity will decrease if the easy axis induced by the external stress is perpendicular to the applied field (e.g. tensile stress on nickel along the field direction). For the bulk materials, the predominant mechanism is domain wall movement. Quantitative predictions of the effects of stress on magnetic properties of bulk materials has been give by Sablik-Jiles model [2,3] and were found in good agreement with experimental results [9].

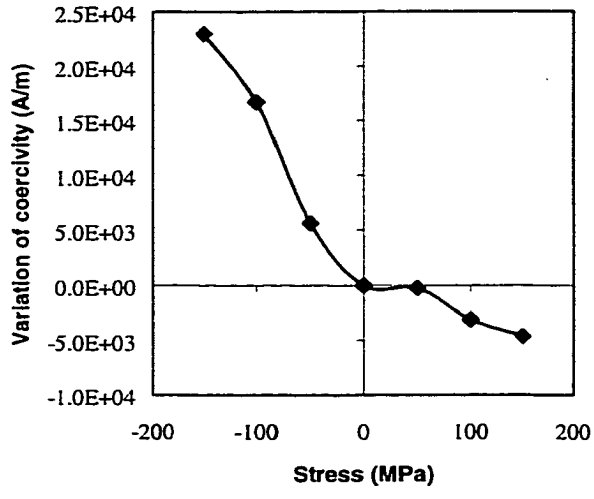

Figure 3 The variation of coercivity for Ni film under stress

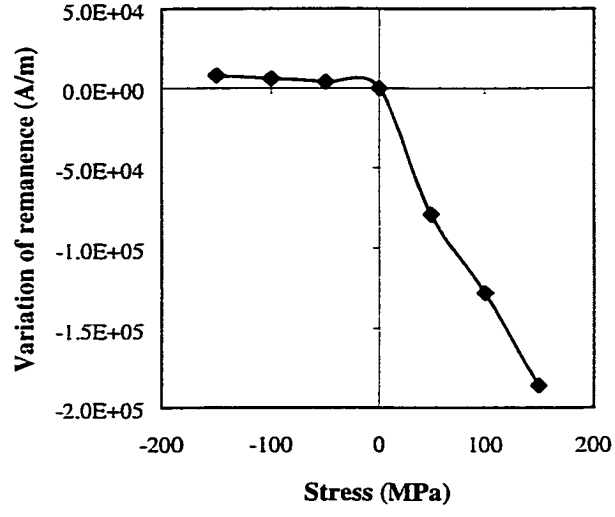

Figure 4 The variation of remanence of Ni film under stress

Fig. 4 shows the variation of the remanence at different stress levels. The results show that the remanence increases with increasing compressive stress and decreases with increasing tensile stress. This can be interpreted based on the argument given above. A tensile stress in the field direction induces an anisotropy perpendicular to the applied field. As the applied field is reduced from saturation, due to the stress-induced anisotropy the domain magnetization may partially rotate reversibly away from the field direction before it suddenly switches to the opposite direction. This effect of reversible rotation becomes more pronounced as the stress-induced anisotropy increases. As a result the remanence decreases with tensile stress. Compressive stress did not change the remanence so much because the remanence in the unstressed state was very close to the saturation value, as shown in Fig. 2.

4. Conclusions

Micromagnetic modeling of the effect of stress on magnetic properties of thin films has been carried out by including the magnetoelastic energy term in the Landau-Lifshitz-Gilbert equation. Magnetization curves of nickel thin film were calculated and the modeling results show that the shape of hysteresis loop and the magnetic properties (e.g. coercivity and remanence) change significantly in a systematic manner under an applied stress. The variation of the coercivity with applied stress can be attributed to the effects of the stress-induced anisotropy on the irreversible rotation of magnetic moments which is the dominant mechanism of magnetization reversal in the model system used in the present study.

Acknowledgement

This work was supported by the National Science Foundation under grant number DMR-9902415.

References

[1] R.M.Bozorth, *Ferromagnetism*, Van Nostrand, New York, 1951.

[2] M.J.Sablik, H,Kwun, G.L.Burkhardt and D.C.Jiles, *J.Appl.Phys*, vol.61, pp.3799, 1987.

[3] D.C.Jiles, *J.Phys.D:Appl.Phys*, vol.28, pp.1537, 1995.

[4] L.Callegaro and E.Puppin, *Appl. Phys.Lett*, vol.68, no.9, pp.1279, 1996.

[5] T.L. Gilbert, *Phys. Rev.*, vol.100, pp. 1243, 1955.

[6] B.D.Cullity, *Introduction to Magnetic Materials*, Addison-Wesley, 1972.

[7] M.J.Donahue, *OOMMF User's guide 1.1b0*, 2000.

[8] A.J.Newell, W.Williams and D.J.Dunlop, *J.Geophysical Research*, vol.98, pp.9551, 1993.

[9] D.C.Jiles, T.T.Chang, D.R.Hougen and R.Ranjan, *J.Appl.Phys*, vol.64, pp.3620, 1988.

[10] I.J.Garshelis, *J.Appl.Phys*, vol.73, pp.5629, 1993.

[11] E.C.Stoner and E.P.Wohlfarth, *Phil.Trans.Roy.Soc.* vol.A240, pp.599,1948.

Application of non-linear Barkhausen model incorporating anhysteretic susceptibility to annealed low carbon Fe sample

S.J. Lee[a], B. Zhu[a], C.C.H. Lo[a], D.M. Clatterbuck[b], and D.C. Jiles[a]
[a] Ames Laboratory, Iowa State University, Ames, IA 50011, U.S.A
[b]Lawrence Berkeley National Lab and Depatment of Materials Science and Mineral Engineering, University of California, Berkeley, CA 94270

Abstract

The Alessandro, Beatrice, Bertotti, and Montorsi (ABBM) model can describe the dynamics of domain wall motion in a ferromagnetic material which is subjected to a smoothly varying external magnetic field. The assumptions of this model limit its use to experiments where the differential permeability and time derivative of applied field are constant. In this paper, the equilibrium susceptibility is incorporated into the model of ABBM model instead of a constant differential permeability which is the correct limiting case if a small pinning field and low applied field rate are considered.

1. Introduction

The magnetic Barkhausen effect (BE), the abrupt change in the magnetization curve, occurs when a ferromagnetic material is subjected to an externally varying magnetic field. The origin of the effect has been known to be due primarily to the discontinuous domain walls motion through the material caused by imperfections of the material. The imperfections such as inclusions, dislocations, grain boundaries, and voids may form random pinning sites and pin the domain wall motion until an external energy is provided enough to overcome the local energy barriers created by the pinning sites. The domain wall jumps occurs at this point and moves to the next available metastable state.

The Barkhausen signal can be detected using a coil encircling a sample while it is being magnetized. The abrupt change in magnetization induces an electrical voltage in the coil. The Barkhausen effect is very sensitive to the changes in the microstructure and stress of a material. Owing to this sensitivity, the Barkhasuen measurements can be used for the nondestructive evaluation of a ferromagnetic material in the application areas such as assessing the quality of heat treatment, measuring surface treatment depth, and detecting grinding burns.

2. Barkhausen effect models

In order to analyze the experimental data in a systematic way, models are necessary to connect the Barkhausen signal to material microstructure. The Barkhausen model of Alessandro et al. (ABBM) [1] provides a description of the dynamics of domain wall motion in an effective random potential, but is limited to regions of the hysteresis curve near the coercive point where the permeability is a constant and under constant rate of change of applied field. Because different domain wall processes (i.e. domain wall motion, domain wall creation, etc.) occur at different locations on the hysteresis loop, the above requirement ensures that a single domain wall process is dominating the behavior. It is also possible ensure that domain wall motion is the dominant process if we consider hysteresis loops which occur at low fields (generally below the knee of the major hysteresis loop). In this case, the domain wall motion is not a stationary process as in the ABBM model, but this does not add further complications assuming that computer simulations are used to study the process rather than analytic methods. These ideas have been incorporated in earlier papers where a non-constant permeability derived from experiment [2] or hysteresis models [3] was used. Below we demonstrate that the model should contain the anhysteretic permeability rather than the total permeability.

Magni et al. [4] have previously shown that a stochastic model similar to the ABBM Barkhausen model can be used describe hysteresis in magnetic materials. The model is a dynamic model based on the idea of a domain wall moving in a random potential developed by Néel [5]. In the limit of low magnetization rate, the rate-independent hysteresis of the system can be understood in terms of the superposition of envelope curves generated around a set of independent free energy curves. It is assumed that the free energy contribution can be separated into two components: a smoothly varying component H_m which describes as the magneto-static contribution, and a randomly varying term H_p which arises from the structural disorder in the system. H_m is assumed linear in M, while H_p is described by suitable stochastic differential equations. The ABBM model and the Stochastic hysteresis model can be written in terms of the magnetization M as:

$$\gamma dM/dt = H_a - H_m - H_p(M), \qquad (1)$$

or its time derivative, where γ is a constant that includes the geometry and electrical conductivity of the system, and H_a is the applied field. In the ABBM model, $\gamma = \sigma G S \mu_o$, where σ is the electrical conductivity, G is a geometry-dependent dimensionless coefficient (which reduces to G=0.1356 if a wide slab is considered), S is the cross sectional area of the slab, and H_a is the applied field.

In the quasi-static limit, equilibrium requires, $H_a = H_m(M) + H_p(M)$. But in the limit of zero structural disorder, or $H_p \rightarrow 0$, the envelope construction in Fig. 1 collapses to the curve H_m. In physical terms, in the quasi-static limit with zero pinning due to structural disorder, the magnetization curve should collapse to the anhysteretic magnetization. This would require that

$H_m(M)$ describe the anhysteretic magnetization curve. We can rewrite this in terms of the anhysteretic susceptibility as $H_m = M/\chi_{an}(M)$, where $\chi_{an}(M)$ is the anhysteretic susceptibility which depends on M. Since $\chi_{an}(M)$ is simply a relation that defines H_m in terms of M, it will not depend on the value of H_p or the requirement of low magnetization rate and is thus a general relation. This can also be shown by analyzing the thermodynamics of the Stochastic model within the framework of the Functional Integration Approach to hysteresis [6,7].

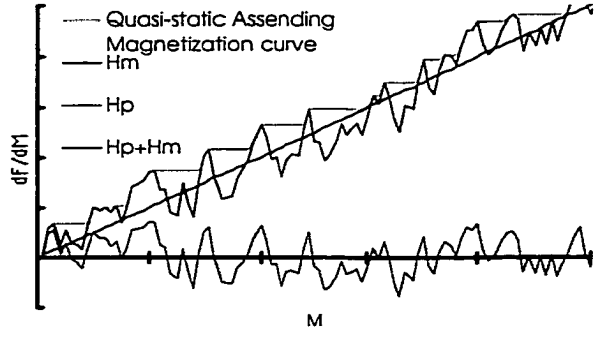

Fig. 1. Decomposition of the free energy gradient dF/dM into H_p and H_m.

The anhysteretic susceptibility $\chi_{an}(M)$ for the modeling can be obtained from experiment or from phenomenological model such as Langevin function. In the ABBM model, the magneto-static field H_m is given as M/μ where μ is a constant differential permeability. In this case, H_m is linear and we would simply drop the dependence of χ_{an} on M. We could equivalently analyze the problem using the time derivatives of M_{an} and H_m in which case we would use the differential susceptibility. An important assumption of the above analysis is the fact that while H_m is a function of M, the statistical properties of H_p do not change. This implies that a single magnetization process is taking place which is only true in the low field region. Also as in Ref. 4, we assume that the statistical ensemble of free energy curves which are averaged to give the hysteresis curve are independent. In addition, the model does not account for long range reversible effects. A small change in field may create reversible effects, but these will become locked in and irreversible at larger applied field, which does make some physical sense if domain wall motion is dominant.

2. Experimental Details

The sample used in this study is a Fe-0.05wt%C alloy chill-cast from high purity iron. The sample has a diameter of 6.35 mm and length 100 mm. It was annealed in a vacuum furnace at 905°C for one hour and then cooled slowly inside the furnace.

The sample was demagnetized before the anhysteresis measurements. During the measurements a dc field superimposed with an ac field with decaying amplitude was then applied

to the sample. The anhysteretic curve was obtained by measuring the magnetic induction as a function of the dc field.

Barkhausen emission and hysteresis loop measurements were made on the sample. During the measurements a 2 Hz sinusoidal excitation field was applied to the sample. The surface field was measured using a Hall sensor mounted on the sample surface. The voltage signal induced across a pickup coil wound on the sample was acquired and integrated numerically to obtain the flux density B. The pick up coil signal was also filtered (passband: 1 kHz to 250 kHz) and amplified (voltage gain: 60dB) to obtain the BE signal. The signal was acquired into a computer (sampling rate: 10 kHz) and analyzed to obtain the root-mean-square value, the pulse height distribution, the frequency spectrum and power density spectrum of the Barkhausen voltage signal [8].

3. Results and Discussion

Figure 2 shows the experimental anhysteretic magnetization curve (solid circle) and phenomenological model (solid line) obtained from the modified Langevin function which is given by

$$M_{an}(H) = M_s\left(\coth\left(\frac{H+\alpha M}{a}\right)-\frac{a}{H+\alpha M}\right),$$

where M_s is the magnetization saturation, α is a mean field parameter representing interdomain coupling, and a is an effective domain density characterizing the shape of the anhysteretic magnetization. The used values for the fitting are $M_s=1.8\times10^6$ (A/m), $\alpha=1.0\times10^{-3}$, and $a=870$ (A/m), respectively. The measured hysteresis loop (dotted line) is shown in Fig. 2. The hysteresis of a ferromagnetic material is created due to the energy loss of a domain wall motion from the pinning sites. The solid line in Fig. 2 is a modeled hysteresis loop from the Jiles-Atherton (J-A) model which treats the pinning energy loss as a constant parameter k. The algorithm of this hysteresis model yields five parameters, M_S, α, a, c, and k from experimental B-H loops. The derivation and the physical interpretation of these five model parameters have been discussed previously [9]. The obtained magnetic permeability from the modeled hysteresis curve was incorporated into the magnetostatic field H_m, which is used for the calculation of the Barkhausen signal [3]. The five hysteresis model parameters from experimental data for Fe-0.05 wt%C sample were k=400 (A/m) and c=0.01 with the same values of M_s, α, and a used in the modified Langevin function. The time domain of the simulated and experimental Barkhausen signals are shown in Fig. 4. The peaks of Barkhausen signal agree well between the experiment and model. The dotted line represents the applied external sinusoidal excitation field which was applied to the sample. The Barkhausen signal is strong in the small absolute magnitude of the

applied field and weak in the strong applied filed. The domain activity near the saturation is weak, as a result the Barkhausen phenomena in this region is weak as shown in Fig. 4. The peaks in the experimental Barkhausen signal are evenly distributed in the time domain spectrum. The simulated Barkhausen signal incorporating anhysteretic susceptibility shows the same behavior as that of experiment.

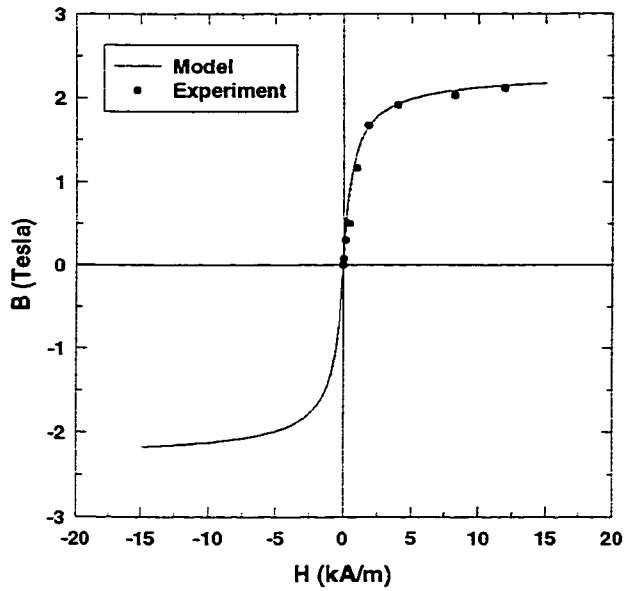

Figure 2. Anhysteretic magnetization curve; experiment (solid circle) and model (solide line).

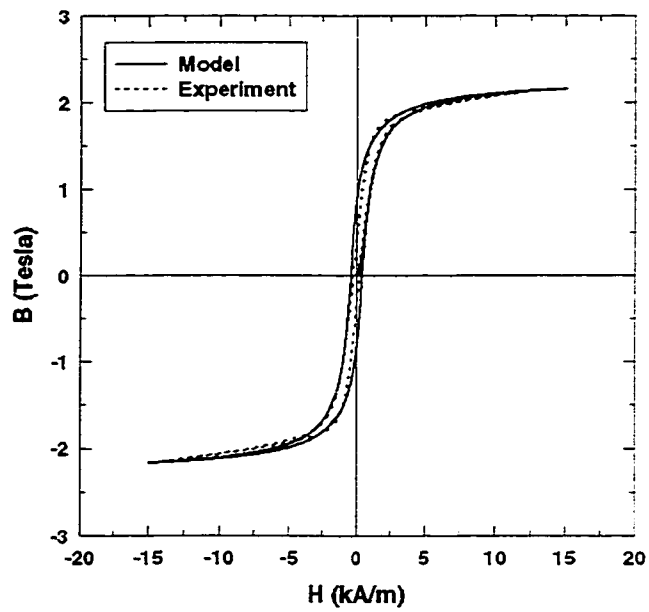

Figure 3. Hysteresis loop; experiment (dotted line), model (solid line).

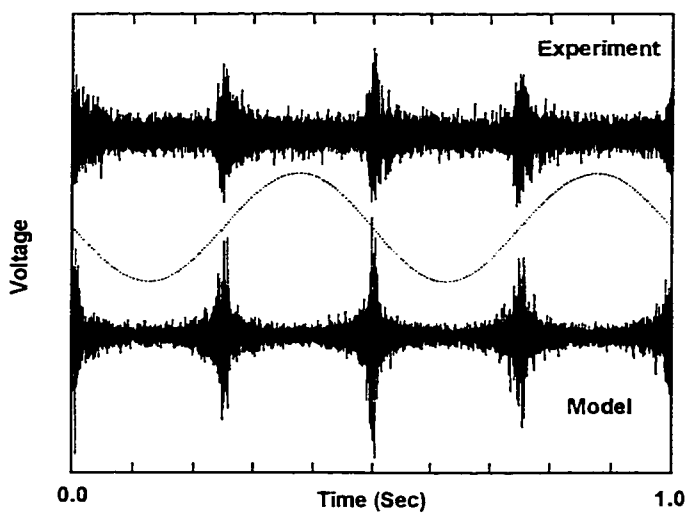

Figure 4. The experimental and modeled Barkhausen signal. The dotted line is the applied external sinusoidal field of frequency 2Hz.

4. Conclusions

In the Barkhausen model of Alessandro, Beatrice, Bertotti, and Montorsi, the magnetostatic field H_m is assumed to be linear in M and therefore the model is restricted to constant permeability and constant rate of change of applied field. Due to these restrictions, the model is not an ideal model for real applications. The model incorporating the equilibrium susceptibility can describe the Barkhausen effect over the time-domain with a periodicity of applied sinusoidal field. This model allows the accurate description of the peak positions of the Barkhausen signal and the shape of the signal agrees well with experimental data obtained on an annealed low carbon Fe sample.

ACKNOWLEDGEMENTS

This research was supported by Center for Nondestructive Evaluation at Iowa State University. This is an NSF sponsored Industry/University Cooperative Research Center.

References

[1] B. Alessandro, C. Beatrice, G. Bertotti, and A. Montorsi, J. Appl. Phys. 68, 2901 (1990).
[2] D.C. Jiles, L.B. Sipahi, G. Williams, J. Appl. Phys. 73, 5830 (1993).
[3] S.J. Lee, B. Zhu, C.C.H. Lo, D.M. Clatterbuck, D.C. Jiles, to be published on QNDE 2000.
[4] A. Magni, C. Beatrice, G. Durin, and G. Bertotti, *J. Appl. Phys.* **86,** 3253 (1999).
[5] L. Neel. *Cah. Phys.* **12**, 1 (1943).
[6] G. Bertotti, I.D. Mayergoyz, V. Basso, A. Magni, *Phys. Rev. E* **60**, 1428 (1999).
[7] D. M. Clatterbuck manuscript in preparation.
[8] A. Magni, C. Beatrice, G. Durin, and G. Bertotti, *J. Appl. Phys.* **86,** 3253 (1999).
[9] D.C. Jiles and D.L. Atherton, J. Magn. Magn. Mater. 61, 48 (1986).

REFERENCES

[1] H.Barkhausen, *Phys.Z*, vol.23, pp.225, 1919.

[2] P.Weiss, *Journal of Physics*, vol.6, pp.661, 1907.

[3] R.Becker and W.Doring, *Ferromagnetism*, Springer-Verlag, Berlin, 1938.

[4] A.Seeger, H.Kronmuller, H.Rieger and H.Trauble, *Journal of Applied Physics*, vol.35, pp.740, 1964.

[5] H.R.Hilzinger and H.Kronmuller, *Journal of Magnetism and Magnetic Materials*, vol.2, pp.11, 1976.

[6] G.Bertotti, *IEEE Transactions on Magnetics*, vol.24, pp.621, 1988.

[7] B.Alessandro, C.Beatrice, G.Bertotti, and A.Montorsi, *Journal of Applied Physics*, vol.68, no.6, pp.2901, 1990.

[8] B.Alessandro, C.Beatrice, G.Bertotti, and A.Montorsi, *Journal of Applied Physics*, vol.68, no.6, pp.2908, 1990.

[9] A.Papoulis, *Probability, Random Variables, and Stochastic Processes*, McGraw-Hill, New York, 1984.

[10] D.C.Jiles, L.B.Sipahi, and G.Williams, *Journal of Applied Physics*, vol.73, no.10, pp.5830, 1993.

[11] W.F.Brown, Jr., *Micromagnetics*, Interscience Publishers, New York, 1963.

[12] G.T.Rado and H.Suhl, *Magnetism*, Vol.III, Academic Press, New York, 1963.

[13] A.Aharoni and S.Shtrikman, *Physical Review*, vol.109, pp.1522, 1958.

[14] D.C.Jiles, *Introduction to Magnetism and Magnetic Materials*, Chapman & Hall, London, 1991.

[15] H.J.Williams and W.Whockley, *Physics Review*, vol.75, pp.178, 1949.

[16] L.Néel, *Cahiers de Physique*, vol.25, pp.21, 1944.

[17] B.D.Cullity, *Introduction to Magnetic Materials*, Addison-Wesley, Reading, Massachusetts, 1972.

[18] L.J.Dijkstra and C.Wert, *Physical Review*, vol.79, pp.979, 1950.

[19] J.B.Goodenough, *Physical Review*, vol.95, pp.917, 1954.

[20] W.D.Nix and R.A.Huggins, *Physical Review*, vol.135, pp.401, 1964.

[21] J.Kameda and R.Ranjan, *Acta Metall*, vol.35, no.7, pp.1515, 1987

[22] H.T.Ng, C.C.Yu and D.H.L.Ng, *IEEE Transactions on Magnetics*, vol.32, no.5, pp.4851, 1996.

[23] D.J.Buttle, J.P.Jakubovics and G.A.D.Briggs, *Philosophical Magazine A*, vol.55, no.6, pp.735, 1987.

[24] C.Kittel and J.K.Galt, *Solid State Physics*, no.9, pp.437, Academic Press, New York, 1956.

[25] H.J.Williams, W.Shockley and C.Kittel, *Physical Review*, vol.80, pp.1090, 1950.

[26] C.Jagadish, L.Clapham and D.L.Atherton, *NDT International*, vol.22, pp.297, 1989.

[27] J.C.McClure,Jr. and K.Schröder, *CRC Critical Reviews in Solid State Sciences*, vol.6, pp.45, 1976.

[28] R.S.Tebble, I.C.Skidmore and W.D.Corner, *Phys.Soc.Proc*, vol.63, no.367A, pp.739, 1950.

[29] G.A.Matzkanin, R.E.Beissner and C.M.Teller, *The Barkhausen Effect and Its Application to Nondestructive Evaluation*, SWRI Report, No.NTIAC-79-2, 1979.

[30] D.K.Bhattacharya and S.Vaidyanathan, *Journal of Magnetism and Magnetic Materials*, vol.166, pp.111, 1997.

[31] L.B.Sipahi, D.C.Jiles and D.Chandler, *Journal of Applied Physics*, vol.73, no.10, pp.5623, 1993.

[32] A.Dhar and D.L.Atherton, *IEEE Transactions on Magnetics*, vol.28, no.6, pp.3363, 1992.

[33] T.R.Haller and J.J.Kramer, *Journal of Applied Physics*, vol.41, pp.1036, 1970.

[34] L.B.Sipahi, *IEEE Transactions on Magnetics*, vol.30, no.6, pp.4590, 1994.

[35] C.G.Gardner, G.A.Matzkanin and D.L.Davidson, *International Journal of Nondestructive Testing*, vol.3, pp.131, 1971.

[36] R.M.Bozorth, *Ferromagnetism*, Van Nostrand, Now York, 1951.

[37] R.L.Pasley, *Materials Evaluation*, vol.28, pp.157, 1970.

[38] J.F.Bussière, *Materials Evaluation*, vol.44, pp.560, 1986.

[39] D.C.Jiles, *IEEE Transaction on Magnetics*, vol.25, no.5, pp.3455, 1989.

[40] C.Jagadish, L.Clapham and D.L.Atherton, *IEEE Transactions on Magnetics*, vol.26, no.3, pp.1160, 1990.

[41] H.Kwun, *Journal of Magnetism and Magnetic Material*, vol.49, pp.235, 1985.

[42] S.Timoshenko and J.N.Goodier, *Theory of Elasticity, second edition*, McGraw-Hill, New York, 1951.

[43] M.J.Sablik, *Journal of Applied Physics*, vol.74, no.9, pp.5898, 1993.

[44] M.J.Sablik and D.C.Jiles, *IEEE Transactions on Magnetics*, vol.29, pp.2113, 1993.

[45] M.J.Sablik and B.Augustyniak, *Journal of Applied Physics*, vol.79, no.2, pp.963, 1996.

[46] K.Titto, *Residual Stress in Design, Process and Materials Selection*, pp.27, ASM International 1987.

[47] R.Ranjan, D.C.Jiles, and P.K.Rastogi, *IEEE Transactions on Magnetics*, vol.23, no.3, pp.1869, 1987.

[48] S.Titto, M.Otala and S.Säynäjäkangas, *NDT International*, vol.9, pp.117, 1976.

[49] C.Gatelier-Rothéa, P.Fleischmann, J.Chicois and R.Fougères, *Nondestructive Testing and Evaluation*, vol.8-9, pp.591, 1992.

[50] R.Ranjan, D.C.Jiles, O.Buck and R.B.Thompson, *Journal of Applied Physics*, vol.61, no.8, pp.3199, 1987.

[51] H.Sakamoto, M.Okada and M.Homma, *IEEE Transactions on Magnetics*, vol.23, no.5, pp.2236, 1987.

[52] R.A.Taylor, J.P.Jakubovics, B.Astié and J.Degauque, *Journal of Magnetism and Magnetic Materials*, vol.31-34, pp.970, 1983.

[53] R.Ranjan, O.Buck and R.B.Thompson, *Journal of Applied Physics*, vol.61, no.8, pp.3197, 1987.

[54] D.J.Buttle, C.B.Scruby, J.P.Jakubovics and G.A.D.Briggs, *Philosophical Magazine A*, vol.55, no.6, pp.717, 1987.

[55] D.G.Hwang and H.C.Kim, *Journal of Physics D: Applied Physics*, vol.21, pp.1807, 1988.

[56] U.Lieneweg, *IEEE Transactions on Magnetics*, vol.10, no.2, pp.118, 1974.

[57] A.J.Birkett, W.D.Corner, B.K.Tanner and S.M.Thompson, *Journal of Physics D: Applied Physics*, vol.22, pp.1240, 1989.

[58] H.C.Kim, D.G.Hwang and B.K.Choi, *Journal of Physics D: Applied Physics*, vol.21, pp.168, 1988.

[59] T.W.Krause, L.Clapham and D.L.Atherton, *Journal of Applied Physics*, vol.75, no.12, pp.7983, 1994.

[60] P.Höller, *Nondestructive Characterization of Materials II*, pp.211, New York, Plenum, 1987.

[61] M.Dubois and M.Fiset, *Materials Science and Technology*, vol.11, pp.264, 1995.

[62] S.Vaidyanathan, V.Moorthy, T.Jayakumar and B.Raj, *Materials Evaluation*, pp.449, March, 1998.

[63] O.Sundström and K.Törrönen, *Materials Evaluation*, vol.37, pp.51, 1979.

[64] Z.J.Chen, A.Strom and D.C.Jiles, *IEEE Transactions on Magnetics*, vol.29, no.6, pp.3031, 1993.

[65] R.J.Pro, *Materials Evaluation*, vol.45, pp.610, 1987.

[66] P.Gondi, G.Mattogno, A.Sili and G.Foderado, *Nondestructive Testing and Evaluation*, vol.10, pp.255, 1993.

[67] L.B.Sipahi, *IEEE Transactions on Magnetics*, vol.30, no.6, pp. 4830, 1994.

[68] W.A.Theiner and I.Altpeter, *New procedures in nondestructive testing : proceedings of the Germany-U.S. workshop*, edited by P.Höller, Springer-Verlag, New York, 1983.

[69] W.A.Theiner, I.Altpeter and R.Kern, *Nondestructive Characterization of Materials II*, edited by J.F.Bussiere, Plenum Press, New York, 1986.

[70] L.Clapham, T.W.Klause, H.Olsen, B.Ma, D.L.Atherton, P.Clark and T.M.Holden, *Nondestructive Testing and Evaluation International*, vol.28, pp.73, 1995.

[71] D.C.Jiles and L.Suominen, *IEEE Transactions on Magnetics*, vol.30, pp.4924, 1994.

[72] A.P.Parakka and D.C.Jiles, *Journal of Magnetism and Magnetic Materials*, vol.140-144, pp.1841, 1995.

[73] B.Zhu, M.J.Johnson, C.C.Lo, S.J.Lee and D.C.Jiles, *Magneprobe Manual*, 2000.

[74] W.H.Press, S.A.Teukolsky, W.T.Vetterling and B.P.Flannery, *Numerical Recipes in C : The Art of Scientific Computing*, Cambridge University Press, New York, 1993.

[75] L.Clapham, C.Jagadish and D.L.Atherton, *Acta metallurgica et materialia*, vol.39, no.7, pp.1555, 1991.

[76] M.G.Hetherington, J.P.Jakubovics, J.A.Szpunar and B.K.Tanner, *Philosophical Magazine B*, vol.56, pp.561, 1987.

[77] J.F.Shackelford, *Introduction to Materials Science for Engineers*, Prentice Hall, New Jersey, 1999.

[78] D.C.Jiles, *Czech Journal of Physics*, vol. 50, no.8, pp. 893, 2000.

[79] G.Bach, K.Goebbels and W.A.Theiner, *Materials Evaluation*, vol.46, pp.1576, 1988.

[80] R.M.Fix, K.Tiitto and S.Tiitto, *Materials Evaluation*, vol.48, pp.994, 1990.

[81] D.C.Jiles and D.L.Atherton, *Journal of Magnetism and Magnetic Materials*, vol.61, pp.48, 1986.

[82] D.C.Jiles, S.J.Lee, J.Kenkel, and K.L.Metlov, *Applied Physics Letter*, vol.77, no.7, pp.1029, 2000.

[83] P.Langevin, *Annales de Chem.et.Phys*, vol.5, pp.70, 1905.

[84] D.C.Jiles and D.L.Atherton, *IEEE Transactions on Magnetics*, vol.19, pp.2183, 1983.

[85] S.Chikazumi, *Physics of magnetism*, John Wiley and Sons, New York, 1964.

[86] L.J.Swartzendruber, L.H.Bennett, H.Ettedgui and I.Aviram, *Journal of Applied Physics*, vol.67, pp.5469, 1990.

[87] C.B.Rorabaugh, *Digital Filter Design's Handbook with C++ Algorithm*, McGraw-Hill, New York, 1997.

[88] B.Zhu, M.J.Johnson, C.C.H.Lo and D.C.Jiles, to be published in *IEEE Transactions on Magnetics*.

[89] D.C.Jiles, J.B.Thoelke and M.K.Devine, *IEEE Transactions on Magnetics*, vol.28, no.1, pp.27, 1992.

[90] M.J.Sablik, H.Kwun, G.L.Burkhardt and D.C.Jiles, *Journal of Applied Physics*, vol.61, pp.3799, 1987.

[91] D.C.Jiles, *Journal of Physics D: Applied Physics*, vol.28, pp.1537, 1995.

[92] L.Callegaro and E.Puppin, *Applied Physics Letter*, vol.68, no.9, pp.1279, 1996.

[93] L.D.Landau and E.M.Lifschitz, *Phys.Z.Sovietunion*, vol.8, pp.153, 1935.

[94] T.L.Gilbert, *Physical Reivew*, vol.100, pp.1243, 1955.

[95] W.F.Brown, Jr., Magnetostatic Principles in Ferromagnetism, North-Holland Publishing, Amsterdam, 1962.

[96] L.D.Landau and E.M.Lifshitz, *Electrodynamic of Continuous Media*, Pergamon Press, Oxford, 1960.

[97] A.E.Labonte, *Journal of Applied Physics*, vol.40, pp.2450, 1969,

[98] S.Müller-Pfeiffer, M.Schneider and W.Zinn, *Physical Review B*, vol.49, pp.15745, 1994.

[99] M.J.Donahue and R.D.McMichael, *Physica B*, vol.233, pp.272, 1997.

[100] D.V.Berkov, K.Ramstöck and A.Hubert, *Physica status solidi. A*, vol.137, pp.207, 1993.

[101] M.J.Donahue, *OOMMF User's guide 1.1b0*, http://math.nist.gov/oommf, 2000.

[102] A.J.Newell, W.Williams and D.J.Dunlop, *J.Geophysical Research*, vol.98, pp.9551, 1993.

[103] D.C.Jiles, T.T.Chang, D.R.Hougen and R.Ranjan, *J.Appl.Phys*, vol.64, pp.3620, 1988.

[104] I.J.Garshelis, *J.Appl.Phys*, vol.73, pp.5629, 1993.

[105] E.C.Stoner and E.P.Wohlfarth, *Phil.Trans.Roy.Soc.* vol.A240, pp.599,1948.